

June 6, 2025

Dear Reviewers,

First of all, we would like to sincerely thank you for your constructive and detailed comments on our manuscript. We have carefully addressed all of your suggestions and concerns. Please find below our responses (in black) to your comments (in blue). In addition to the changes suggested by the reviewers, we have also made minor edits throughout the manuscript to improve clarity and readability.

For your convenience, we have included a marked-up version of the revised manuscript showing all changes.

Yours sincerely,

Ang Li, Mac Gaunaa, Georg Raimund Pirrung and Kenneth Lønbæk

Comments to Reviewer #1

Overall, I am very pleased with this paper. However, please address the following comments:

1. From figures 8 to 18, the spanwise C_t and C_p show higher projection and wake effects on the outboard span of the blade. Please discuss why.

We thank the reviewer for the positive feedback and for highlighting this consistent pattern. We agree that the projection and wake-induced effects are more pronounced toward the outboard part of the blade. This is because the geometric curvature (sweep, prebend or both combined) is introduced only in the outer half of the blade, while the inboard half of the blade remains straight. To clarify these mechanisms, we have added some brief explanations in Sections 4.6, 4.7 and 4.8.

In Section 4.6: *For the swept blades, both projection and wake-induced effects are concentrated in the outboard half of the span. This is because for the swept blades used in this study, the blade sweep begins only from the mid-span, and the inboard section remains straight.*

In Section 4.7: *For prebent blades, the projection effects arise only in the outboard region, which is consistent with the blade geometry setup where prebend begins around mid-span.*

In Section 4.8: *This redistribution arises from the combination of sweep and prebend applied in the outboard portion of the blade. However, the superposed geometrical changes lead to more complex aerodynamic behavior, with both sweep effects (local effects) and prebend effects (global effects) combined.*

2. Nomenclature for parameters in Table 2 is missing in the appendix.

We thank the reviewer for pointing this out. As suggested, we have now added all previously missing parameters in the table to the nomenclature section in the Appendix.

Comments to Reviewer #2

An interesting article about curved blades and the issues that are accompanied by modelling these. The statement that the entanglement of the mentioned two effects hinders the evaluation of the effects of blade curvature on loads (abstract p1 line 12) can be argued to be subjective. For example, from the viewpoint of a manufacturer it could be desirable to evaluate the full effect (projection + wake) of curving a blade on its performance, keeping chord and twist distribution the same. This should be reflected upon more carefully. However from the viewpoint of modeling and design, the article provides new and valuable insights by separating projection and wake induced effects, and hence is worthy of publication.

We thank the reviewer for this insightful comment. We fully agree that from a manufacturer's perspective, evaluating the full aerodynamic impact of the blade's curvature while keeping the chord and twist distributions fixed, is a natural and practical approach to assess performance. Indeed, our previous statement that "..., hindering the clear evaluation of how blade curvature alone influences the loads and inductions." (in p1 line 12) was not strictly correct.

However, the purpose of the present study is not to suggest that the full effect is unimportant, but rather to support aerodynamic model development, benchmarking and design optimization, where isolating wake-induced effects from the projection effect is crucial. This isolation allows for a clear understanding of how blade curvature affects the wake and hence the induced velocities. To reflect this distinction more clearly, we have revised the relevant sentence in the abstract:

Consequently, wake-induced effects on loading and induction become entangled with projection effects, hindering the clear evaluation of how wake-induced effects, due solely to blade curvature, influence the loads and induction.

This clarifies that the goal is to enable targeted analysis of wake-induced aerodynamic effect. We also emphasize this point in the revised introduction (Section 1) for clarity:

From a performance evaluation point, it may indeed be relevant to consider the combined effect due to projection and wake. However, for the purposes of aerodynamic model development, benchmarking and design optimization, it is crucial to disentangle these effects to understand how blade curvature alone influences the wake and the induction.

It is recommended to follow up on the below suggestions for improvement:

-The article is rather lengthy for the message it brings, and it is advised to re-arrange the content in a more concise way, making it also more digestible.

We thank the reviewer for this constructive comment. We carefully reconsidered the manuscript's structure and agree that readability and conciseness are critical for clearly communicating our findings.

We would like to respectfully clarify that the primary goal of this paper is to provide a comprehensive and foundational framework for aerodynamic model development, benchmarking,

and design optimization of curved wind turbine blades. Specifically, the manuscript provides:

- A general method to isolate wake-induced effects by removing projection effects via modified chord and twist.
- Systematic validation across different types of blade curvature (sweep-only, prebend-only and combined).
- Comparisons across multiple operational conditions, ranging from high to low rotor loading, offering a complete analysis.
- Critical revisits of results in previous works using original (unmodified) swept blades and prebent blades, demonstrating the importance of removing projection effects.
- Demonstration that BEM-based corrections are effective in removing the projection effect.
- New insights from CFD results showing that wake-induced effects from sweep and prebend can be modeled separately and then linearly superimposed. This finding is only possible based on the framework developed in the present work.
- Explicit implications for future engineering aerodynamic model development, benchmarking and design optimization.

To ensure reproducibility, clarity and serve as a long-term reference, the manuscript includes detailed derivations and comparisons. In addition, we provided a substantial online appendix with more than 200 pages, with extensive supplementary cases [1]. Our intent is for the paper to stand as a benchmark resource, reducing the need for repeated CFD studies on such curved blades in future studies.

We have carefully considered the reviewer's suggestion to significantly shorten the manuscript, but ultimately concluded that preserving detailed derivations, results and explanations is crucial. This is because the study is intended to be comprehensive, complete and fully reproducible, which would be useful over the long term. That said, we took the reviewer's comment seriously and made revisions to enhance clarity and digestibility. Specifically:

- We revised sentence structures throughout to enhance readability and clarity.
- We added an explicit organizing paragraph in the introduction, clearly summarizing the logical progression and help guiding readers through the structure.
- We have refined the language, aiming at improving readability without omitting technical details. Rather than shortening content, these clarifications make the logic and progression easier to follow, which we believe enhances accessibility and comprehension.
- In the result section (Section 4), when discussing the results of different lower loading conditions, we only keep the figure of the lowest loading conditions (20 m/s) in the main text. The results of other lower loading conditions (12 and 15 m/s) are moved into the Appendix.

The added organizing paragraph in the introduction (Section 1) is:

The remainder of the paper is organized as follows. Section 2 presents the theoretical foundation within the BEM method and derives the BEM-based chord and twist modifications that removes projection effects. Section 3 details the aerodynamic models used for comparison, including the BEM implementation and the CFD setup. Section 4 compares the results of the original and modified curved blades at different operational conditions. Section 5 summarizes the key findings and their implications for future aerodynamic modeling and blade design.

We hope the updated version balances comprehensiveness with readability and we thank the reviewer again for encouraging us to communicate the paper's scope more clearly.

-Many of the citations reach back to literature from own work and is on curved blades as well. To ensure there is no overlap between these, it would be good to clarify the relation between the articles.

We thank the reviewer for this valuable suggestion. To clarify the relationship between the present study and our prior work:

In [2, 3], we developed two mid-fidelity aerodynamic model for swept blades and prebent blades, respectively. We benchmarked them against BEM, LL and CFD. However, both studies used the same chord and twist distributions for the curved and straight blades, meaning that the projection effects were not removed. As a result, the projection and wake-induced effects were entangled in the comparison.

In [4], we provided a theoretical analysis showing that, within the BEM framework, a curved blade will produce the same inductions and lift-based loads as a straight blade if the radial circulation distribution is identical. However, that study did not show how to modify the chord and twist to achieve this condition.

The present work builds directly on [4] by deriving the necessary chord and twist modifications to match circulation and thus remove projection effects. We revisit the original swept and prebent blade cases from the previous studies [2, 3]. We also extend the analysis to blades with combined sweep and prebend. We show numerically that the projection effects can be effectively removed using the BEM-based corrections derived in the present work. Finally, we demonstrate that sweep and prebend effects can be modeled independently and superimposed, based on CFD results. This last result has direct implications for the development of mid-fidelity engineering aerodynamic models.

We have clarified these distinctions in the updated introduction (see the second last paragraph in Section 1).

-The introduction of projection and wake-induced effects (p2 line 53) could do with a visualization to clarify and define these effects more clearly to the reader.

We appreciate the reviewer's suggestion to include a visualization to clarify the projection and wake-induced effects. In the introduction (Section 1) of the manuscript, we described the projection and wake-induced effects. Furthermore, we used a backward swept blade as an example to describe the two effects. In the later section (Section 2), we described the projection effects more concisely using analytical expressions, as also shown in [4]. For wake-induced effects of backward swept blades, both the trailed wake geometry and bound vortex contributions were illustrated and discussed in prior work [2, 5].

However, we fully agree with the reviewer's suggestion that a qualitative visual illustration would greatly improve clarity for readers, especially those less familiar with these concepts. Therefore, we have now included a new figure (Figure 1 in Section 1) that visually illustrates the projection and wake-induced effects using a backward swept blade as an example, consistent with the existing descriptions in the manuscript. In addition, we have revised the manuscript by clearly showing the role of referenced previous works on projection and wake-induced effects, thereby enhancing the manuscript's readability.

We appreciate the reviewer's guidance, which helped us significantly improve the clarity and comprehensibility of our manuscript.

-At several points the three-quarter chord point is explained to be used for angle of attack evaluation, following unsteady airfoil theory. Perhaps the authors can include a reference citation to the original work on airfoil theory as well?

We thank the reviewer for the helpful suggestion. We have now added references to both classical and modern sources on unsteady airfoil theory. Specifically, we cite the classical work by Theodorsen [6] as well as more recent works [7, 8]. These references have been included in the revised manuscript to support the discussion on evaluating the angle of attack at the 3/4 chord point for lift magnitude and evaluating at the 1/4 chord point for lift direction.

-Section 3.1 p20 line 488. Is it true that the tip region does not affect the flow at the root? Or should tip and root be exchanged in this sentence?

We thank the reviewer for pointing out this issue. The original statement was indeed inaccurate as it only applies to swept blades and not to general curved blade geometries. To avoid confusion, we have removed that sentence.

-Section 3.2 p20 line 503. Are the 2D airfoil data from CFD consistent with the 3D-CFD method described in section 3.1 (e.g. both turbulent but also in general terms of performance prediction)? That would be a prerequisite for a sound comparison between BEM and CFD.

We thank the reviewer for raising this important point. To address this, we have added the following clarification in Section 3.2:

The airfoil data used in the BEM method is from 2-D fully turbulent CFD simulations [9], using EllipSys2D with the same turbulence model ($k-\omega$ SST) as employed in the 3-D CFD simulations described in Sect. 3.1. In previous benchmark studies [10, 11, 12], BEM and other engineering aerodynamic models using the same 2-D airfoil data have shown good agreement with 3-D CFD results from EllipSys3D. This consistency provides a solid foundation for comparing BEM and CFD results in the present work.

-Section 4.3.2 Modified curved blades. Please include a visualization of the planform modification comparison to the original curved blade.

We thank the reviewer for this helpful suggestion. In response, we have added a new figure (Figure 8) in Section 4.3.2, which visualizes the planform modifications of the modified swept and prebent blades compared to the baseline straight blade. The figure shows the offset in chord length and twist angle. We have also added corresponding text in the manuscript to explain the observed behavior and reference the relevant equations derived in the present work.

-Section 4.6 Swept blade case. I find some of the results description difficult to follow as different points are being made in an alternating way (how well does the projection removal work and how relevant are projection effects in comparison to wake effects). It would be great if the structure can be re-arranged to improve readability in that sense (e.g. instead of sections about different operational conditions, separate sections by the points that are to be made).

We thank the reviewer for this valuable suggestion and for proposing an alternative structure of Section 4.6. We fully understand the rationale behind organizing the results according to the main discussion points rather than by operational condition. After careful consideration, we concluded that the current structure, with the discussion organized by operational conditions (optimal and lower loading), remains the most logical and transparent approach for presenting the results. A key goal of the analysis is to enable direct comparison and analyze of projection and wake-induced effects at each operational condition. Organizing the results by operational condition ensures that the reader can evaluate all relevant aerodynamic effects in a step-by-step manner for each operational condition.

We also carefully considered the alternative structure suggested by the reviewer. Reorganizing the section by discussion point (e.g., projection effects, wake-induced effects, etc.) across all wind speeds, in our view, would have resulted in more fragmented descriptions. Readers would need to navigate through multiple sections, each including descriptions of different operational conditions, to get the full findings. Also, direct comparisons within a single operational condition would be harder to follow. In contrast, the current structure allows for a consistent and logical step-by-step evaluation of all effects at each loading condition. We believe that this structure better supports both the clarity of the discussion and the physical interpretation of the results.

To ensure consistency and clarity, our analysis at each operational condition follows a consistent and structured sequence:

- Projection effects: Load offsets predicted by BEM for the original swept blades, which is only

due to projection effects. In comparison, load offsets of the modified swept blades predicted by BEM is approximately zero, indicating the projection effects are removed.

- Wake-induced effects: Load offsets from CFD for the modified swept blades, highlighting wake-induced effects. Also, we describe the load re-distribution pattern due to blade sweep, as also observed in previous work [2].
- Performance of using original blades: Assessment of whether CFD results of original swept blade (as used in previous work [2]) can correctly show the wake-induced effects. And what is the error due to projection effects.
- BEM-based correction: Apply the BEM-based correction to original swept blade CFD results, showing good agreement with the modified blade CFD results. This means the projection effects are effectively removed.

It is the intention that this consistent structure helps readers compare and interpret results clearly across both high and low loading conditions.

To further address the reviewer's concern about clarity and to help guide readers, we have made the following changes. We have revised the title of Section 4.6 from "Revisit of the swept blade cases" to "Blades with only sweep" to reflect that the analysis goes beyond revisiting and includes new comparisons using modified swept blades. We have also updated the first paragraph in Section 4.6 to better summarize the original work and clarify the novelty in the present analysis. We now explicitly state that the previous work used original swept blades (with unmodified chord and twist) and that the present work includes both original and modified swept blades for comparison. Similar clarification changes have been performed in Section 4.7 for prebent blades.

We hope these changes further improves the clarity and readability of Section 4.6 and Section 4.7 while maintaining the logical structure and progression of the analysis. We thank the reviewer again for encouraging us to carefully consider the structure of this section.

It is stated that CFD simulations of the original swept blades are unsuitable to determine the wake induced effect at low loading conditions. But are we interested in this effect at low loading conditions as it is rather small? And after all, what kind of % difference in terms of rotor integral C_p and C_t are we talking about? It would be good to clarify the relevance.

We thank the reviewer for raising this thoughtful and important question. We agree that for design optimization and performance evaluation, the aerodynamic effects at the optimal operational condition are typically of primary interest. However, the aim of the present study is to systematically disentangle and quantify the individual contributions of projection and wake-induced effects across a wide range of loading conditions, rather than focusing solely on optimal operation.

Specifically, we show that the spanwise load redistribution effects due to sweep and prebend, which are observed at the optimal condition, also exist at lower loading conditions, but only when projection effects are removed using the modified curved blades. These pure wake-induced effects at lower loading conditions have not been reported in previous studies. This highlights the

importance of removing the projection effects and demonstrates that blade curved geometry results in a consistent wake-induced effects across different operating conditions.

To address the reviewer's suggestion, we have added new dedicated sections in the revised manuscript (Sections 4.6.3, 4.7.3 and 4.8.3) for each blade geometry, focusing on rotor-integrated effects. In these sections, we present tables summarizing the relative differences in rotor-integrated thrust and power coefficients (C_T and C_P). We compare the relative influence of:

- The total effect (from CFD results of the original curved blades)
- The wake-induced effect (from CFD results of the modified curved blades)
- The projection effect (from the difference between the total and wake-induced effects)

The relative differences are computed as: $\epsilon C_i = (C_i - C_i^{\text{Str}})/C_i^{\text{Str}}$, where C_i represents either the thrust coefficient (C_T) or the power coefficient (C_P), and the superscript "Str" denotes the baseline straight blade.

The results demonstrate that for sweep-only and prebend-only blades, the wake-induced effect is more significant at the optimal operational condition. However, as wind speed increases and rotor loading decreases, the projection effect becomes increasingly dominant. For blades with both sweep and prebend combined, the projection effect is already significant at the optimal condition and becomes even more dominant at lower loading conditions.

These findings are discussed in detail in each section, making it clear how the relative magnitude of projection and wake-induced effects changes across different operational conditions and curved blade geometries. We also note that rotor-integrated quantities may not fully represent the details of the local wake-induced effects, since the spanwise load redistribution may partially cancel out when integrated along the blade span.

We thank the reviewer again for this helpful suggestion, which led to a clearer and more complete presentation of the relative importance of these effects for both local and rotor-integrated aerodynamic performance.

Do we need to see all wind speeds (p31 Fig 10) or can we do with the 20m/s case to illustrate the point of projection effects being dominant (which was to be expected at low induction) and the confirmation of the modified blade performance? It is nice to see that the BEM based adjustments applied to the original blade CFD agree with the modified blade CFD.

We thank the reviewer for this helpful suggestion. Our aim in the results section (Section 4) is to systematically investigate both high and lower loading conditions to understand how projection and wake-induced effects evolve across a wide range of operational conditions. Specifically, we include one high-loading case ($C_T = 0.9$) corresponding to the optimal operating condition, and three lower-loading cases ($C_T = 0.4, 0.2, 0.1$).

While the case at 20 m/s (lowest loading, $C_T = 0.1$) clearly illustrates the projection effects is much higher than the wake-induced effect, it alone does not provide a complete picture. The intermediate conditions (12 and 15 m/s with $C_T = 0.4$ and 0.2) help reveal how the relationship between projection and wake-induced effects changes with loading.

Therefore, we believe including all tested wind speeds offers a more complete and informative characterization of the aerodynamic behavior across different operational conditions.

However, we agree with the reviewer that it is not necessary to include all lower loading condition results in the main manuscript. In response to the reviewer's suggestion, we have kept only the figures for 20 m/s in the main text, while the figures for wind speeds at 12 m/s and 15 m/s have been moved to the Appendix. For completeness and to allow direct comparison, the Appendix also includes the 20 m/s results.

We believe that these changes make the manuscript more concise and accessible, while preserving the completeness and transparency of our analysis. We thank the reviewer again for this constructive input.

-Section 4.7 Prebend. It seems a bit much to arrive at more than 4 pages to draw a similar conclusion as for the swept blades section 4.6. The summaries in 4.6.3 / 4.7.3 / 4.8.3 seem very similar

We thank the reviewer for the comment regarding the length and structure of Section 4.7 and the observation that the summaries in Sections 4.6.4, 4.7.4 and 4.8.4 may appear similar. While these sections follow a consistent structure to enable clear comparisons across swept, prebent and combined curved blade geometries, the aerodynamic effects and conclusions in each case differ in significant ways.

In Section 4.7, we focus on the prebent blade cases, which differ fundamentally from the swept blade cases (Section 4.6) in aerodynamic effects. Specifically, blade prebend at the outboard region leads to a more global spanwise load redistribution due to its influence on the entire wake geometry (since the wake is displaced upwind or downwind compared to the rotor plane). In contrast, blade sweep at the outboard region generates mostly localized effects in the curved blade region (due to local azimuthal shifts in the trailed wake and the curved bound vortex). This distinction has direct implications for the development of mid-fidelity aerodynamic models, which will require different approaches for modeling sweep and prebend effects. Additionally, projection effects are shown to be stronger for prebent blades than for swept blades, especially under lower loading conditions.

Section 4.8 analyzes more general cases that the curved blades have both sweep and prebend combined, with all four possible combinations of blade curve direction investigated. For such combined curved blades, projection effects become more significant and the wake-induced effects are more complicated. This section also presents a key new finding: the wake-induced effects of sweep and prebend can be modeled independently and then superimposed. Again, the conclusions in Section 4.8 have significant differences from Section 4.6 and 4.7, despite some

similarities.

We would like to emphasize that, although some of the content and structure may appear repetitive, this approach ensures a thorough and reproducible analysis. The inclusion of detailed results and comparisons for each case (sweep-only, prebend-only and combined) is crucial to provide a comprehensive and solid investigation. This systematic approach allows readers to clearly see the differences and similarities across different cases and ensures transparency of methodology and results.

We have updated the manuscript in Sections 4.6 to 4.8 to make the differences between these sections clearer. We hope this clarifies the reasons of using a uniform structure while highlighting different aerodynamic characteristics and modeling implications in each section.

-The motivation behind having curved blades sometimes originates from unsteady load alleviation. The subject of the present work is on steady performance. Could the authors comment/hypothesize on the effect of the removal of the projection effects on dynamic loading?

We thank the reviewer for raising this important point. While it is true that one motivation for curved blade designs is unsteady load alleviation, we would like to clarify that the purpose of removing projection effects in the present study is to enable a clean aerodynamic comparison. Particularly, the purpose is to isolate the wake-induced contributions under steady-state conditions for aerodynamic benchmarking, design optimization and model development. It is not intended to modify or capture the dynamic response of flexible blades or unsteady load alleviation behavior.

We hypothesize that removing projection effects does not fundamentally change the characteristic of unsteady wake and structure interactions. This is because the wake geometries generated by curved blades (e.g., swept or prebent) will be very similar to those of not removing the projection effects. Our reasoning is that removing the projection effects only slightly adjusts the rotor loading and will have very small impact on the blade's aeroelastic deformation. This will result in negligible influence on the overall wake geometry and in turn have negligible influence on the dynamic behavior.

However, we fully agree that both the dynamic aerodynamic response and the aeroelastic response of curved blades are important topics for future research. In response to the reviewer's suggestion, we have revised the "Conclusions" section (Section 5) to "Conclusions and future work" to specifically highlight these directions. As the present study focuses exclusively on steady-state aerodynamic behavior of rigid blades, we have not addressed dynamic or aeroelastic behavior in the current manuscript, but have included this as an outlook for future work.

While this work has focused on steady-state aerodynamic comparisons of rigid blades, the aeroelastic response of curved blades remains an important direction for future research. In particular, the dynamic aerodynamic response of curved blades may differ significantly from that of straight blades. Moreover, the observed load redistribution, through loading or deloading near the tip region, is expected to change both the steady and dynamic aeroelastic load alleviation associated with blade sweep.

Also, the current analysis features rigid blades. What would be the order of magnitude of the proposed twist modifications in comparison to the expected torsion angle deformations?

We thank the reviewer for this insightful question. The twist modifications derived in Section 2 are not intended as design changes but are instead used as an analytical and computational tool to enforce the same spanwise circulation distribution when comparing curved and straight blades.

For the optimal operational condition (8 m/s), the twist modifications at the blade tip are small, only 0.14° for the swept blade and only -0.25° for the prebent blade. At the lower loading condition with $C_T = 0.1$ (20 m/s), the twist modifications increase in magnitude: at the blade tip, the values are 0.46° for the swept blade and -0.81° for the prebent blade, as shown in Figure 8 in the manuscript.

For comparison, aeroelastic simulations of the IEA 10MW RWT blade (the same reference blade as used in this study), performed by Gözcü and Verelst [13] reported torsional deformations at the blade tip of approximately 1.0° and 2.3° , for these two operating conditions. Thus, the twist modifications applied here are about 5 to 7 times smaller than the structural torsional deformations for the swept blades, and 3 to 4 times smaller for the prebent blades.

However, we emphasize that these two quantities serve different purposes. Structural torsional deformation is the actual aeroelastic response to loading, while the twist modification is an artificial adjustment introduced in the numerical setup to remove projection effects and highlight the wake-induced effects. Because of this fundamental difference, and because the present paper focuses exclusively on rigid blades, we have not included a detailed numerical comparison in Section 2. However, to provide readers with a sense of the typical magnitude for comparison, we have added a clarifying paragraph in Section 2.6.

In comparison, Gözcü and Verelst [13] reported the blade tip torsional deformations between 1.0° and 2.3° in aeroelastic simulations of the IEA 10MW RWT blade for the operational conditions used in the present work. Therefore, the twist modifications applied here are, on average, approximately five times smaller than the aeroelastic torsional deformations.

Comments to Reviewer #3

The results presented in this study account for projection effects on predictions of aerodynamic loading for a wind turbine with curved blades, allowing for wake-induced loading effects to be isolated. Verifying that effects from sweep and prebend can be determined independently and superimposed will have significant benefits for this area of study. The process of finding these results is well documented and clearly explains the motivation and relevance to similar studies.

Please explain whether "dihedral" is dependent only on prebend or relies on coning/blade deflection as well. Is this related to the toe/cant angles of the blade?

Thank you very much for your encouraging feedback and thoughtful question.

In our approach, the blade geometry includes blade (pre-)sweep, prebend, coning and elastic deflection, with coning and deformation are treated as integral parts of the overall blade geometry. The sweep and dihedral angles are defined using the coordinates of the blade's main axis in the blade root coordinate system (B-sys) and are used to describe the local in-plane (sweep) and out-of-plane (dihedral) orientations of the blade at each spanwise location. By using the spanwise distributions of sweep and dihedral angles, we are able to represent the combined geometric effects along the entire blade. Additionally, as described in Section 2, we use the assumption that the airfoil sections are always perpendicular to the main axis and can then rotate by a twist angle (which includes twist, pitch and torsional deformation), so that the full 3-D blade geometry is determined.

Regarding toe and cant angles, these are local geometric features typically defined relative to neighboring blade sections and are especially relevant for describing detailed local geometries. In our framework, the combined global and local geometric effects, including those that could be represented by local toe and cant angles, are fully captured by the spanwise distributions of sweep and dihedral angles defined in the blade root coordinate system (B-sys).

We have clarified this point in the revised manuscript in Section 2 and hope this explanation addresses your question. Thank you again for your helpful suggestion.

It would be helpful to include a reference justifying the decision to not consider the effect of wake rotation effect on thrust coefficient (Section 2.5).

Thank you for your suggestion regarding the justification for neglecting the wake rotation effect on the thrust coefficient in Section 2.5. In response, we have added a reference to [14], which numerically demonstrates that the wake rotation effect is generally small for modern wind turbine designs, except near the blade root region. Additionally, we have included a reference to a previous study [3], Section 3.2, which provides detailed arguments showing that including the wake rotation effect would not change the conclusions. These same detailed arguments also apply to the present study. These references are now cited in the revised manuscript.

The derivation of Eqs. 50 and 51 was not described clearly.

Thank you for pointing out the need for a clearer derivation of Eqs. (50) and (51). In the revised manuscript, we added the explanation just before these equations to clarify how they are obtained. We hope this clarification addresses your concern and improves the readability of this section.

Substituting Eqs. (48) and (49) into Eqs. (19) and (21), respectively, the relationships in the 2-D flow angle and the relative velocity between curved and straight blades are derived to be:

Discussion of results in Sections 4.6-4.8 is somewhat repetitive - it would be helpful to summarize this information in a more concise way.

Thank you for your comment regarding the repetitive structure in the discussion in Sections 4.6 to 4.8 and your suggestion to summarize the information more concisely.

As also noted in the response to Reviewer 2, the summaries in Sections 4.6, 4.7 and 4.8 follow a consistent structure. This was a deliberate choice to enable clear, systematic comparisons across swept, prebent and combined curved blade geometries. While the structure may appear repetitive, it ensures a thorough and transparent analysis, which allows the reader to easily compare results and understand the different aerodynamic effects and modeling approaches required for different curved blade geometries.

Nevertheless, we recognize the importance of conciseness. In response to your suggestion and similar feedback from Reviewer 2, we have revised the manuscript to better highlight the key differences and reduce unnecessary repetition, while maintaining a uniform structure for comparability.

We hope these revisions address your concern and improve the clarity and value of the discussion.

Appendix A is not comprehensive, and is missing several relevant variables and subscripts used throughout the work, such as those used in Section 2.6 and Section 4.3.1.

Thank you for your comment regarding missing variables and subscripts in Appendix A. We note that this issue was also raised by Reviewer 1. In response, we have now added all previously missing variables and subscripts from Sections 2.6 and 4.3.1 to Appendix A. We appreciate your attention to detail.

The label of "CFD - Delta BEM, Original" is unclear.

Thank you for your helpful comment regarding the clarity of the legend, specifically the label CFD- Δ BEM, Original.

In response, we have updated the legend and notation to improve consistency and clarity. We now use (origin) and (mod) in the legends to distinguish the original and modified curved blades. This approach is consistent with the naming conventions used throughout the manuscript. We chose to use parentheses rather than superscripts in the legends to improve readability and visual clarity.

The label has been changed to "CFD (origin), Δ BEM-adj." in the figures. This clearly indicates that the plots are CFD results for the original curved blade, with the projection effects removed using a BEM-based adjustment. Here, Δ BEM specifically refers to the methodology described in Section 4.4.3, which uses the offset between the modified and original curved blades, as predicted by the BEM method.

We have updated the labels in the figures and also slightly updated the manuscript for clarification. We believe these changes make the figure legends clearer and more intuitive. Thank you again for your constructive feedback to help improve the presentation of our results.

[In Section 4, the notation used to describe the curved blades and modified curved blades is overly complex.](#)

Thank you for your comment regarding the notation used for the curved blades and modified curved blades in Section 4. To address your concern about complexity, we have added a table in the revised manuscript that summarizes the naming convention for all blade types and operating conditions (see Table 2). We believe this addition will make the notation more accessible and easier for readers to reference throughout the manuscript. In addition, we have reviewed all table and figure captions to ensure that the qualitative blade shape (e.g., backward swept blade, upwind prebent blade) is always clearly stated.

We would like to emphasize that a systematic naming convention is important for both clarity and organization. In the manuscript, we focus on a limited subset of blade shapes (specifically, shape indices 1 and 5 and their combinations). However, the online appendix presents a much larger dataset, including all eight shapes and their possible combinations. Consistent and unambiguous naming becomes even more important in this context, as it helps keep results organized and easily referenced for readers and future studies.

Importantly, each blade label in our convention corresponds to a unique and complete dataset, including the main axis geometry, chord length and twist distribution, which is important for reproducibility and transparency. For example, the blade mC-15-U12 refers to a modified curved blade that is a combination of B-1 (backward sweep) and W-5 (downwind prebend). The blade is operating at 12 m/s and the twist distribution is modified according to this operational condition. The suffix of wind speed is necessary, since the twist distribution for modified curved blades at different operational conditions will be different, as shown in Figure 8 (b). This figure is newly added in response to Reviewer 2.

We also highlight that the core of our naming convention (e.g., B-1 and W-1) is directly inherited from previous studies, which allows for direct comparison and consistency with earlier published work.

We hope that the inclusion of the summary table and these clarifications address your concern. Thank you again for your constructive feedback.

Bibliography

- [1] A. Li, M. Gaunaa, G. R. Pirrung, and K. Lønbæk. Internet appendix for: "Disentangling wake and projection effects in the aerodynamics of wind turbines with curved blades", 2025. <https://doi.org/10.5281/zenodo.13149533>.
- [2] A. Li, G. R. Pirrung, M. Gaunaa, H. A. Madsen, and S. G. Horcas. A computationally efficient engineering aerodynamic model for swept wind turbine blades. *Wind Energy Science*, 7(1):129–160, 2022.
- [3] A. Li, M. Gaunaa, G. R. Pirrung, and S. G. Horcas. A computationally efficient engineering aerodynamic model for non-planar wind turbine rotors. *Wind Energy Science*, 7(1):75–104, 2022.
- [4] A. Li, M. Gaunaa, G. R. Pirrung, and K. Lønbæk. How does the blade element momentum method see swept or prebent blades? *Journal of Physics: Conference Series*, 2767(2):022033, jun 2024.
- [5] A. Li, M. Gaunaa, G. R. Pirrung, N. Ramos-García, and S. G. Horcas. The influence of the bound vortex on the aerodynamics of curved wind turbine blades. *Journal of Physics: Conference Series*, 1618:052038, sep 2020.
- [6] T. Theodorsen. General theory of aerodynamic instability and the mechanism of flutter. Technical Report NACA No. 496, National Advisory Committee for Aeronautics, 1935. (last access: 23 November 2021).
- [7] M. Gaunaa. Unsteady two-dimensional potential-flow model for thin variable geometry airfoils. *Wind Energy*, 13(2-3):167–192, 2010.
- [8] G. R. Pirrung and M. Gaunaa. *Dynamic stall model modifications to improve the modeling of vertical axis wind turbines*. DTU Wind Energy E-0171, Roskilde, Denmark, 2018.
- [9] P. Bortolotti, H. C. Tarrés, K. Dykes, K. Merz, L. Sethuraman, D. Verelst, and F. Zahle. Systems Engineering in Wind Energy - WP2.1 Reference Wind Turbines. Technical report, National Renewable Energy Laboratory (NREL), 2019. (last access: 1 August 2024).
- [10] T. Barlas, G. R. Pirrung, N. Ramos-García, S. G. Horcas, A. Li, and H. A. Madsen. Atmospheric rotating rig testing of a swept blade tip and comparison with multi-fidelity aeroelastic simulations. *Wind Energy Science*, 7(5):1957–1973, 2022.
- [11] S. G. Horcas, N. Ramos-García, A. Li, G. Pirrung, and T. Barlas. Comparison of aerodynamic models for horizontal axis wind turbine blades accounting for curved tip shapes. *Wind Energy*, 26(1):5–22, 2023.
- [12] F. Zahle, A. Li, K. Lønbæk, N. N. Sørensen, and R. Riva. Multi-fidelity, steady-state aeroelastic modelling of a 22-megawatt wind turbine. *Journal of Physics: Conference Series*, 2767(2):022065, jun 2024.
- [13] O. Gözcü and D. R. Verelst. The effects of blade structural model fidelity on wind turbine load analysis and computation time. *Wind Energy Science*, 5(2):503–517, 2020.

- [14] E. Branlard and M. Gaunaa. Cylindrical vortex wake model: right cylinder. *Wind Energy*, 18(11):1973–1987, 2015.

Disentangling wake and projection effects in the aerodynamics of wind turbines with curved blades

Ang Li¹, Mac Gaunaa¹, Georg Raimund Pirrung¹, and Kenneth Lønbæk¹

¹Department of Wind and Energy Systems, Technical University of Denmark, Frederiksborgvej 399, DK-4000 Roskilde, Denmark

Correspondence: Ang Li (angl@dtu.dk)

Abstract. Advancements in wind turbine technology have led to larger, more flexible blades and an increasing interest in aerodynamic load calculations and design optimization of blades featuring significant sweep, prebend or coning. High-fidelity blade-resolved computational fluid dynamics (CFD) simulations provide precise rotor performance predictions but are computationally expensive. In contrast, the low-fidelity blade element momentum (BEM) method is computationally efficient but
5 unable to model wake-induced effects of non-straight blades and coned rotors. To bridge this gap, mid-fidelity aerodynamic models, which balance accuracy and computational efficiency, are essential for design optimization tasks. Consistent aerodynamic benchmarks are crucial to effectively evaluate these models, particularly for modeling wake-induced effects across different blade geometries. Previous studies typically used the same chord and twist distributions across different curved blade geometries. However, this approach introduces inconsistencies, as it does not guarantee the same local aerodynamic conditions (e.g., angle of attack and local thrust coefficient) along the blade span due to projection effects of velocities and forces
10 between the 2-D airfoil section and the 3-D flow. Consequently, wake-induced effects on loading and induction become entangled with ~~unwanted~~ projection effects, hindering the clear evaluation of how ~~blade curvature alone influences~~ wake-induced effects, due solely to blade curvature, influence the loads and induction. This study introduces a framework to disentangle wake-induced and projection effects in aerodynamic comparisons of curved blades. Within the BEM framework, we derive the
15 necessary modifications to the chord and twist distributions of curved blades, ensuring the same spanwise circulation distribution as a baseline straight blade. These adjustments remove projection-driven discrepancies, enabling a consistent evaluation of wake-induced effects on loading and induction. Numerical validations using BEM and CFD confirm the effectiveness of these modifications. Additionally, projection effects in existing CFD results can be effectively isolated and removed. Using this framework, we discovered a novel insight from analysis of the CFD results: the wake-induced effects of moderate blade
20 sweep and prebend can be modeled independently and then superimposed. This previously inaccessible insight significantly simplifies the modeling process and provides valuable guidance for developing mid-fidelity engineering aerodynamic models. Overall, this study advances the understanding of blade sweep and prebend effects on normal and tangential aerodynamic loads, supporting future blade design optimization.

1 Introduction

25 Advancements in wind turbine design and manufacturing have resulted in modern horizontal-axis wind turbine (HAWT) blades that are significantly more flexible than the stiff blades of the 1980s, leading to larger elastic deformations. In parallel, there is growing interest in innovative blade designs with non-straight blade shapes and coned rotor configurations. Examples include backward swept blades for passive load alleviation via geometric bend-twist coupling (Liebst, 1986; Zuteck, 2002; Larwood and Zutek, 2006; Manolas et al., 2018), highly flexible blades that exhibit significant out-of-plane deflections (Loth et al., 2012),
30 downwind rotor configurations optimized for low specific wind speed conditions (Madsen et al., 2020b) and aeroelastically tailored curved blade tip designs (Barlas et al., 2021; Madsen et al., 2022). These unconventional blade geometries present significant challenges for aerodynamic load calculation and design optimization. It is crucial to model their aerodynamic effects on loads correctly, particularly in numerical optimization tasks. Using models that cannot correctly capture these effects may lead to blade designs that deviate significantly from the actual optimal design (Li et al., 2022a; Zahle et al., 2024) and
35 unforeseen aeroelastic instabilities may occur. The blade element momentum (BEM) method (Glauert, 1935; Madsen et al., 2020a), which relies on two-dimensional (2-D) airfoil polars¹, has been widely used for aerodynamic and aeroelastic load calculations due to its computational efficiency. However, the BEM method is strictly applicable only to straight blades forming a planar rotor (Li et al., 2022b, 2024), as it does not account for the impact of changes in wake geometry on inductions and loads. Consequently, BEM is considered a low-fidelity method and is often used as the baseline for comparison. On the high-fidelity
40 end, Reynolds-averaged Navier–Stokes (RANS) simulations with fully resolved three-dimensional (3-D) blade geometries (commonly referred to as computational fluid dynamics or CFD) can accurately model the effects of blade geometry on wake and loads since the entire flow field is solved. Despite its accuracy, CFD’s high computational cost limits its practicality for direct use in design optimizations or repetitive aeroelastic calculations. Mid-fidelity engineering aerodynamic models, which include the effects of wake geometry on inductions to different extents, lie between BEM and CFD. If a mid-fidelity model
45 can capture the primary aerodynamic effects of curved blades with significantly lower computational demands than CFD, it becomes a favorable alternative. Examples include the blade element vortex cylinder (BEVC) method for prebend effects (Li et al., 2022b), a vortex-based coupled near- and far-wake model for sweep effects (Li et al., 2022d), corrections to Prandtl’s tip-loss factor for sweep effects (Fritz et al., 2022), higher-fidelity lifting-line (LL) approaches (Phillips and Snyder, 2000; Ramos-García et al., 2016; Boorsma et al., 2020; Branlard et al., 2022) and the actuator line (AL) method (Sørensen and Shen,
50 2002; Meyer Forsting et al., 2019; Martínez-Tossas and Meneveau, 2019). Before confidently applying these models for load calculations and design optimization, consistent aerodynamic benchmarks (Barlas et al., 2022; Horcas et al., 2023) or even aeroelastic benchmarks (Behrens de Luna et al., 2022; Zahle et al., 2024) are essential.

Two primary effects of the curved blade geometry or rotor coning on inductions and loads have been identified, termed *projection effects* and *wake-induced effects*. First, projection effects arise from the projection of velocities and loads between the
55 3-D turbine blade and the 2-D airfoil section under the cross-flow principle (Hoerner and Borst, 1985). For instance, sweeping the blade backward increases the flow angle perceived by the 2-D airfoil section, [as shown analytically in](#) (Li et al., 2024).

¹Obtained from 2-D Navier–Stokes solvers or wind tunnel measurements.

Second, wake-induced effects result from changes in the wake geometry due to the curved blade geometry. For instance, the starting position of the trailed vortex for a backward swept blade follows the blade and is shifted within the rotor plane compared to a straight blade, as described and illustrated in (Li et al., 2018, 2022d). Induction changes also arise from contributions of the curved bound vortex, as analyzed and visualized in (Li et al., 2018, 2020). Fig. 1 provides a qualitative illustration of these two effects.

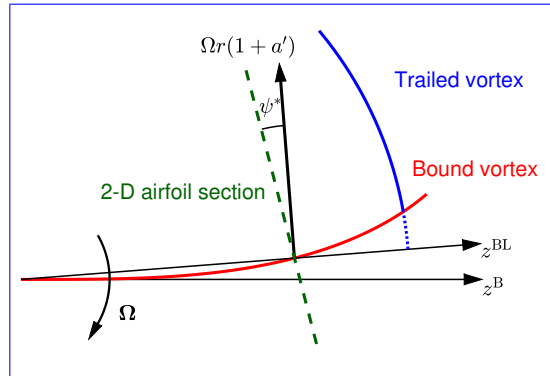


Figure 1. Qualitative illustration of the projection effect and the wake-induced effect for a backward swept blade. The *projection effect* refers to the geometric projection of velocities and loads between the 3-D turbine blade and the 2-D airfoil section. For example, projecting the tangential velocity component $\Omega r(1+a')$ (black arrow) onto the 2-D airfoil section plane (green dashed line) introduces a scaling by the cosine of the effective sweep angle ψ^* . The *wake-induced effect* refers to changes in the wake geometry resulting from blade curvature. In this example, the trailed vortex (blue line) originates from a shifted azimuthal location compared to a straight blade, with the segment shown as a dotted blue line missing. Additionally, the curvature of the bound vortex (red line), which follows the 1/4 chord line of the swept blade, introduces additional induction effects; these are considered as part of the wake-induced effects in this work. A correct implementation of BEM theory captures projection effects, but does not account for wake-induced effects. Note that the 2-D airfoil section is locally perpendicular to the curved blade line and the tangential velocity component is perpendicular to the radial direction (i.e., the z^{BL} -axis).

In previous comparisons, the same chord and twist distributions are typically used for both curved blades and the reference baseline straight blade (Sun et al., 2020, 2021; Li et al., 2022b, c, d; Horcas et al., 2023). ~~Results from~~ For example, Li et al. (2022d) developed a mid-fidelity engineering aerodynamic models are compared against those from BEM and CFD. While an model for swept blades, which demonstrated significantly better agreement with LL and CFD predictions than BEM results. Similarly, the BEVC model introduced in Li et al. (2022b) also showed substantially improved agreement with LL and CFD compared to BEM. ~~While~~ improved agreement with higher-fidelity LL and CFD over BEM suggests that mid-fidelity models better capture wake-induced effects than BEM models, these comparisons the comparisons in both studies do not show the pure effect of the change in geometry because the projection effects (which change the local flow conditions and thus local loading) and the wake-induced effects (the primary focus) are entangled. Moreover, it remains unclear whether having blade sweep or prebend provides aerodynamic benefits, as blades with different geometries may operate under different conditions due to projection effects (e.g., different angles of attack and local thrust coefficients). From a performance evaluation point, it

may indeed be relevant to consider the combined effect due to projection and wake. However, for the purposes of aerodynamic model development, benchmarking and design optimization, it is crucial to disentangle these effects to understand how blade curvature alone influences the wake and the induction. To achieve consistent comparisons, it is essential to minimize projection effects such that the influence of wake geometry on inductions and loads is highlighted. Recent research (Li et al., 2024) demonstrated that, within the BEM method, if a curved blade has an identical radial circulation distribution $\Gamma(r)$ as a straight blade, it will see the same induced velocities. Further, the loads due to the lift force will also be identical between curved and straight ~~blade~~blades; only negligible differences due to the drag force remain.

Building on this insight, the present study ~~derives the~~ directly extends the theoretical work in Li et al. (2024) by deriving the necessary modifications to the chord and twist distributions to ensure curved blades achieve this equivalence. We also discuss important theoretical considerations for aerodynamic comparisons, including curved blade length corrections, non-circulatory loads and the choice of loads for comparison.

~~To demonstrate and validate this approach, we~~ These theoretical developments are then tested in a comprehensive numerical investigation. We first revisit previous numerical comparisons (Li et al., 2018, 2022b, d), examining blades with only sweep and with only prebend. After this, we extend the analysis to curved blades with combined sweep and prebend ~~are investigated,~~ which have significant stronger projection effects. Comparisons are made between BEM and CFD results using both the original setup (unmodified chord and twist distributions, as in previous studies) and the modified setup (with modified distributions, as introduced in the present work). These comparisons aim to evaluate whether the modified setup effectively isolates projection effects, thereby enabling a consistent aerodynamic evaluation of the isolated effect of the non-straight blade geometry on the wake induction. Leveraging the framework derived in this study, we use CFD results to explore the potential of modeling wake-induced effects of sweep and prebend independently and assessing whether their superposition enables simplified engineering aerodynamic modeling methods.

The remainder of the paper is organized as follows. Section 2 presents the theoretical foundation within the BEM method and derives the BEM-based chord and twist modifications that removes projection effects. Section 3 details the aerodynamic models used for comparison, including the BEM implementation and the CFD setup. Section 4 compares the results of the original and modified curved blades at different operational conditions. Section 5 summarizes the key findings and their implications for future aerodynamic modeling and blade design.

2 Consistent modeling of curved blades using the BEM method

This section presents a consistent approach for modeling curved blades within the blade element momentum (BEM) framework, adapted from Madsen et al. (2020a) with specific modifications. In this approach, the drag force contribution is excluded during momentum balancing to determine the inductions (Wilson and Lissaman, 1974; Branlard, 2017). The radial induction model proposed by Madsen et al. (2020a) is omitted, as it is not derived from momentum theory and is not standard in most BEM implementations. However, it is acknowledged that radial induction can contribute to axial and tangential loads if the blade is

105 curved. The rotor is assumed to operate at a constant rotational speed with uniform inflow applied perpendicular to the rotor plane, eliminating effects such as rotor yaw, tilting and wind shear.

Precise definitions of airfoil section alignments and coordinate systems are crucial for a consistent BEM implementation. In the present work, the blade planform is defined along a local main axis, with 2-D airfoil sections oriented perpendicular to it. Unlike planar rotors with straight blades, which have a radially oriented main axis, this analysis incorporates tangential and axial components of the local blade axis to account for blade sweep and prebend. For simplicity, the main axis is initially defined as the 1/4 chord line of the blade. The lift force direction is then directly determined using the flow velocity at the main axis (Bergami and Gaunaa, 2012; Li et al., 2022e)(Oye, 1981; Bergami and Gaunaa, 2012; Li et al., 2022c). Then, the relationship between the chord and twist distributions of the curved blade and the baseline straight blade, which enables the same circulation distribution, is also derived. Afterwards, the assumption that the airfoils are aligned to the 1/4 chord line is relaxed and the equations and conclusions are generalized.

2.1 Coordinate systems and transformation matrices

This section describes the coordinate systems used in this work: the sectional coordinate system (labeled as S-sys), the blade root coordinate system (labeled as B-sys) and the blade local coordinate system (labeled as BL-sys). An illustration of the relationships between these coordinate systems is shown in Fig. 2.

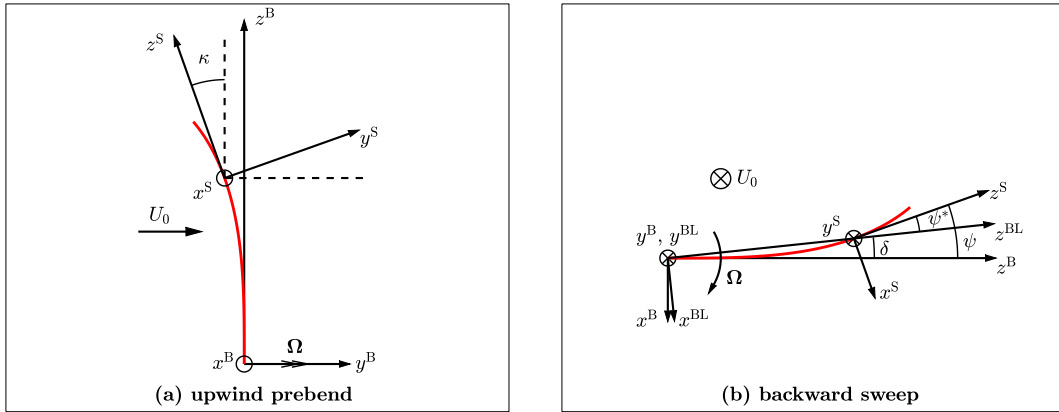


Figure 2. Illustration of different coordinate systems used in the present work. (a) Blade with only upwind prebend, showing the rotation from the blade root coordinate system B-sys around its x -axis with the dihedral angle κ to the sectional coordinate system S-sys. (b) Blade with only backward sweep, showing the rotation from the blade root coordinate system B-sys around its y -axis: with the position angle δ to the blade local coordinate system BL-sys; with the sweep angle ψ to the sectional coordinate system S-sys. The difference between the sweep angle and the position angle is defined as the effective sweep angle ψ^* .

120 The S-sys is introduced for defining the local 2-D airfoil sections. The $x^S - y^S$ plane defines the local airfoil section, with the z^S -axis tangent to the main axis at this section. Importantly, like the B-sys and the BL-sys, the local S-sys does not rotate with twist; that is, the twist angle does not alter the orientation of S-sys in its own definition. However, when transforming

S-sys coordinates into B-sys, a reference twist condition, often referred to as the zero twist angle, must be specified to fix the orientation of S-sys relative to B-sys. When the twist angle is zero, the x^S -axis points from the trailing edge to the leading edge, while the y^S -axis points from the pressure side to the suction side. The B-sys has its origin on the rotational axis and rotates with the blade. The y^B -axis aligns with the free stream direction (axial direction) and the z^B -axis corresponds to the radial direction at the blade root. At each spanwise position, the BL-sys is obtained by rotating the B-sys around its y^B -axis to align the blade section calculation point with the z^{BL} -axis, making z^{BL} the radial and x^{BL} the tangential direction, see Fig. 2 (b).

~~The~~ In the present work, the blade geometry is described in B-sys, including blade sweep, prebend, coning and elastic deflection, with coning and deformation treated as integral parts of the blade geometry. Both the dihedral angle κ and the sweep angle ψ are defined using the main axis coordinates in the B-sys. ~~The~~, ensuring a consistent reference frame for capturing different geometric effects. At a spanwise location along the blade's main axis, the local tangent vector \mathbf{t} is represented using can be represented in terms of the dihedral and sweep angles:

$$\mathbf{t} \equiv \begin{pmatrix} \frac{dx^B}{dz^B} \\ \frac{dy^B}{dz^B} \\ 1 \end{pmatrix} = \begin{pmatrix} -\tan \psi \\ -\tan \kappa \\ 1 \end{pmatrix}. \quad (1)$$

Here, the dihedral angle κ describes the local out-of-plane orientation of the blade relative to the rotor plane, while the sweep angle ψ describes the local in-plane blade orientation.

The transformation matrix from the sectional coordinate system (S-sys) to the blade root coordinate system (B-sys) requires the definition of the zero twist angle. Following the definition used in the HAWC2 code (Larsen and Hansen, 2007), the zero twist angle is defined such that the projection of the y^S -axis from the S-sys into B-sys has no x -component. In other words, once the zero-twist definition is chosen, S-sys is fully determined with respect to B-sys.

$$\mathbf{T}_{S \rightarrow B} = \begin{bmatrix} \frac{1}{\|\mathbf{t}\| \cos \kappa} & 0 & -\frac{\tan \psi}{\|\mathbf{t}\|} \\ -\frac{\sin \kappa \tan \psi}{\|\mathbf{t}\|} & \cos \kappa & -\frac{\tan \kappa}{\|\mathbf{t}\|} \\ \frac{\cos \kappa \tan \psi}{\|\mathbf{t}\|} & \sin \kappa & \frac{1}{\|\mathbf{t}\|} \end{bmatrix} \quad (2)$$

The transformation matrix from B-sys to BL-sys is given by:

$$\mathbf{T}_{B \rightarrow BL} = \mathbf{R}_y(\delta) = \begin{bmatrix} \cos \delta & 0 & \sin \delta \\ 0 & 1 & 0 \\ -\sin \delta & 0 & \cos \delta \end{bmatrix}, \quad (3)$$

where δ is the position angle calculated from the coordinates in the B-sys:

$$\delta = -\arctan \frac{x^B}{z^B}. \quad (4)$$

The transformation matrix from S-sys to BL-sys can then be calculated using Eqs. (2) and (3):

$$\mathbf{T}_{S \rightarrow BL} = \mathbf{T}_{B \rightarrow BL} \mathbf{T}_{S \rightarrow B}. \quad (5)$$

For ease of derivation, a modified sectional coordinate system (S*-sys) is introduced. It is obtained by rotating the S-sys around its z -axis by an angle $\Delta\theta_z$, such that the projection of the y -axis in the S*-sys into the BL-sys has no x -component.

150 Consequently, the transformation matrix $\mathbf{T}_{S^* \rightarrow BL}$ is in the same form as $\mathbf{T}_{S \rightarrow B}$ in Eq. (2):

$$\mathbf{T}_{S^* \rightarrow BL} = \begin{bmatrix} \frac{1}{\|\mathbf{t}^*\| \cos \kappa^*} & 0 & -\frac{\tan \psi^*}{\|\mathbf{t}^*\|} \\ -\frac{\sin \kappa^* \tan \psi^*}{\|\mathbf{t}^*\|} & \cos \kappa^* & -\frac{\tan \kappa^*}{\|\mathbf{t}^*\|} \\ \frac{\cos \kappa^* \tan \psi^*}{\|\mathbf{t}^*\|} & \sin \kappa^* & \frac{1}{\|\mathbf{t}^*\|} \end{bmatrix}, \quad (6)$$

where \mathbf{t}^* is the modified tangent vector:

$$\mathbf{t}^* \equiv \begin{pmatrix} -\tan \psi^* \\ -\tan \kappa^* \\ 1 \end{pmatrix}, \quad (7)$$

with the effective sweep angle ψ^* and the effective dihedral angle κ^* introduced for the ease of formulation:

$$155 \quad \psi^* \equiv \psi - \delta, \quad (8)$$

$$\tan \kappa^* \equiv \tan \kappa \frac{\cos \psi}{\cos \psi^*}. \quad (9)$$

The transformation matrix from the modified sectional coordinate system (S*-sys) to the sectional coordinate system (S-sys) is given by:

$$\mathbf{T}_{S^* \rightarrow S} = \mathbf{R}_z(\Delta\theta_z) = \begin{bmatrix} \cos \Delta\theta_z & -\sin \Delta\theta_z & 0 \\ \sin \Delta\theta_z & \cos \Delta\theta_z & 0 \\ 0 & 0 & 1 \end{bmatrix}. \quad (10)$$

160 The rotational angle $\Delta\theta_z$ is derived based on the condition that $\mathbf{T}_{S^* \rightarrow BL}(1, 2) = 0$.

$$\Delta\theta_z = \arctan \frac{\mathbf{T}_{S \rightarrow BL}(1, 2)}{\mathbf{T}_{S \rightarrow BL}(1, 1)} = \arctan \frac{\|\mathbf{t}\| \tan \delta \tan \kappa}{1 + \tan^2 \kappa + \tan \delta \tan \psi} \quad (11)$$

When either the sweep angle ψ is zero or the dihedral angle κ is zero, the rotational angle $\Delta\theta_z$ will be zero, and the S*-sys will coincide with the S-sys.

2.1.1 Special conditions

165 For the special condition where the blade has only prebend but no sweep, the transformation matrix $\mathbf{T}_{S^* \rightarrow BL}$ simplifies to:

$$\mathbf{T}_{S^* \rightarrow BL}^{\text{prebend}} = \mathbf{R}_x(\kappa) = \begin{bmatrix} 1 & 0 & 0 \\ 0 & \cos \kappa & -\sin \kappa \\ 0 & \sin \kappa & \cos \kappa \end{bmatrix}. \quad (12)$$

For the special condition where the blade has only sweep but no prebend, the transformation matrix $\mathbf{T}_{S^* \rightarrow BL}$ simplifies to:

$$\mathbf{T}_{S^* \rightarrow BL}^{\text{sweep}} = \mathbf{R}_y(-\psi^*) = \begin{bmatrix} \cos \psi^* & 0 & -\sin \psi^* \\ 0 & 1 & 0 \\ \sin \psi^* & 0 & \cos \psi^* \end{bmatrix}. \quad (13)$$

For the special condition where the blade is straight and has no coning, all four coordinate systems described in this section (B-sys, BL-sys, S-sys and S^* -sys) will coincide with each other.

2.2 Projection of the vectors

The projection of vectors between coordinate systems is crucial for accurately calculating aerodynamic loads and velocities. This section summarizes the projection of key vectors, including velocity, bound circulation, angular velocity and centrifugal acceleration, between the 2-D airfoil section in the S^* -sys and the 3-D rotor in the BL-sys.

The 3-D relative velocity vector experienced by the blade section in the BL-sys can be expressed in terms of inductions or the inflow angle φ (see Appendix A for nomenclature):

$$\mathbf{V}^{BL} = \begin{pmatrix} -\Omega r(1+a') \\ U_0(1-a_B) \\ u_r \end{pmatrix} = \begin{pmatrix} -V \cos \varphi \\ V \sin \varphi \\ u_r \end{pmatrix}, \quad (14)$$

with

$$\tan \varphi \equiv \frac{U_0(1-a_B)}{\Omega r(1+a')}, \quad (15)$$

$$V = \sqrt{(V_x^{BL})^2 + (V_y^{BL})^2} = \sqrt{(U_0(1-a_B))^2 + (\Omega r(1+a'))^2}. \quad (16)$$

Following the assumptions described in Sect. 2, the BEM method used in the present work assumes zero radial induced velocity, with $u_r = 0$. The relative velocity vector in BL-sys is transformed into the modified sectional coordinate system (S^* -sys) using the transformation matrix in Eq. (6):

$$\begin{aligned} \mathbf{V}^{S^*} &= \mathbf{T}_{BL \rightarrow S^*} \mathbf{V}^{BL} \\ &= V \begin{pmatrix} -\frac{\cos \varphi}{\|\mathbf{t}^*\| \cos \kappa^*} - \frac{\sin \kappa^* \tan \psi^* \sin \varphi}{\|\mathbf{t}^*\|} \\ \cos \kappa^* \sin \varphi \\ \frac{\tan \psi^* \cos \varphi}{\|\mathbf{t}^*\|} - \frac{\tan \kappa^* \sin \varphi}{\|\mathbf{t}^*\|} \end{pmatrix}. \end{aligned} \quad (17)$$

Figure 3 illustrates the relative velocity vector and its components as perceived by the blade section in the BL-sys and the 2-D airfoil in the S-sys and S^* -sys. This visualization aids in understanding how velocity components differ between coordinate systems and highlights the impact on resulting flow angles.

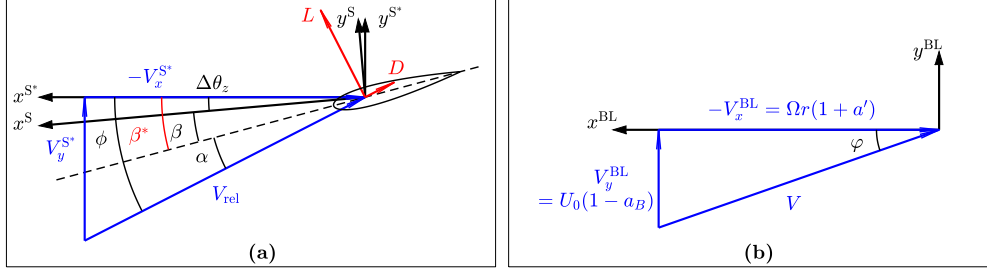


Figure 3. Illustration of velocity triangles experienced by (a) the 2-D airfoil section and (b) the 3-D flow in the blade local coordinate system (BL-sys). In panel (a), the 2-D flow angle ϕ in S^* -sys is shown. The airfoil is aligned along the dashed line. The twist angle is β in the S -sys and is β^* in the S^* -sys. The S -sys is rotated around its z -axis with $\Delta\theta_z$ to get the S^* -sys, with $\beta^* = \beta + \Delta\theta_z$, which is the source of the difference between the two twist angles. The angle of attack α at the calculation point, which is the 1/4 chord point as shown here, is also indicated. The 2-D lift and drag forces are applied perpendicular and parallel to the 2-D relative velocity V_{rel} at the 1/4 chord point, respectively. Panel (b) corresponds to the top view of a clockwise rotating rotor with the blade pointing downward. The axial and tangential velocity components in BL-sys and the inflow angle φ are shown.

The 2-D relative velocity is the velocity magnitude observed by the 2-D airfoil section, neglecting the spanwise velocity component that is normal to the airfoil.

$$190 \quad V_{rel} = \sqrt{(V_x^S)^2 + (V_y^S)^2} = \sqrt{(V_x^{S^*})^2 + (V_y^{S^*})^2} \quad (18)$$

The 2-D sectional flow angle ϕ in S^* -sys is derived from Eq. (17).

$$\tan \phi = \frac{V_y^{S^*}}{-V_x^{S^*}} = \frac{\|\mathbf{t}^*\| \tan \varphi}{1 + \tan^2 \kappa^* + \tan \psi^* \tan \kappa^* \tan \varphi} \quad (19)$$

The angle of attack at the calculation point is calculated from the 2-D flow angle ϕ and the twist angle β^* , both defined in the S^* -sys:

$$195 \quad \alpha = \phi - \beta^*. \quad (20)$$

The 2-D sectional relative velocity magnitude V_{rel} in Eq. (18) is derived as a function of the 3-D relative velocity magnitude V .

$$V_{rel} = \frac{V_y^{S^*}}{\sin \phi} = V \frac{\sin \varphi \cos \kappa^*}{\sin \phi} \quad (21)$$

The bound circulation vector of a blade section in BL-sys, labeled as Γ^{BL} , tangent to the blade's local main axis, is expressed as:

$$200 \quad \Gamma^{BL} = \mathbf{T}_{S^* \rightarrow BL} \begin{pmatrix} 0 \\ 0 \\ \Gamma \end{pmatrix} = \begin{pmatrix} -\frac{\tan \psi^*}{\|\mathbf{t}^*\|} \\ -\frac{\tan \kappa^*}{\|\mathbf{t}^*\|} \\ \frac{1}{\|\mathbf{t}^*\|} \end{pmatrix} \Gamma. \quad (22)$$

For blades with prebend, the 2-D airfoil section experiences an effective torsional motion that result in aerodynamic forces and moments. This has been demonstrated in a previous study focusing on prebend-only blades (Li et al., 2022c). For a generalized curved blade, the angular velocity vector in S^* -sys is first obtained. The effective torsion rate, labeled as $\dot{\theta}$, is the z -component of Ω^{S^*} . A positive effective torsion rate $\dot{\theta}$ corresponds to an effective nose-up motion of the airfoil section².

$$\Omega^{S^*} = \mathbf{T}_{BL \rightarrow S^*} \begin{pmatrix} 0 \\ \Omega \\ 0 \end{pmatrix} = \begin{pmatrix} -\frac{\sin \kappa^* \tan \psi^*}{\|\mathbf{t}^*\|} \\ \cos \kappa^* \\ -\frac{\tan \kappa^*}{\|\mathbf{t}^*\|} \end{pmatrix} \Omega \quad (23)$$

$$\dot{\theta} = \Omega_z^{S^*} = -\frac{\Omega \tan \kappa^*}{\|\mathbf{t}^*\|} \quad (24)$$

The airfoil section of a blade with prebend also experiences an effective mid-chord heaving acceleration which also generates aerodynamic forces and moments (Li et al., 2022c). This effective mid-chord heaving acceleration, denoted as $\ddot{\epsilon}$, is obtained by projecting the centrifugal acceleration vector from the BL-sys into the S^* -sys. It is perpendicular to the chord line and is defined to be positive when pointing from the pressure side to the suction side.

$$\mathbf{a}^{S^*} = \mathbf{T}_{BL \rightarrow S^*} \begin{pmatrix} 0 \\ 0 \\ -\Omega^2 r \end{pmatrix} = -\Omega^2 r \begin{pmatrix} \frac{\cos \kappa^* \tan \psi^*}{\|\mathbf{t}^*\|} \\ \sin \kappa^* \\ \frac{1}{\|\mathbf{t}^*\|} \end{pmatrix} \quad (25)$$

$$\begin{aligned} \ddot{\epsilon} &= a_x^{S^*} \sin \beta^* + a_y^{S^*} \cos \beta^* \\ &= -\Omega^2 r \left(\frac{\cos \kappa^* \tan \psi^*}{\|\mathbf{t}^*\|} \sin \beta^* + \sin \kappa^* \cos \beta^* \right) \end{aligned} \quad (26)$$

2.3 Curved blade length correction

In aerodynamic load calculations using generalized lifting-line methods, which combine the 2-D airfoil modeling with the 3-D wake modeling, sectional loads are first obtained using 2-D airfoil polars. These loads are subsequently transformed into the 3-D blade or rotor coordinate system for further analysis. Alternatively, the lift force can be calculated from the bound circulation using the Kutta–Joukowski theorem in vector form through the cross-product operation, as discussed in Sect. 2.4. For both methods, the calculated loads correspond to load per unit span. This poses no issues when calculating the rotor integrated loads if correctly integrating with respect to the span length. However, loads with other definitions, such as load per unit radius or load per unit of z -coordinate in the blade root system (B-sys), are also commonly used for comparisons. Therefore, correction factors ds/dr and ds/dz are necessary to convert between different definitions and ensure consistent load comparisons. These correction factors can be derived by projecting the spanwise tangent vector in Eq. (1) into the radial direction (z^{BL} -direction) or the z^{B} -direction using the dot product, as demonstrated in Madsen et al. (2020a). Alternatively, the

²Alternatively, projecting the angular velocity vector into the sectional coordinate system S-sys and the effective torsion rate is the z -component of Ω^S .

correction factors can be directly obtained from the transformation matrices:

$$\frac{ds}{dr} = \frac{1}{\mathbf{T}_{S \rightarrow BL}(3,3)} = \|\mathbf{t}^*\|, \quad (27)$$

$$\frac{ds}{dz} = \frac{1}{\mathbf{T}_{S \rightarrow B}(3,3)} = \|\mathbf{t}\|. \quad (28)$$

2.4 Kutta–Joukowski analysis

230 In this section, the lift force acting on the blade is calculated using the Kutta–Joukowski theorem in its vector form, applying the cross-product of the relative velocity vector and the bound circulation vector. This method directly provides the different components of the aerodynamic loads, eliminating the need for complex transformation matrices. The blade is modeled as a vortex filament aligned with the 1/4 chord line of the blade, a framework commonly referred to as the lifting line method. For each section, the lifting line is represented by the bound circulation vector, as in Eq. (22). The blade load due to lift force, 235 represented as force per unit span, is expressed as:

$$\mathbf{f}_L^{\text{BL}} = \rho \mathbf{V}^{\text{BL}} \times \mathbf{\Gamma}^{\text{BL}} = \rho \Gamma \frac{1}{\|\mathbf{t}^*\|} \begin{pmatrix} U_0(1 - a_B) + u_r \tan \kappa^* \\ \Omega r(1 + a') - u_r \tan \psi^* \\ U_0(1 - a_B) \tan \psi^* + \Omega r(1 + a') \tan \kappa^* \end{pmatrix}. \quad (29)$$

The local thrust and power coefficients from the Kutta–Joukowski analysis³, which consider only the lift force, are calculated from the contributions of all N_B blades for an annulus of the rotor disc at radius r :

$$C_{t,\text{KJ}} \equiv \frac{N_B f_{L,y}^{\text{BL}} ds}{\frac{1}{2} \rho U_0^2 2\pi r dr} = k_s \left(1 + a' - \frac{u_r \tan \kappa^*}{U_0 \lambda_r} \right), \quad (30)$$

$$240 \quad C_{p,\text{KJ}} \equiv \frac{N_B \Omega r f_{L,x}^{\text{BL}} ds}{\frac{1}{2} \rho U_0^3 2\pi r dr} = k_s \left(1 - a_B + \frac{u_r}{U_0} \tan \kappa^* \right), \quad (31)$$

where k_s denotes the normalized circulation strength of all blades and λ_r denotes the local speed ratio at radius r :

$$k_s \equiv \frac{\Omega N_B \Gamma}{\pi U_0^2}, \quad (32)$$

$$\lambda_r = \frac{\Omega r}{U_0} = \lambda \frac{r}{R_{\text{tot}}}. \quad (33)$$

245 For cases where the radial induction u_r is neglected and assumed to be zero, as in standard BEM implementations, the coefficients in Eqs. (30) and (31) are simplified as follows. These simplified expressions correspond to the case of a straight blade without sweep or prebend, forming a planar rotor:

$$C_{t,\text{KJ}} = k_s (1 + a'), \quad (34)$$

$$C_{p,\text{KJ}} = k_s (1 - a_B). \quad (35)$$

³These non-dimensioned load coefficients can also be derived by projecting the lift force from S*-sys into BL-sys using transformation matrices, resulting in identical results.

2.5 System closure and induction calculation

250 With a prescribed circulation distribution, calculating inductions using the BEM method with Prandtl's tip-loss correction (Glauert, 1935; Sørensen, 2015) included will still require an iterative process to solve for the inflow angle φ (Lønbæk et al., 2021). The blade's axial induction factor a_B is calculated from the effective local thrust coefficient $C_{t,\text{eff}}$, which is adjusted by dividing it by the tip-loss factor F to account for the effects of having a finite number of blades, in contrast to the actuator disc concept used in the momentum theory of the BEM framework. The effective thrust coefficient $C_{t,\text{eff}}$ is equal to the Kutta–
 255 Joukowski thrust coefficient $C_{t,\text{KJ}}$ minus the contribution of wake rotation $C_{t,\text{rot}}$ (Branlard and Gaunaa, 2015a). The wake rotation effect increases toward the rotor's rotational axis and decreases as the tip-speed ratio increases. In this study, the wake rotation effect is neglected, considering its impact is rather small for typical modern wind turbine designs, except in the root region, as demonstrated numerically in (Branlard and Gaunaa, 2015b). Including this effect would not change the study's conclusions, following the same arguments as previously presented in Section 3.2 of (Li et al., 2022b).

260 The tip-loss factor F is calculated using the inflow angle φ , instead of the 2-D sectional flow angle ϕ that was used in the previous study (Li et al., 2022b). See Fig. 3 for the illustration of these angles. The tangential induction factor a' is directly calculated from the circulation Γ , as in the vortex cylinder model (Øye, 1990; Branlard and Gaunaa, 2015b; Li et al., 2022b).

$$a_B = f_{a-C_t}(C_{t,\text{KJ}}/F) \quad (36)$$

$$F = \frac{2}{\pi} \cos^{-1} \left(\exp \left(-\frac{N_B}{2} \frac{R_{\text{tot}} - r}{r \sin \varphi} \right) \right) \quad (37)$$

$$265 \quad a' = \frac{N_B \Gamma}{4\pi \Omega r^2} = \frac{k_s}{4\lambda_r^2} \quad (38)$$

In the present work, the relationship between the axial induction factor and the thrust coefficient is computed using the empirical polynomial function in Eq. (39) proposed by Madsen et al. (2020a). This polynomial function is also the default relationship in the HAWC2 code (Larsen and Hansen, 2007)⁴.

$$f_{a-C_t}^{\text{Madsen}}(C_t) = \sum_{i=1}^3 k_i C_t^i \quad (39)$$

270 with coefficients $k_3 = 0.0883$, $k_2 = 0.0586$ and $k_1 = 0.2460$.

By substituting $C_{t,\text{KJ}}$ from Eq. (34) into Eq. (36), it becomes evident that the inductions are functions solely of the circulation distribution Γ , or equivalently the Kutta–Joukowski thrust coefficient $C_{t,\text{KJ}}$. The inductions do not depend explicitly on the blade's dihedral angle κ or sweep angle ψ . Therefore, with the same prescribed circulation distribution, a curved blade will have the same inductions (a_B and a'), inflow angle φ and also Kutta–Joukowski thrust and power coefficients ($C_{t,\text{KJ}}$ and $C_{p,\text{KJ}}$)
 275 as the corresponding straight blade forming a planar rotor.

⁴Note that the choice of the $a - C_t$ relationship can significantly influence the design optimizations. For example, using the polynomial relationship in Eq. (39) for optimization would result in designs with a higher thrust coefficient compared to the analytical optimal value of 8/9 from the momentum theory.

This conclusion highlights that, within the BEM framework, the aerodynamic performance of a curved blade can be matched to that of a straight blade by ensuring that the circulation distribution is the same (Li et al., 2024). A more detailed proof is provided in Appendix B.

2.6 Relationship in chord and twist distributions

280 In this section, the relationship between the chord and twist distributions of a curved blade with a given main axis geometry and the corresponding straight blade that has the same bound circulation is derived under the BEM framework. The bound circulation strength is calculated from the 2-D relative velocity V_{rel} , chord length and the 2-D lift coefficient obtained from airfoil polars⁵. Following conclusions from unsteady 2-D airfoil theory, the [magnitude of the](#) lift coefficient is determined using the angle of attack evaluated at the 3/4 chord point ([Bergami and Gaunaa, 2012; Li et al., 2022e](#)). [Although it is not explicitly](#)
285 [stated in the classical work by Theodorsen \(1935\), it can be inferred from the equations presented there. This is explicitly shown in the technical report by Øye \(1981\), as well as later studies \(Gaunaa, 2010; Bergami and Gaunaa, 2012; Li et al., 2022c\).](#)

$$\Gamma = \frac{1}{2} V_{rel} c C_L(\alpha_{3/4}) \quad (40)$$

As discussed in Sect. 2.2, when an airfoil section experiences an effective torsional rate $\dot{\theta}$, the sectional flow angle varies along the chord. For a rotor operating at steady-state conditions, this torsional rate is only from the projection of the angular
290 velocity vector, as shown in Eq. (24). The difference in the angle of attack between the 3/4 and 1/4 chord points is given by:

$$\Delta\alpha \equiv \alpha_{3/4} - \alpha_{1/4} = \frac{\dot{\theta}c}{2V_{rel}}. \quad (41)$$

The angle of attack at the 3/4 chord point can then be calculated from the 2-D flow angle ϕ (evaluated at the 1/4 chord point), the twist angle β^* and the additional angle $\Delta\alpha$:

$$\alpha_{3/4} = \alpha_{1/4} + \Delta\alpha = \phi - \beta^* + \Delta\alpha. \quad (42)$$

295 At each radial position, both curved and straight blades should operate with the same angle of attack at the 3/4 chord point. They are also assumed to have the same spanwise distribution of relative thickness and airfoil series, enabling the use of the same airfoil polars. As a result, the lift coefficients of the two blades are also identical.

$$\alpha_{3/4}^{cur} = \alpha_{3/4}^{str} \quad (43)$$

$$C_L^{cur} = C_L^{str} \quad (44)$$

300 Substituting Eq. (44) into Eq. (40) gives the following relationship between the chord lengths:

$$c^{cur} = c^{str} \frac{V_{rel}^{str}}{V_{rel}^{cur}}. \quad (45)$$

⁵The 2-D relative velocity is calculated in Eq. 21 and does not include the local z^S - or z^{S^*} -components of the total velocity.

As described in Sect. 2.5, the 3-D velocity magnitude V and the inflow angle φ at a given radius are the same for both the curved blade and its corresponding straight blade. For the straight blade, the 2-D relative velocity magnitude V_{rel} is equal to the 3-D value V and the 2-D flow angle ϕ is identical to the inflow angle φ .

$$305 \quad V_{\text{rel}}^{\text{str}} = V \quad (46)$$

$$\phi^{\text{str}} = \varphi \quad (47)$$

For ease of derivation, denote the ratio of tangent and sine values of the 2-D sectional flow angle ϕ and the inflow angle φ as ζ and μ , respectively.

$$\zeta \equiv \frac{\tan \phi}{\tan \varphi} \quad (48)$$

$$310 \quad \mu \equiv \frac{\sin \phi}{\sin \varphi} = \frac{\zeta}{\cos \varphi \sqrt{1 + \zeta^2 \tan^2 \varphi}} \quad (49)$$

The Substituting Eqs. (48) and (49) into Eqs. (19) and (21), respectively, the relationships in the relative velocity and the 2-D flow angle and the relative velocity between curved and straight blades are derived to be:

$$\tan \phi^{\text{cur}} = \zeta \tan \phi^{\text{str}}, \quad (50)$$

$$V_{\text{rel}}^{\text{cur}} = \frac{\cos \kappa^*}{\mu} V_{\text{rel}}^{\text{str}}, \quad \tan \phi^{\text{cur}} = \zeta \tan \phi^{\text{str}}. \quad (51)$$

315 Inserting Eq. (51) into Eq. (45) gives the following relationship for the chord length:

$$c^{\text{cur}} = \frac{\mu}{\cos \kappa^*} c^{\text{str}}. \quad (52)$$

Substituting Eqs. (24), (51) and (52) into Eq. (41), the difference in angle of attack between the 3/4 and 1/4 chord points due to the torsional rate for curved and straight blades is calculated as:

$$\Delta \alpha^{\text{cur}} = \frac{\dot{\theta} c^{\text{cur}}}{2V_{\text{rel}}^{\text{cur}}} = -\frac{\Omega c^{\text{str}}}{2V} \frac{\mu^2 \tan \kappa^*}{\|\mathbf{t}^*\| \cos^2 \kappa^*}, \quad (53)$$

$$320 \quad \Delta \alpha^{\text{str}} = 0. \quad (54)$$

Moreover, since the angle of attack at the 3/4 chord point is identical for both curved and straight blades, the difference in twist angle in the modified sectional coordinate system (S^* -sys) is calculated.

$$\Delta \beta^* = \beta^{*,\text{cur}} - \beta^{*,\text{str}} = \arctan(\zeta \tan \varphi) - \varphi + \Delta \alpha^{\text{cur}} \quad (55)$$

325 Since the twist angle is typically defined in the sectional coordinate system (S -sys), such as in the HAWC2 code (Larsen and Hansen, 2007)⁶, the twist angle difference in the S -sys is also derived:

$$\Delta \beta = \beta^{\text{cur}} - \beta^{\text{str}} = \Delta \beta^* - \Delta \theta_z, \quad (56)$$

where $\Delta \theta_z$ was given in Eq. (11).

⁶The twist angle defined in this study is in the opposite direction to that in the HAWC2 code.

2.6.1 Approximations and special conditions

To further illustrate the relationship between the chord and twist distributions of curved and straight blades, approximations are performed assuming the inflow angle φ is small. This condition is typically satisfied at high tip-speed-ratios and near blade tip regions where the curved blade shapes are commonly employed.

$$\frac{\phi^{\text{cur}}}{\varphi} \approx \frac{\sin \phi^{\text{cur}}}{\sin \varphi} = \mu \approx \frac{\tan \phi^{\text{cur}}}{\tan \varphi} = \zeta \quad (57)$$

The relationship in chord length in Eq. (52) and the twist angle difference in Eq. (56) then simplifies to:

$$c^{\text{cur}} \approx \frac{\zeta}{\cos \kappa^*} c^{\text{str}}, \quad (58)$$

$$\Delta\beta \approx \varphi(\zeta - 1) + \Delta\alpha^{\text{cur}} - \Delta\theta_z. \quad (59)$$

Two special conditions are investigated to highlight the impact of blade sweep and prebend on the modifications to the chord and twist distributions.

For the special condition that the blade has only sweep and no prebend ($\kappa = 0$), it follows that $\zeta = 1/\cos\psi^*$, the approximations are further simplified:

$$c^{\text{cur}} \approx \frac{c^{\text{str}}}{\cos \psi^*}, \quad (60)$$

$$\Delta\beta \approx \varphi \left(\frac{1}{\cos \psi^*} - 1 \right). \quad (61)$$

This shows that a swept blade requires a larger chord length and also a larger twist angle compared to the straight blade to maintain the same circulation distribution. The modifications in chord and twist distributions are symmetric: they depend only on the magnitude of the sweep angle, not its sign.

For the special condition that the blade has only prebend and no sweep ($\psi = 0$), it follows that $\zeta = \cos \kappa$, the approximated relationships in chord and twist distributions can be simplified to:

$$c^{\text{cur}} \approx c^{\text{str}}, \quad (62)$$

$$\Delta\beta \approx \varphi(\cos \kappa - 1) - \frac{\Omega c}{2V} \sin \kappa. \quad (63)$$

This suggests that a prebent blade has approximately the same chord length as the straight blade. The difference in twist angle has two components. The first part is due to the velocity projection, requiring the prebent blade to have a smaller twist angle. The second part is due to the torsional rate, resulting in a decreased twist angle for an upwind prebent blade ($\kappa > 0$) and an increased twist angle for a downwind prebent blade ($\kappa < 0$).

2.7 Local thrust and power coefficients

In the current BEM implementation, only the lift force is included in the iterative convergence calculations, which is the balancing of the momentum and angular momentum between the rotor and the flow. However, the drag force and the sectional

moment also contribute to the aerodynamic loads on the blades, which are calculated in a post-processing step after the momentum balancing iteration has converged. First, the magnitudes of the lift, drag and sectional moment are calculated from the 2-D airfoil polars⁷. The forces are then projected into the blade local coordinate system (BL-sys). Detailed derivations can be found in (Li et al., 2024).

360 The contributions of the drag force to the local thrust and power coefficients are as follows:

$$\begin{aligned}\Delta C_{t,D} &= \frac{N_B f_{D,y}^{\text{BL}} ds}{\frac{1}{2} \rho U_0^2 2\pi r dr} \\ &= C_{t,KJ} \frac{C_D}{C_L} \frac{1}{\|\mathbf{t}^*\|} \left(\frac{\tan \varphi}{\cos^2 \psi^*} + \tan \psi^* \tan \kappa^* \right),\end{aligned}\quad (64)$$

$$\begin{aligned}\Delta C_{p,D} &= \frac{\Omega r N_B f_{D,x}^{\text{BL}} ds}{\frac{1}{2} \rho U_0^3 2\pi r dr} \\ &= -\lambda_r C_{t,KJ} \frac{C_D}{C_L} \frac{1}{\|\mathbf{t}^*\|} \left(\frac{1}{\cos^2 \kappa^*} + \tan \varphi \tan \kappa^* \tan \psi^* \right).\end{aligned}\quad (65)$$

The sectional moment also contributes to the aerodynamic power coefficient as:

$$\Delta C_{p,M} = \frac{N_B \Omega M_y^{\text{BL}} ds}{\frac{1}{2} \rho U_0^3 2\pi r dr} = -\lambda_r C_{t,KJ} \frac{C_M}{C_L} \frac{c^{\text{str}} \tan \kappa^*}{r \cos \varphi},\quad (66)$$

365 where c^{str} is the chord length of the corresponding straight blade, as defined in Eq. (52).

2.7.1 Contribution of the non-circulatory force and moment

In previous work (Li et al., 2022c), it was shown that the airfoil sections of a prebent blade experience an effective torsional motion and an effective mid-chord heaving acceleration due to the projection of the angular velocity and the centrifugal acceleration, originating from the blade rotation. These effects will result in non-circulatory forces and moments, even when the rotor
370 is operating under steady-state conditions. For blades with only prebend and no sweep, it was demonstrated that non-circulatory lift forces due to the effective torsion rate and the heaving acceleration approximately cancel each other under steady-state conditions, resulting in negligible net contributions to thrust and power (Li et al., 2022c). However, the non-circulatory sectional moment and non-circulatory torsion rate drag force, which could also contribute to the aerodynamic power, were not considered significant in that analysis. In this study, non-circulatory forces and moments for generalized curved blades under
375 steady-state conditions are derived. In addition, their contributions to the thrust and power coefficients are analyzed, with detailed derivations provided in Appendix C. Results show that, under steady-state operational conditions, the total contribution of non-circulatory loads to thrust and power is approximately zero. This also confirms that correctly implemented non-circulatory effects do not artificially enhance the rotor's performance or violate the Betz limit.

To validate this conclusion, numerical tests are performed using various curved blade configurations, including backward
380 swept blades, upwind prebent blades and blades combining both backward sweep and upwind prebend. The blade planforms are presented in Sect. 4 and results are detailed in Appendix C.

⁷Following the cross-flow principle (Hoerner and Borst, 1985), the drag force vector aligns with the 2-D sectional flow direction at the 1/4 chord point.

These findings emphasize the importance of correctly including all non-circulatory terms in the 2-D unsteady aerodynamic model. Otherwise, an incomplete implementation with a net contribution from the non-circulatory loads under steady-state conditions could lead to incorrect results. Moreover, the non-circulatory forces and moments generally do not cancel out in unsteady conditions. As a result, a complete implementation is necessary to ensure accurate computation of flutter speeds and other aeroelastic properties.

2.7.2 Total local thrust and power coefficients

Combining the contributions from lift, drag and sectional moment, the total local thrust and power coefficients are derived. For the local thrust coefficient, the approximation can be made when the ratio of C_L/C_D (also known as the glide ratio) is large and the inflow angle φ is small. This is typically satisfied for near-optimal operational conditions and near the blade tip.

$$C_t = C_{t,KJ} + \Delta C_{t,D} \approx C_{t,KJ} \quad (67)$$

$$C_p = C_{p,KJ} + \Delta C_{p,D} + \Delta C_{p,M} \quad (68)$$

For blades with only prebend and no sweep, the local thrust and power coefficients simplify as follows:

$$C_t^{\text{prebend}} = C_{t,KJ} \left(1 + \frac{C_D}{C_L} \tan \varphi \cos \kappa \right) \approx C_{t,KJ}, \quad (69)$$

$$C_p^{\text{prebend}} = C_{p,KJ} - \lambda_r C_{t,KJ} \left(\frac{C_D}{C_L} \frac{1}{\cos \kappa} + \frac{C_M}{C_L} \frac{e^{\text{str}} \tan \kappa}{r \cos \varphi} \right). \quad (70)$$

For blades with only sweep and no prebend, the local thrust and power coefficients are:

$$C_t^{\text{sweep}} = C_{t,KJ} \left(1 + \frac{C_D}{C_L} \frac{\tan \varphi}{\cos \psi^*} \right) \approx C_{t,KJ}, \quad (71)$$

$$C_p^{\text{sweep}} = C_{p,KJ} - \lambda_r C_{t,KJ} \frac{C_D}{C_L} \cos \psi^*. \quad (72)$$

For the special condition that the 1/4 chord line of the blade is straight, the local thrust and power coefficients are in the same form as C_{LT} and C_{LP} derived by Lønbæk et al. (2021):

$$C_t^{\text{str}} = C_{t,KJ} \left(1 + \frac{C_D}{C_L} \tan \varphi \right) \approx C_{t,KJ}, \quad (73)$$

$$C_p^{\text{str}} = C_{p,KJ} - \lambda_r C_{t,KJ} \frac{C_D}{C_L}. \quad (74)$$

For cases where the lift coefficient is zero, such as in the root cylinder part of the blade, the above equations are not valid. In such cases, thrust and power coefficients should be derived using projections, resulting in different expressions. However, this special condition is of limited practical importance and is omitted for brevity.

2.8 Generalization: airfoil alignment and calculation point

In previous sections, the blade's main axis was defined as the 1/4 chord line, with airfoils aligned perpendicularly to this axis. Calculation points were also placed along the 1/4 chord line. These assumptions simplified the derivations and enabled direct

load calculations from velocities in different coordinate systems using vector operations, as detailed in Sect. 2.4. This is because
 410 the lift force should be applied at the 1/4 chord point, perpendicular to the flow at this location ([Bergami and Gaunaa, 2012](#); [Li et al., 2022c](#))
[\(Bergami and Gaunaa, 2012; Pirrung and Gaunaa, 2018; Li et al., 2022c\)](#). However, practical implementations of the BEM method
 may use different definitions for the blade main axis and calculation points. For example, in the aeroelastic code HAWC2
 (Larsen and Hansen, 2007), the main axis aligns along the 1/2 chord line and the 3/4 chord point serves as the calculation
 point.

415 In this section, the previous derivations are generalized to accommodate different definitions of the blade's main axis. The
 airfoils are still assumed to be aligned perpendicular to the main axis, with the cross-flow principle (Hoerner and Borst, 1985)
 applied. In this generalized approach, the main axis is defined as the x_{ma} -chord line of the blade, which can vary along the
 span. For example, airfoils may align with the 1/2 chord line in the blade root (cylinder) region and gradually transition to the
 1/4 chord line toward the blade tip. This flexible representation allows for a more general representation of the actual 3-D blade
 420 geometry. Additionally, the choice of the calculation point is also generalized. With a given blade planform, the choice of the
 calculation point should ideally not influence the final aerodynamic results.

2.8.1 Choice of calculation point

For blades with prebend or coning, the airfoil sections experience an effective torsional motion, as discussed in Sect. 2.2. This
 torsional motion causes the flow angle to vary along the chord. According to unsteady 2-D airfoil theory, flow information at
 425 two locations along the chord should be used: the lift force magnitude is determined using the flow condition at the 3/4 chord
 point, while lift force should be applied at the 1/4 chord point, perpendicular to the flow at this location. [To the best of the
 author's knowledge, it was Øye \(1981\) who firstly explicitly demonstrated these aspects using unsteady 2-D airfoil theory, in
 a technical report written in Danish. These details are also explicitly presented in later works](#) ([Bergami and Gaunaa, 2012](#); [Li
 et al., 2022c](#)). In free-wake lifting-line (LL) methods, total velocities at both the 1/4 and 3/4 chord points can be calculated
 430 directly ([Li et al., 2022c](#)). In the BEM method and other engineering aerodynamic models, however, a constant induced velocity
 for each blade section is typically assumed, with a single chordwise position (the x_{cp} -chord point) chosen as the calculation
 point. The angles of attack at the 1/4 and 3/4 chord points can be approximated from the angle of attack at the calculation
 point (the x_{cp} -chord point), using the effective torsion rate. Numerical studies with the LL method show that the magnitude of
 the 2-D relative velocity V_{rel} is nearly constant along the chord, even for blades with significant prebend and coning ([Li et al.,
 435 2022c](#)). Therefore, the angle of attack at different chordwise positions can be related as follows:

$$\tilde{\alpha}_{3/4} = \alpha_{xc} + \left(\frac{3}{4} - x_{\text{cp}} \right) \frac{\dot{\theta}_c}{V_{\text{rel}}} = \alpha_{xc} + \Delta\alpha_{3/4}, \quad (75)$$

$$\tilde{\alpha}_{1/4} = \alpha_{xc} - \left(x_{\text{cp}} - \frac{1}{4} \right) \frac{\dot{\theta}_c}{V_{\text{rel}}} = \alpha_{xc} - \Delta\alpha_{1/4}. \quad (76)$$

For a given blade planform, the total aerodynamic force and moment at the 1/4 chord point should remain the same, irre-
 spective of the choice of calculation point. Lift, drag and moment coefficients obtained from airfoil polars correspond to using
 440 the 1/4 chord point as the calculation point. When a calculation point other than the 1/4 chord point is used, adjustments are

needed for the force and moment coefficients to ensure that the aerodynamic loads are correctly represented. These adjusted aerodynamic coefficients corresponding to the calculation point at the x_{cp} -chord point are:

$$C_{L,xc} = C_L \cos \Delta\alpha_{1/4} - C_D \sin \Delta\alpha_{1/4} \approx C_L, \quad (77)$$

$$C_{D,xc} = C_D \cos \Delta\alpha_{1/4} + C_L \sin \Delta\alpha_{1/4} \approx C_D + C_L \Delta\alpha_{1/4}, \quad (78)$$

$$C_{M,xc} = C_M + \left(x_{cp} - \frac{1}{4}\right) (C_L \cos \alpha_{xc} + C_D \sin \alpha_{xc})$$

445 $\approx C_M + \left(x_{cp} - \frac{1}{4}\right) C_L. \quad (79)$

The compositions of the force and moment with the calculation point at the 1/4 chord point and at the x_{cp} -chord point are illustrated in Fig. 4.

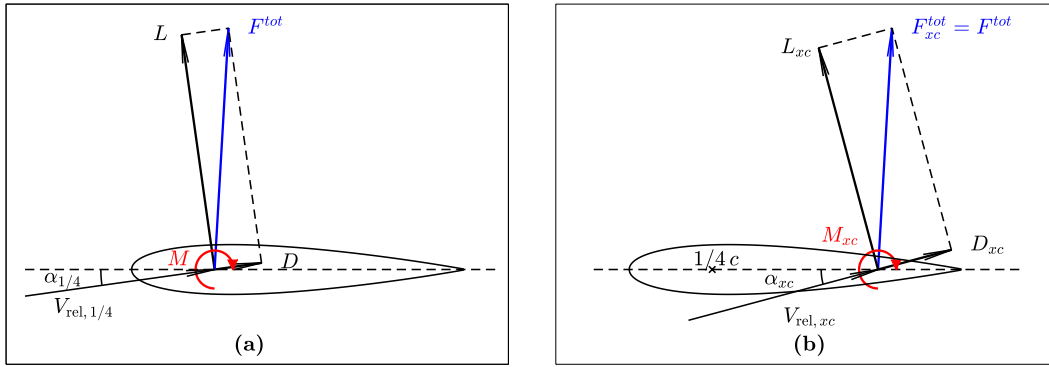


Figure 4. Illustration of the projection of the aerodynamic force with respect to the flow direction at the 1/4 chord point (a) and the x_{cp} -chord point (b). The total sectional force F^{tot} on the airfoil remains the same. The sectional aerodynamic moment from the airfoil polars corresponds to the total sectional moment M evaluated at the 1/4 chord point.

2.8.2 Influence of airfoil alignment

In this section, different airfoil alignments are investigated. Since the choice of the calculation point does not affect the total aerodynamic loads, the calculation points (x_{cp} -chord points) are assumed to coincide with the main axis (at the x_{ma} -chord line) for simplicity. Consequently, velocity vectors and flow angles derived in Sect. 2.2 correspond to the x_{cp} -chord point rather than the 1/4 chord point. The angles of attack at the 1/4 and 3/4 chord points are calculated from the angle at the x_{cp} -chord point using Eqs. (75) and (76). Then, the 2-D force and moment coefficients corresponding to the x_{cp} -chord point are calculated using Eqs. (77) to (79). Substituting these coefficients into Eqs. (67) and (68) provides the local thrust and power coefficients.

455 This also implies that if the blade has prebend, the final equations for the local thrust and power coefficients will differ when the blades are aligned other than the 1/4 chord line. Detailed derivations are omitted for brevity.

The relationships in chord and twist distributions derived in Sect. 2.6 with the main axis being the 1/4 chord line are also generalized. As discussed in Sect. 2.8.1, the 2-D relative velocity magnitude V_{rel} is approximately constant along the chord.

According to Eq. (45), the relationship in chord length between the curved blade and its corresponding straight blade is then identical to that derived in Sect. 2.6.

As shown in Eq. (75), the approximated angle of attack at the 3/4 chord point is calculated from the 2-D flow angle ϕ (at the x_{cp} -chord point), the twist angle β^* in S^* -sys and the additional angle due to the torsion rate $\Delta\alpha_{3/4}$:

$$\tilde{\alpha}_{3/4} = \phi - \beta^* + \Delta\alpha_{3/4}. \quad (80)$$

where, the additional angle $\Delta\alpha_{3/4}$ is the difference between the angle of attack at the 3/4 chord point and the x_{cp} -chord point.

For curved and straight blades, the values of $\Delta\alpha_{3/4}$ are derived from Eq. (75).

$$\Delta\alpha_{3/4}^{\text{cur}} = \left(\frac{3}{4} - x_{cp} \right) \frac{\dot{\theta}_c^{\text{cur}}}{V_{\text{rel}}^{\text{cur}}} \quad (81)$$

$$\Delta\alpha_{3/4}^{\text{str}} = 0 \quad (82)$$

Since the value of $\tilde{\alpha}_{3/4}$ is the same for both blades, the twist angle difference in the S^* -sys is derived:

$$\Delta\beta^* = \beta^{*,\text{cur}} - \beta^{*,\text{str}} = \arctan(\zeta \tan \varphi) - \varphi + \Delta\alpha_{3/4}^{\text{cur}}. \quad (83)$$

Furthermore, the twist angle difference in the S -sys can be calculated using Eq. (56). Assuming small 2-D flow angle ϕ and inflow angle φ in Eq. (57), the twist angle difference is approximated as:

$$\Delta\beta \approx \varphi(\zeta - 1) + \Delta\alpha_{3/4}^{\text{cur}} - \Delta\theta_z \quad (84)$$

For the special condition of a blade with only prebend, the twist angle difference is derived, differing from the case when using the 1/4 chord line as the main axis:

$$\Delta\beta \approx \varphi(\cos \kappa - 1) - \left(\frac{3}{4} - x_{cp} \right) \frac{\Omega c}{V} \sin \kappa. \quad (85)$$

In summary, when the airfoils are aligned differently than the 1/4 chord line, the chord distribution relationship between curved and straight blades remains the same. However, the twist distribution relationship is affected by the choice of the airfoil alignment, particularly when the blade has prebend or coning. Prebent blades with the same main axis geometry, chord and twist distributions but different airfoil alignments (e.g., aligned to the 1/2 chord line versus the 1/4 chord line) will result in different angles of attack and thus different loads. This difference may become significant for blades with large prebend or coning, highlighting the importance of consistent airfoil alignment definitions in aerodynamic or aeroelastic analyses for prebent or coned blades.

2.9 Summary: modifying chord and twist to remove projection effects

This section summarizes the final equations for determining the chord and twist distributions of a curved blade within the BEM framework, ensuring the same bound circulation as that of a given straight baseline blade.

The approximations presented in Sect. 2.6.1, which assume a small inflow angle ϕ , are applied here. These approximations will be validated in Sect. 4 and shown to be sufficient. For reference, equations without these approximations are provided in Sect. 2.6 and 2.8, following similar calculation steps. The procedure for determining the chord and twist distributions of a curved blade, given its main axis geometry, consists of five steps:

- 490 – Using the given chord and twist distributions of the baseline straight blade (c^{Str} and β^{Str}), solve for the converged induced velocities using the BEM method.
- Compute the flow angles φ and ϕ , along with their tangent ratio ζ , using Eqs. (15), (19) and (48). Determine the 2-D relative velocity of the straight blade $V_{\text{rel}}^{\text{Str}}$ using Eq. (18).
- Apply the approximation $\mu \approx \zeta$ and calculate the chord length and the 2-D relative velocity of the curved blade (c^{cur} and
495 $V_{\text{rel}}^{\text{cur}}$) using Eqs. (58) and (51).
- Compute the effective torsion rate $\dot{\theta}$ using Eq. (24), the change in angle of attack at the 3/4 chord point $\Delta\alpha_{3/4}^{\text{cur}}$ using Eq. (81), and the additional twist angle $\Delta\theta_z$ using Eq. (11).
- Finally, determine the twist angle β^{cur} using Eq. (84).

3 Models for comparison

500 In the present work, the high-fidelity Navier–Stokes solver EllipSys3D (Michelsen, 1992, 1994; Sørensen, 1995) and the low-fidelity BEM method are used for comparison. Key details regarding the model setups are provided below.

3.1 Reynolds-averaged Navier–Stokes (RANS) solver

The incompressible, pressure-based, three-dimensional solver EllipSys3D is used to solve the Reynolds-averaged Navier–Stokes (RANS) equations with finite volume discretization. The boundary conditions at the outer domain limit adopt an in-
505 let/outlet strategy, and the $k-\omega$ SST model (Menter, 1994) is applied, assuming fully turbulent flow.

Rotor-resolved meshes are generated in two consecutive steps, fully scripted to maintain grid quality consistently. First, a structured surface mesh of the blade is generated using the PGLW tool (Zahle, 2019), with 128 spanwise and 256 chordwise cells. This surface mesh is then radially extruded into a volume grid using the hyperbolic mesh generator Hypgrid (Sørensen, 1998). A total of 256 cells are used in this process, and the resulting outer domain size is approximately 11 rotor diameters.
510 Boundary layer clustering is applied, with an imposed first cell height of 1×10^{-6} m, targeting y^+ values below one. The resulting volume meshes account for a total of 14.2 million cells. The grid topology of the baseline straight blade is detailed in (Li et al., 2022b).

Although a steady solver is employed, the solver struggles to converge the solution as it gets stuck in limit cycles, particularly near the blade root and maximum chord where both the angle of attack and the airfoil’s relative thickness are high. Unlike
515 previous studies (Li et al., 2022b, d), which averaged CFD results over the last 350 iterations, the present work averages the last

50 iterations, resulting in increased load variation near the root. It is possible to apply convergence enhancement methods to the RANS CFD solver, such as the modified-BoostConv method (Dicholkar et al., 2022, 2024)(Dicholkar et al., 2022, 2024, 2025), to improve the convergence in the root region. However, since the blade geometry at the tip region has negligible impact on the root region, the current results are sufficient for the present study.

520 3.2 BEM method

The BEM method is used as the low-fidelity aerodynamic model, serving as the baseline for comparison. The BEM method implemented in the standalone BEVC code (Li et al., 2022b) is used, which is based on the HAWC2 aerodynamic module (Larsen and Hansen, 2007). The implementation uses a steady-state approach, meaning the polar-grid approach available in the HAWC2 code (Madsen et al., 2020a) for unsteady simulations or non-uniform inflow is not used. Detailed descriptions of the coordinate systems and projections of velocities and loads are discussed in Sect. 2. The unsteady 2-D aerodynamic model is also included, as the airfoil of prebent blades experience effective torsional motion and heaving acceleration, even at steady-state operational conditions, as shown in Sect. 2.2. The complete implementation of the model is used, despite contributions due to non-circulatory forces and moments approximately cancel out, as discussed in Appendix C. As described in Sect. 2.7, only the lift force is used in the momentum balancing calculation. After the convergence is reached, the profile drag and the sectional moment are also included in the load calculation. The relationship between the axial induction factor and the thrust coefficient follows the polynomial relationship in Eq. (39) by Madsen et al. (2020a). Prandtl's tip-loss correction (Glauert, 1935; Sørensen, 2015) is applied to account for increased blade axial induction compared to the annulus-averaged value near the tip, due to the effect of the finite number of blades. The airfoil data used in the BEM method is from 2-D fully turbulent CFD results (Bortolotti et al., 2019) and simulations (Bortolotti et al., 2019), using EllipSys2D with the same turbulence model ($k-\omega$ SST) as employed in the 3-D CFD simulations described in Sect. 3.1. In previous benchmark studies (Barlas et al., 2022; Horcas et al., 2023; Zahle et al., 2024), BEM and other engineering aerodynamic models using the same 2-D airfoil data have shown good agreement with 3-D CFD results from EllipSys3D. This consistency provides a solid foundation for comparing BEM and CFD results in the present work. In the present study, each blade is radially discretized into 80 sections for the BEM calculation.

540 4 Results

This section presents numerical results using both the BEM method and the high-fidelity RANS CFD solver (referred to as CFD). The primary objective is to numerically demonstrate that using the modified curved blades with adjusted chord and twist distributions leads to more consistent and meaningful comparisons than previous setups. This study revisits previous work on blades with only sweep (Li et al., 2022d) and only prebend (Li et al., 2022b) and extends the analysis to generalized curved blades combining both sweep and prebend.

4.1 Rotor configuration for comparison

The numerical tests use blades based on the IEA-10.0-198 10 MW reference wind turbine (RWT) (Bortolotti et al., 2019), consistent with previous studies (Li et al., 2022b, d). The main axis is defined as the half-chord line of the blade and the airfoils are aligned perpendicular to this main axis. The baseline straight blade is obtained by removing the prebend and sweep from the original RWT blade, resulting in a straight half-chord line. The blade length is 96.2 m with a hub radius of 2.8 m, giving a total rotor radius of 99 m. For all test cases, the rotor operates under steady-state conditions with a zero cone angle and uniform inflow perpendicular to the rotor plane, implying no yaw error or rotor tilt. The blades are assumed to be rigid, excluding elastic deformation effects.

4.2 Operational conditions

The operational conditions used in this study align with previous work (Li et al., 2022b, d). Initially, an optimal operational condition with high rotor thrust is used for comparison. The rotors operate under a uniform inflow of 8 m s^{-1} with a constant rotational speed of 0.855 rad s^{-1} and zero blade pitch angle. For the rotor with baseline straight blades, the tip speed ratio is 10.58, the [rotor](#) thrust coefficient is 0.90 and the rotor power coefficient is 0.46, as predicted by the BEM method. Additionally, comparisons are made under operational conditions corresponding to lower thrust coefficients. Three lower-loading operational conditions defined in the IEA Wind TCP Task 37 report (Bortolotti et al., 2019) are used, with a rotational speed of 0.909 rad s^{-1} , wind speeds varying from 12.0 m s^{-1} to 20.0 m s^{-1} and the blade is pitched towards lower loadings. The operational conditions are summarized in Table 1, which also includes the rotor thrust and power coefficients predicted by the BEM method for the baseline straight blade. For brevity, the operational conditions are represented by the wind speeds in subsequent discussions.

Table 1. Operational conditions used in the comparison. $C_{T,\text{BEM}}^{\text{str}}$ and $C_{P,\text{BEM}}^{\text{str}}$ are the thrust and power coefficients predicted by the BEM method for the baseline straight blade.

Wind speed U_0 [m s^{-1}]	Tip-speed-ratio λ [-]	Pitch angle θ_p [$^\circ$]	$C_{T,\text{BEM}}^{\text{str}}$ [-]	$C_{P,\text{BEM}}^{\text{str}}$ [-]
8.0	10.58	0.00	0.90	0.46
12.0	7.50	5.98	0.42	0.32
15.0	6.00	11.77	0.21	0.17
20.0	4.50	18.51	0.09	0.07

4.3 Planform of curved blades

Two sets of curved blades are used for comparison: the original curved blades and the modified curved blades. [The blade naming convention used to identify blade type, curve configuration and operating condition throughout this study is summarized in Table 2. Further details for each blade type are provided in the following sections.](#)

Table 2. Naming convention for curved blades used in this study. The prefix and suffix are optional, depending on blade type and operating condition. In each example, the relevant element is highlighted in bold for clarity.

Notation element	Example	Meaning / usage
Prefix “m” (optional)	m B-1	modified blade: chord/twist adjusted to remove projection effect
Geometry type	m B -1, m W -5, m C -15	B=swept; W=prebent; C=combined
Curve index	B -1, W -5, C -15	Curve shape identifier
Suffix “Uv” (optional)	m B-1- U12	Operating condition: wind speed $v \text{ m s}^{-1}$

4.3.1 Original curved blades

570 The original curved blades follow the configurations used in previous studies (Li et al., 2022b, d), with the same chord and twist distributions as the baseline straight blade for blade sections with the same z^B -coordinates. The main axis geometries of these curved blades are modified from the baseline straight blade by adding x^B -components for blade sweep and by adding y^B -components for blade prebend, while keeping the z^B -coordinates unchanged. For blades with sweep (x^B -component), the radius will be increased compared to the baseline straight blade.

575 Following previous studies (Li et al., 2018, 2022b, d), the main axis geometry is defined using a modified Bézier curve parameterized by the curve ratio \bar{r}_c , the curve magnitude Δd and the tip curve angle Λ_{tip} , as illustrated in Fig. 5.

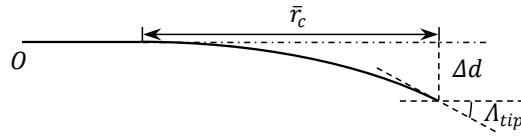


Figure 5. Parameterization of the curved blade with curve ratio \bar{r}_c , curve magnitude Δd and tip curve angle Λ_{tip} , adapted from Li et al. (2018).

For the optimal operational condition at 8 m s^{-1} with high rotor loading and zero blade pitch, several blades were used for comparison in previous studies. The study on swept blades (Li et al., 2022d) used four different backward swept blades, labeled Blade-1 to Blade-4. In addition, four forward swept blades, labeled Blade-5 to Blade-8, with the same curve parameters as Blade-1 to Blade-4 but opposite sweep directions, were also introduced. These swept blades with different sweep magnitudes and tip sweep angles were introduced to represent different possible swept blade shapes. In the present work, they are abbreviated as B-1 to B-8 and referred to as the original swept blades. In the previous study on prebent blades (Li et al., 2022b), the main axis geometries of the prebent blades (labeled W-1 to W-8) are identical to the swept blades (B-1 to B-8), but with the curvature applied in the prebend direction (y^B -direction) instead of sweep (x^B -direction). The original prebent blades W-1 to W-4 feature upwind prebend and W-5 to W-8 feature downwind prebend. The parameters of these curved blades are summarized in Table 3.

Table 3. Parameters of the planforms of the curved blades. Only the first set of curved blades is used for comparison in the present study.

Swept blades	Prebent blades	\bar{r}_c	Δd	Λ_{tip}
B-1 / B-5	W-1 / W-5	50%	10%	20°
B-2 / B-6	W-2 / W-6	50%	10%	40°
B-3 / B-7	W-3 / W-7	25%	5%	20°
B-4 / B-8	W-4 / W-8	25%	5%	40°

In this study, the focus is on the first set of curved blades: swept blades B-1 and B-5; prebent blades W-1 and W-5. The front view of the swept blades B-1 and B-5 is illustrated in Fig. 6. The top view of the prebent blades W-1 and W-5 is shown in
 590 Fig. 7.

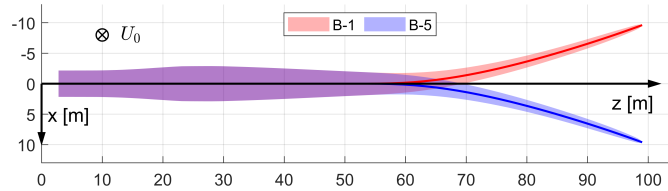


Figure 6. Front view of the backward swept blade B-1 and forward swept blade B-5, with main axes highlighted, in the blade root coordinate system (B-sys). This corresponds to the front view of the rotor with the blade pointing east. The free-stream wind velocity vector is also shown.

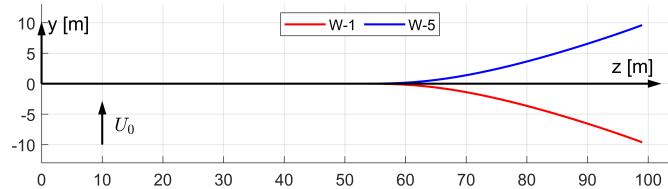


Figure 7. Top view of the main axis geometries of upwind prebent blade W-1 and downwind prebent blade W-5, in the blade root coordinate system (B-sys). This corresponds to the top view of the rotor with the blade pointing east. The free-stream wind velocity vector is also shown.

It has been tested that other swept and prebent blades with different main axis curved shapes exhibit similar behaviors to the curved blades used in the present work. Including these additional results will not change the conclusions of the present work. The results of other swept and prebent blades are summarized in an internet appendix (Li et al., 2025).

For operational conditions corresponding to lower thrust coefficients in Table 1, blade pitching effects are introduced as
 595 an additional constant twist angle offset, rather than a rotation around the pitch axis (z^B -axis). This approach maintains the blade's 3-D main axis coordinates in B-sys. For these lower-loading cases, the original swept blades based on B-b are labeled

as B-b-U v , where b is the swept blade index and v is the wind speed in m s^{-1} . Similarly, the original prebent blades based on W-w are labeled as W-w-U v , where w is the prebent blade index.

4.3.2 Modified curved blades

600 The modified curved blades have their chord and twist distributions adjusted based on the original curved blades, following the relationships derived in Sect. 2.6. These modifications ensure that the BEM method predicts these modified curved blades to have the same circulation distribution as the corresponding baseline straight blades. Further, the loads due to the lift force will also be identical between curved and straight blade; only negligible differences due to the drag force remain. These modified blades are expected to allow for consistent comparisons by subtracting the projection effects, thereby highlighting the effects
605 of wake geometry on inductions and resulting loads. Since the main axis is defined along the half-chord line, the generalized chord and twist distribution relationships derived in Sect. 2.8 with $x_{cp} = 0.5$ are applied. The approximations presented in Sect. 2.8.2 are used, which will be shown to be sufficient for this study.

For the swept blades, two modifications are applied to the original swept blades. First, the main axis geometries are scaled such that each blade section has the same radius as the corresponding section of the baseline straight blade. Second, the chord
610 lengths and twist angles are modified according to Eqs. (60) and (61). Specifically, both the chord length and the twist angle are increased. The original swept blades B-b are modified into mB-b, and the original swept blades B-b-U v for lower loading conditions are modified into mB-b-U v .

For the prebent blades, since the radii are already identical to the baseline straight blade, scaling of the main axis geometry as done for the swept cases is not necessary. Using the approximated relationship in Sect. 2.8.2, the chord distribution remains
615 unchanged from the original prebent blades. However, the twist angles are adjusted according to Eq. (85), with the condition of $x_{cp} = 0.5$ for the current setup. The original prebent blades W-w are modified into mW-w, and the original prebent blades W-w-U v for lower loading conditions are modified into mW-w-U v .

Figure 8 illustrates the planform modifications applied to the swept and prebent blades in terms of chord length and twist angle. Only the outboard region of the blade (from a radius of 50 m to the blade tip) is shown, as the chord and twist remain unchanged in the straight inboard portion of the blade. Panel (a) shows the chord length offset relative to the baseline straight blade⁸. For the modified swept blades (mB-1 and mB-5), the chord length is increased in the swept region, consistent with Eq. (60). In contrast, the modified prebent blades (mW-1 and mW-5) have the same chord distribution as the baseline straight blade, in agreement with Eq. (62). As also indicated in the figure, the chord length does not change with wind speed, which is as expected. Panel (b) presents the twist angle offset $\Delta\beta$ for the modified swept and prebent blades across different wind
620 speeds. The modified swept blades consistently show an increased twist angle, while the modified prebent blades generally show a reduced twist. An exception occurs at the optimal condition of 8 m s^{-1} , where the modified upwind prebent blade mW-1 shows a slight increase in twist in the mid-span region due to the torsional rate term. The overall magnitude of the twist angle offset $\Delta\beta$ increases with wind speed, consistent with the corresponding increase in flow angle ϕ . Overall, the trends on the twist angle offsets observed in panel (b) are consistent with the formulations provided in Eqs. (61) and (85).

⁸Equivalent to the offset relative to the original swept and prebent blades.

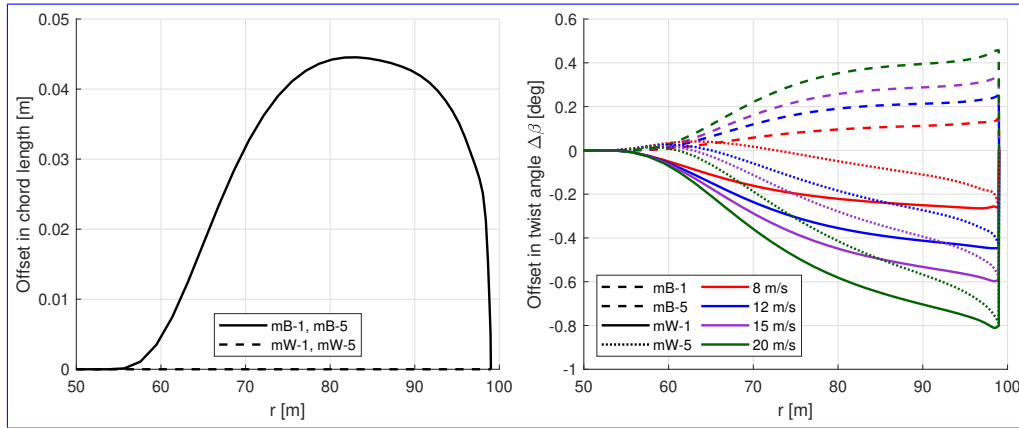


Figure 8. Offset in chord length (panel a) and twist angle $\Delta\beta$ (panel b) of modified swept blades mB-1 and mB-5, as well as modified prebent blades mW-1 and mW-5 compared to the baseline straight blade. The swept blades mB-1 and mB-5 have identical chord and twist distributions for different wind speeds.

630 In comparison, Gözcü and Verelst (2020) reported the blade tip torsional deformations between 1.0° and 2.3° in aeroelastic simulations of the IEA 10MW RWT blade for the operational conditions used in the present work. Therefore, the twist modifications applied here are, on average, approximately five times smaller than the aeroelastic torsional deformations.

4.3.3 Blades with sweep and prebend combined

Curved blades combining both sweep and prebend are also introduced to investigate generalized curved blade configurations. First, curved blades that are generated using similar ideas as the original swept and prebent blades described in Sect. 4.3.1 are referred to as the original curved blades. The main axis geometry of the original curved blade is adjusted from the baseline straight blade: the x^B - and y^B -coordinates are adjusted to allow sweep and prebend, while the z^B -coordinate remains unchanged. The chord, twist and relative thickness distributions remain the same as the baseline blade for blade sections with the same z^B -coordinates. In the present work, the original curved blades are generated by superimposing the main axis geometries of the original swept blades and the original prebent blades. These original combined curved blades are labeled as C-bw, where b and w are the indices of the corresponding original swept blade B-b and prebent blade W-w. Four cases are used for comparison in this study, which are C-11, C-55, C-15 and C-51, representing combinations of the swept blades B-1 and B-5 and the prebent blades W-1 and W-5. Specifically, blade C-11 has backward sweep and upwind prebend; blade C-55 has forward sweep and downwind prebend; blade C-15 has backward sweep and downwind prebend and blade C-51 has forward sweep and upwind prebend.

645 These four cases are representative, covering all possible combinations of sweep and prebend directions. Furthermore, they correspond to different combinations of load redistribution effects observed in previous studies (Li et al., 2022b, d). For example, the influences of backward sweep and upwind prebend have similar patterns for the spanwise load redistribution, which are in opposite directions to the influence due to forward sweep and downwind prebend. Consequently, the influence of

650 wake geometry on loads is expected to be more pronounced for blades C-11 and C-55 due to the expected superpositioning of load redistribution effects. In contrast, for blades C-15 and C-51, the influence of wake geometry on loads is expected to be weaker, since the sweep and prebend effects oppose each other and are expected to partially cancel out.

The original curved blades are modified into the modified curved blades for a consistent comparison, where two modifications are necessary. First, the main axis geometry is scaled to match the radius of each section of the baseline straight blade. 655 Second, the chord and twist distributions are adjusted according to Eqs. (52) and (83), with the condition $x_{cp} = 0.5$ applied. The original curved blades C-bw are modified into mC-bw, and the original curved blades C-bw-Uv for lower loading conditions are modified into mC-bw-Uv.

It has been tested that other combined curved blades with different main axis curved shapes exhibit similar behaviors to the curved blades used in the present work. Their results are summarized in an internet appendix (Li et al., 2025).

660 4.4 Loads for comparison

In previous studies (Li et al., 2022b, d), aerodynamic loads were directly presented and compared using dimensioned values. In the present work, non-dimensional loads are used to provide a clearer representation of the relative changes between curved and straight blades. Different non-dimensional load definitions are used for the original and modified setups to ensure meaningful comparisons. This distinction is made because, in the original setup, the z^B -coordinate length is fixed at 99 m, while in the 665 modified setup, the radius⁹ is fixed at 99 m. Additionally, in previous studies involving blades with only sweep or prebend, the original setup used loads in the y^B - and x^B -directions for comparison. For the modified setup, however, loads in the y^{BL} - and x^{BL} -directions are more physically meaningful, since the x^{BL} -direction aligns with the tangential direction.

4.4.1 Comparison for original curved blades

In previous work on swept blades (Li et al., 2022d), loads in the y^B - and x^B -directions in the blade root coordinate system 670 (B-sys) were referred to as the out-of-plane and in-plane loads, respectively. In the present work, they are non-dimensionalized into a local thrust coefficient and a simplified local power coefficient, defined as:

$$C_t(z^B) = \frac{N_B f_y^B ds}{\frac{1}{2} \rho U_0^2 2\pi z^B dz}, \quad (86)$$

$$\hat{C}_p(z^B) \equiv \frac{\Omega z^B N_B f_x^B ds}{\frac{1}{2} \rho U_0^3 2\pi z^B dz}. \quad (87)$$

Here, the simplified local power coefficient \hat{C}_p represents the contribution of the in-plane force f_x^B to the power, acknowl- 675 edging that the in-plane force is not perpendicular to the radial direction and that other loads also contribute to the power.

To highlight differences between the curved and straight blades, offsets in the non-dimensional loads are used for comparison. These offsets are the difference in loads between the original curved blade and the baseline straight blade, evaluated at the

⁹Equivalent to the z^{BL} -coordinate length.

same z^B -coordinate:

$$\Delta C_t(z^B) = C_t^{\text{cur}}(z^B) - C_t^{\text{str}}(z^B), \quad (88)$$

$$680 \quad \Delta \hat{C}_p(z^B) = \hat{C}_p^{\text{cur}}(z^B) - \hat{C}_p^{\text{str}}(z^B). \quad (89)$$

As shown by Lønbæk et al. (2021), the rotor-integrated thrust and simplified power coefficients can be calculated from the local thrust and simplified power coefficients.

$$C_T = \frac{2}{R^2} \int_0^{z_{\text{tip}}^B} z^B C_t(z^B) dz^B, \quad (90)$$

$$\hat{C}_P \equiv \frac{2}{R^2} \int_0^{z_{\text{tip}}^B} z^B \hat{C}_p(z^B) dz^B. \quad (91)$$

685 4.4.2 Comparison for modified curved blades

In the present work, the axial and tangential loads are defined as the loads in the y^{BL} - and x^{BL} -directions in the blade local coordinate system (BL-sys). With this definition, the axial load is normal to the rotor plane and the tangential load is perpendicular to the radial direction at each blade section. These loads are non-dimensionalized into the local thrust coefficient and a simplified local power coefficient:

$$690 \quad C_t(r) = \frac{N_B f_y^{\text{BL}} ds}{\frac{1}{2} \rho U_0^2 2\pi r dr}, \quad (92)$$

$$\tilde{C}_p(r) \equiv \frac{\Omega r N_B f_x^{\text{BL}} ds}{\frac{1}{2} \rho U_0^3 2\pi r dr}. \quad (93)$$

The simplified power coefficient in Eq. (93) represents the contribution of the tangential force to power. Note that other loads, such as sectional moments, also contribute to aerodynamic power. In the following sections, the local thrust coefficient and the simplified local power coefficient are referred to as thrust coefficient and power coefficient for brevity.

695 While the thrust coefficients in Eqs. (86) and (92) can be directly compared, the simplified power coefficients in Eqs. (87) and (93) correspond to loads in slightly different directions. For blades without sweep, where there is no x^B -component in the main axis, the blade root coordinate system (B-sys) will coincide with the blade local coordinate system (BL-sys). In this case, Eqs. (86) and (87) will be identical to Eqs. (92) and (93).

700 To highlight the influence of curved blade geometry on the loads, the offsets of the non-dimensional loads are used for comparison. They are the load differences between the modified curved blade and the baseline straight blade at the same radial positions:

$$\Delta C_t(r) = C_t^{\text{cur}}(r) - C_t^{\text{str}}(r), \quad (94)$$

$$\Delta \tilde{C}_p(r) = \tilde{C}_p^{\text{cur}}(r) - \tilde{C}_p^{\text{str}}(r). \quad (95)$$

For the modified curved blades, the rotor-integrated thrust and simplified power coefficients are calculated as:

$$705 \quad C_T = \frac{2}{R^2} \int_0^R r C_t(r) dr, \quad (96)$$

$$\tilde{C}_P \equiv \frac{2}{R^2} \int_0^R r \tilde{C}_p(r) dr. \quad (97)$$

4.4.3 Subtracting the projection effects in CFD results using BEM method

This section introduces a method to adjust the CFD results of the original curved blades by subtracting the projection effects estimated using the BEM method. For the original curved blade, which has the same chord and twist distributions as the
710 baseline straight blade, the CFD results include contributions from both projection and wake-induced effects. In contrast, the BEM results should only have the influence due to projections. Thus, the difference in loads between the original curved blade and the corresponding modified curved blade in the BEM results provides an estimation of the projection effects. Subsequently, the CFD results of the original curved blades can be adjusted by subtracting the estimated projection effects:

$$\Delta C_{t,\text{CFD}-\Delta\text{BEM}}(z^B) \equiv \Delta C_{t,\text{CFD}}^{\text{origin}}(z^B) - \left(C_{t,\text{BEM}}^{\text{origin}}(z^B) - C_{t,\text{BEM}}^{\text{mod}}(r) \right), \quad (98)$$

$$715 \quad \Delta \hat{C}_{p,\text{CFD}-\Delta\text{BEM}}(z^B) \equiv \Delta \hat{C}_{p,\text{CFD}}^{\text{origin}}(z^B) - \left(\hat{C}_{p,\text{BEM}}^{\text{origin}}(z^B) - \tilde{C}_{p,\text{BEM}}^{\text{mod}}(r) \right). \quad (99)$$

Since the modified curved blade has the same radius as the baseline straight blade, while the original curved blade has the same z^B -coordinate as the baseline, the subtraction is conducted for the corresponding abscissas.

The adjusted CFD results of the original curved blades are expected to closely match the CFD results of the modified curved blades, effectively isolating the wake-induced effects for a more consistent comparison.

720 4.5 Baseline straight blade

Before comparing the curved blades, the thrust and power coefficients of the baseline straight blade operating at 8 m s^{-1} predicted by the BEM method and the CFD solver are firstly shown in Fig. 9. These results correspond to Eqs. (86) and (87) or Eqs. (92) and (93), as the blade root coordinate system (B-sys) and the blade local coordinate system (BL-sys) coincide for the straight blade configuration.

725 In the blade root region, the difference is relatively large for loads in both direction, primarily due to unsteady flow separation effects in this region. Therefore, the focus of the comparison is on the region from a radius of 20 m to the blade tip.

For the thrust coefficient, the BEM and CFD predictions are in close agreement. According to the Kutta–Joukowski analysis presented in Sect. 2.4, the similarity in thrust indicates that the bound circulation distributions predicted by both methods are very similar. However, discrepancies are observed in the power coefficient, where the BEM method tends to over-predict the
730 tangential loads, especially from a radius of 60 m to the blade tip. This discrepancy is likely related to the empirical nature of the tip loss and high-thrust corrections implemented in the BEM method. Specifically, the BEM method relies on the empirical

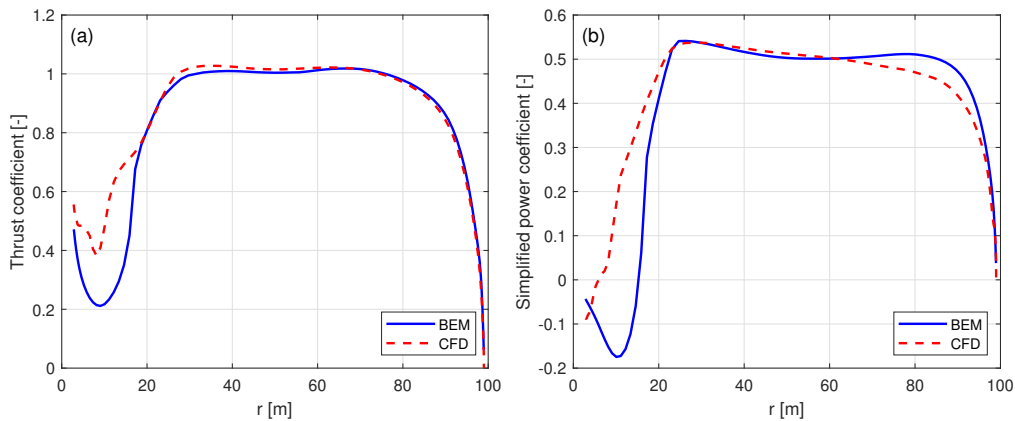


Figure 9. Thrust coefficient C_t (panel a) and simplified power coefficient \tilde{C}_p (panel b) of the baseline straight blade, calculated using the BEM method and the CFD solver, at a wind speed of 8 m s^{-1} .

Prandtl's tip-loss correction that do not account for wake expansion and wake roll-up, which can significantly influence tip flow behavior at high-loading conditions. Similarly, the empirical polynomial $a - C_t$ relationship is used at this high-thrust condition. In contrast, the CFD solver is modeling the tip effects with much higher fidelity, since the flow around the 3-D blade geometry is fully resolved and does not require an empirical high-thrust correction.

For operational conditions with higher wind speeds and lower thrust coefficients, as listed in Table 1, the results are presented in Appendix D1. As the wind speed increases and the rotor loading decreases, the agreement between the BEM and CFD results generally improves for both thrust and power coefficients. This improvement is due to the reduced induction effects and lower uncertainty in the $a - C_t$ relationship in the lower-thrust region.

740 4.6 Revisit of the swept blade cases Blades with only sweep

This section ~~revisits the previous study on~~ examines blades with only sweep and no prebend, revisiting the previous study presented in (Li et al., 2022d). In that work, comparisons were made using various aerodynamic models, including the BEM method, the CFD solver, the lifting-line method and a mid-fidelity engineering model developed in that study to improve swept blade modeling. The comparisons were conducted using the original swept blades, which have the same chord and twist distributions as the baseline straight blade. The primary objectives were to investigate the impact of blade sweep on wake geometry and the consequent effects on loads and to demonstrate the improved agreement of the new model with CFD and lifting-line methods in modeling blade sweep effects. In the present work, results from both the original and the modified swept blades are used for the comparison.

4.6.1 Optimal operational condition

750 The optimal operational condition with a uniform inflow velocity of 8 m s^{-1} is firstly used for comparison. The offsets in thrust and power coefficients for both the original and modified swept blades, compared to the baseline straight blade, are plotted in

Figs. 10 and 11. For the original swept blades B-1 and B-5, the load offsets ΔC_t and $\Delta \hat{C}_p$ are calculated using Eqs. (88) and (89) and plotted against the z^B -coordinates. For the modified swept blades mB-1 and mB-5, the load offsets ΔC_t and $\Delta \tilde{C}_p$ are calculated using Eqs. (94) and (95) and plotted against the radius. In addition, the adjusted CFD results of the original swept blades, obtained by subtracting the BEM thrust and power differences between original and modified blades, Eqs. (98) and (99), are included for comparison.

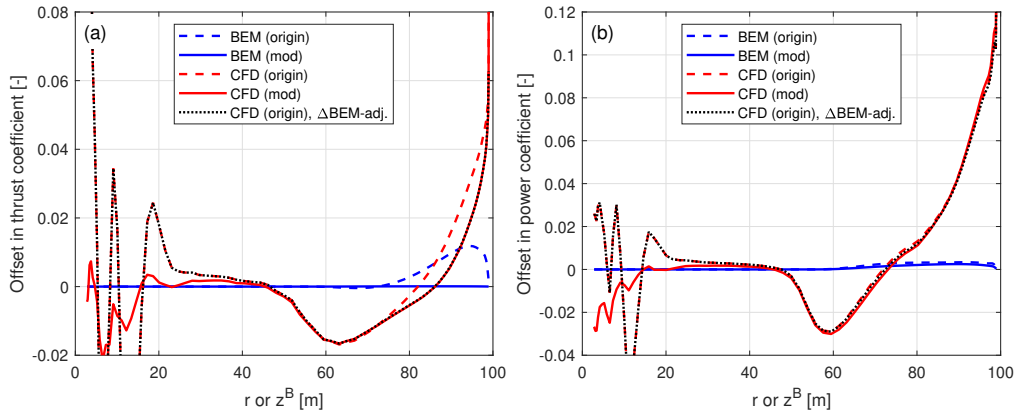


Figure 10. Offset in thrust coefficient ΔC_t (panel a) and simplified power coefficients $\Delta \tilde{C}_p$ and $\Delta \hat{C}_p$ (panel b) of the original backward swept blade B-1 and the modified backward swept blade mB-1, compared to the baseline straight blade, at a wind speed of 8 m s^{-1} .

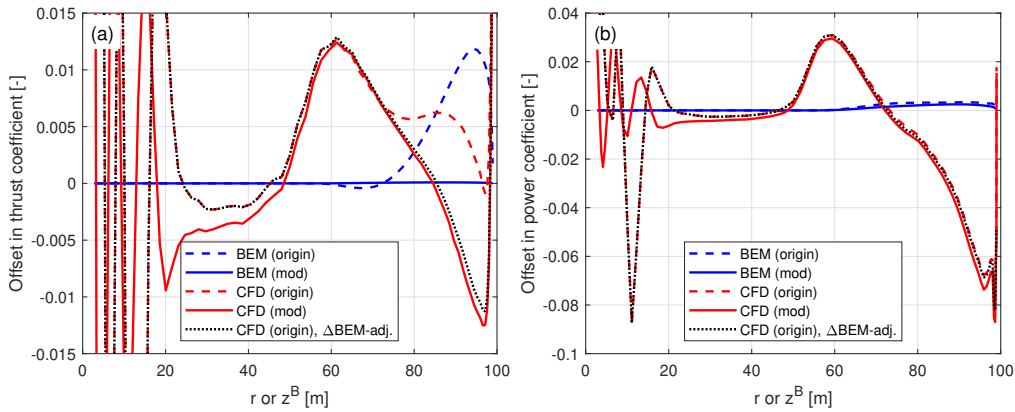


Figure 11. Offset in thrust coefficient ΔC_t (panel a) and simplified power coefficients $\Delta \tilde{C}_p$ and $\Delta \hat{C}_p$ (panel b) of the original forward swept blade B-5 and the modified forward swept blade mB-5, compared to the baseline straight blade, at a wind speed of 8 m s^{-1} .

For the original swept blades, the load offsets predicted by the BEM method are due to the projection effects. Specifically, the thrust coefficient offsets for B-1 and B-5 predicted by the BEM method show a small increase, both reaching a maximum magnitude of only approximately 0.01 at the z^B -coordinate of 94 m. The power coefficient offsets predicted by the BEM method are approximately zero. This suggests that the projection effects are small for these original swept blades, indicating that they

operate under similar conditions to the baseline straight blade. For the modified swept blades mB-1 and mB-5, the offsets in both thrust and power coefficients predicted by the BEM method are approximately zero throughout the span, confirming that the projection effects are effectively subtracted. This validates the modifications to the chord and twist distributions derived in Sect. 2.6.1 as well as the approximations made in Sect. 2.8.2.

765 The CFD results include the impact of changed wake geometries on the aerodynamics, as evidenced by the larger load offsets between the modified swept blades (mB-1 and mB-5) and the baseline straight blade. For the inboard part of the swept blade (radius less than 50 m), where the main axis is still straight, the loads are approximately identical to those of the baseline straight blade. In the swept part of the blade (radius greater than 50 m), a distinctive spanwise load redistribution pattern is observed. For the backward swept blade mB-1, when moving towards the blade tip, the load is initially lower compared to the
770 baseline straight blade until approximately halfway until the blade tip (radius of 80 m). Subsequently, when moving further towards the tip, the load increases and becomes higher compared to the baseline straight blade until the blade tip. For the forward swept blade mB-5, an opposite load redistribution pattern is observed. These load redistribution patterns for the swept blades are consistent with observations from previous studies (Li et al., 2020, 2022d). For the swept blades, both projection and wake-induced effects are concentrated in the outboard half of the span. This is because for the swept blades used in this
775 study, the blade sweep begins only from the mid-span, and the inboard section remains straight.

The performance of using the CFD results of the original swept blades (B-1 and B-5) to investigate the wake-induced effects of the swept blade, as has been done in previous work (Li et al., 2022d), is also analyzed. As shown in Figs. 10 and 11, the power coefficient offsets are almost identical between the original and modified setups. For the thrust coefficient, the offsets are slightly increased for both original swept blades due to projection effects. For the original backward swept blade B-1, a
780 load redistribution pattern is still observed, although it is slightly altered by the projection effects. In contrast, for the original forward swept blade B-5, the load redistribution effect in the thrust coefficient is not observed. Instead, the thrust coefficient is consistently increased from a radius of 50 m to the blade tip. The CFD results of the original swept blades adjusted using BEM results according to Eqs. (98) and (99), labeled as "CFD(origin), Δ BEM-adj." in the figure, show good agreement with the CFD results of the modified swept blades. This indicates that the projection effects in the CFD and BEM results are similar
785 for swept blades and can be effectively subtracted using this adjustment¹⁰.

4.6.2 Lower loading conditions

In the previous work (Li et al., 2022d), only the optimal operational condition at 8 m s^{-1} was considered. This study extends the analysis to lower loading conditions, as listed in Table 1. Results for the backward swept blades B-1-Uv and mB-1-Uv ~~under~~
~~these conditions~~ at a wind speed of 20 m s^{-1} (lowest loading condition) are presented in Fig. 12, while results at intermediate
790 conditions (12 and 15 m s^{-1}) are presented in Fig. D2 in Appendix D2¹¹. Similar conclusions apply to the forward swept blades B-5-Uv and mB-5-Uv, which are therefore not shown in this study.

¹⁰This also suggests that the cross-flow principle used in the BEM method performs well for swept blades.

¹¹For completeness and ease of comparison, Fig. D2 also includes results at 20 m s^{-1} .

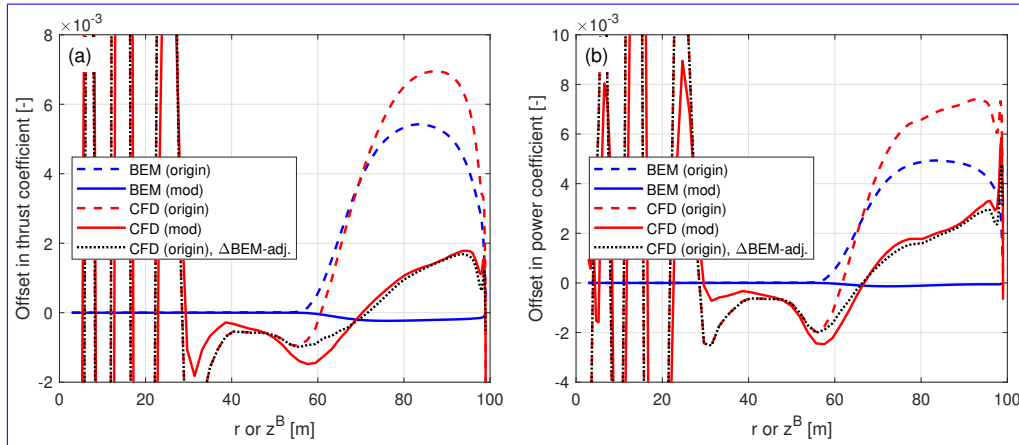


Figure 12. Offset in thrust coefficient ΔC_t (panel a) and simplified power coefficients $\Delta \tilde{C}_p$ and $\Delta \hat{C}_p$ (panel b) of the original and modified backward swept blades B-1-Uv, B-1-U20 and mB-1-Uv, mB-1-U20 compared to the baseline straight blade, for wind speeds at 12 m s^{-1} (a), (b); 15 m s^{-1} (c), (d); and wind speed of 20 m s^{-1} (e), (f).

For the modified swept blades at all tested lower loading conditions ($12, 15$ and 20 m s^{-1}), the offsets in thrust and power coefficients predicted by the BEM method are approximately zero, indicating negligible projection effects. For all tested these lower loading conditions, the CFD results of the modified swept blades show load redistribution effects clear load redistribution patterns, similar to those observed at the optimal condition. This suggests that the wake-induced effects due to blade sweep geometry maintain similar patterns across both high and low loading conditions. As wind speed increases and rotor loading decreases, the wake-induced effects diminish and gradually diminish, while the projection effects become more pronounced. This trend is particularly evident from the CFD results at higher wind speeds, at the highest wind speed (20 m s^{-1}): the load offset of the modified swept blade becomes less significant is significantly smaller compared to that of the original swept blade, especially for the local thrust coefficient.

The Thus, the CFD results of the original swept blades are insufficient to correctly draw conclusions on the wake-induced effects of swept blades for low loading conditions. The Specifically, the local thrust and power coefficients near the blade tip are overestimated due to projection effects, especially substantially overestimated at a wind speed of 20 m s^{-1} due to strong projection effects. Once again, the adjusted CFD results of the original swept blades, using BEM-based corrections in Eqs. (98) and (99), show good agreement with the CFD results of the modified swept blades at all tested lower loading conditions. This demonstrates that the projection effects of swept blades can be effectively subtracted using this adjustment method, even at lower loading conditions.

4.6.3 Rotor-integrated effects

In this section, CFD results are used to provide a clear overview of the individual and combined influences of projection and wake-induced effects on rotor-integrated thrust and simplified power coefficient. First, the wake-induced effect is calculated

from the CFD results of the modified curved blades:

$$\epsilon C_i^{\text{wake}} = (C_i^{\text{mod}} - C_i^{\text{Str}}) / C_i^{\text{Str}}, \quad (100)$$

where C_i is either the thrust coefficient (C_T) in Eq. (96) or the simplified power coefficient (\tilde{C}_P) in Eq. (97).

815 Second, the total effect (combined projection and wake-induced effects) is calculated from the CFD results of the original curved blades:

$$\epsilon C_i^{\text{tot}} = (C_i^{\text{origin}} - C_i^{\text{Str}}) / C_i^{\text{Str}}, \quad (101)$$

where C_i is either the thrust coefficient (C_T) in Eq. (90) or the simplified power coefficient (\hat{C}_P) in Eq. (91).

Finally, the projection effect is determined by subtracting the wake-induced effect from the total effect:

$$\epsilon C_T^{\text{proj}} = \epsilon C_T^{\text{tot}} - \epsilon C_T^{\text{wake}}, \quad (102)$$

$$820 \quad \epsilon C_P^{\text{proj}} = \epsilon \hat{C}_P^{\text{tot}} - \epsilon \tilde{C}_P^{\text{wake}}. \quad (103)$$

$$(104)$$

Table 4 summarizes these contributions for the backward swept blade B-1 across different operational conditions:

Table 4. Relative differences (in %) in rotor-integrated thrust and power coefficients due to projection, wake-induced and total effects for the backward swept blade B-1, as calculated from the CFD solver at different operational conditions.

Wind speed [m/s]	$\epsilon C_T^{\text{wake}}$ [%]	$\epsilon C_T^{\text{proj}}$ [%]	$\epsilon C_T^{\text{tot}}$ [%]	$\epsilon C_P^{\text{wake}}$ [%]	$\epsilon C_P^{\text{proj}}$ [%]	$\epsilon C_P^{\text{tot}}$ [%]
8.0	-0.09	0.35	0.26	2.92	0.16	3.07
12.0	-0.16	0.68	0.52	0.63	0.07	0.70
15.0	0.09	1.48	1.57	0.79	1.09	1.87
20.0	0.29	2.82	3.11	1.01	3.25	4.27

825 At the optimal operating condition, the influence of blade sweep on the rotor-integrated power is dominated by the wake-induced effect, with minimal contribution from the projection effect. However, for the rotor-integrated thrust, the projection effect is more than three times as large as the wake-induced effect. This is because the spanwise load redistribution is partially canceled out when integrating along the blade span. As wind speed increases and rotor loading decreases, the projection effect becomes increasingly dominant over the wake-induced effect, for both rotor-integrated thrust and power. For example, at a wind speed of 20 m s⁻¹, the projection effect is approximately nine times as large as the wake-induced effect for thrust and about three times as large for power.

830 4.6.4 Summary

In summary, the original swept blade setup in the previous work (Li et al., 2022d) is sufficient to show the wake-induced effects of swept blades at the optimal operational condition with high rotor loadings. However, for conditions with higher wind speeds and lower rotor thrust coefficients that were not presented in that previous work (Li et al., 2022d), the wake-induced effects decrease while projection effects become dominant. This trend is consistent for both load distributions along the blade span and also the rotor-integrated loads. Hence, the original swept blades are insufficient to correctly draw conclusions at these lower loading conditions. In comparison, the modified swept blades provide a consistent basis for comparison across all tested operational conditions. With the modified swept blades, the impact of wake geometry on the load is isolated and can be directly visualized from the CFD results. Additionally, it is demonstrated that the projection effects in the CFD results of the original swept blades can be effectively subtracted using BEM-based adjustments.

840 4.7 ~~Revisit of the prebent blade cases~~ Blades with only prebend

This section ~~revisits~~ examines blades with only sweep and no prebend, revisiting the previous study ~~on~~ presented in (Li et al., 2022d). This section examines blades with only prebend and no sweep, revisiting the previous study presented in (Li et al., 2022b). In that work, comparisons were performed using the BEM method, the lifting-line method and the CFD solver and a mid-fidelity engineering aerodynamic model developed within that study to improve prebent blade modeling. The comparisons were conducted using the original prebent blades, which have both projection and wake-induced effects included. The primary objectives were to investigate the impact of blade prebend on wake geometry and the resulting effects on loads and to demonstrate the improved agreement between the ~~CFD solver~~ higher-fidelity LL and CFD solvers and the newly developed model compared to the BEM method in predicting the prebend effects. In the present work, results from both the original and the modified prebent blades are used for the comparison.

850 4.7.1 Optimal operation condition

The optimal operational condition with a uniform inflow velocity of 8 m s^{-1} is first used for comparison. The load offsets of the original and modified prebent blades compared to the baseline straight blade are calculated using Eqs. (94) and (95) and are plotted against the radius. Since B-sys coincides with BL-sys for blades without sweep, the thrust coefficients $C_t(r)$ and $C_t(z^B)$ in Eqs. (88) and (94), and the simplified power coefficients $\tilde{C}_p(r)$ and $\hat{C}_p(z^B)$ in Eqs. (89) and (95) are identical. Results of the original and modified upwind prebent blades (W-1 and mW-1) are shown in Fig. 13. Results of the downwind prebent blades (W-5 and mW-5) are shown in Fig. 14. In addition, the adjusted CFD results of the original prebent blades, obtained by subtracting the projection effects predicted by the BEM method using Eqs. (98) and (99), are also included for comparison.

For the original upwind prebent blade W-1, the BEM method predicts a decrease in the thrust coefficient in the prebent region of the blade due to projection effects, with a maximum offset magnitude of approximately 0.017 at a radius of 88 m. This offset is slightly larger than that observed for the original backward swept blade B-1 (value of approximately 0.01), which has the

860

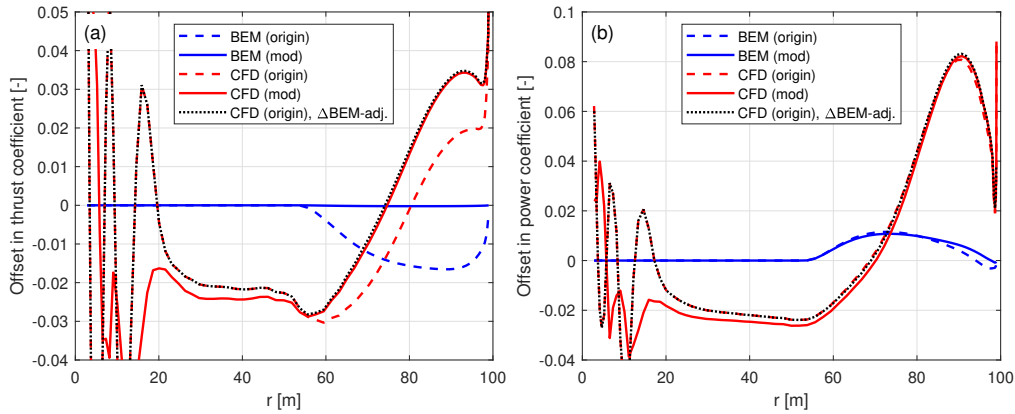


Figure 13. Offset in thrust coefficient ΔC_t (panel a) and simplified power coefficient $\Delta \tilde{C}_p$ (panel b) of the original upwind prebent blade W-1 and the modified upwind prebent blade mW-1, compared to the baseline straight blade, at a wind speed of 8 m s^{-1} .

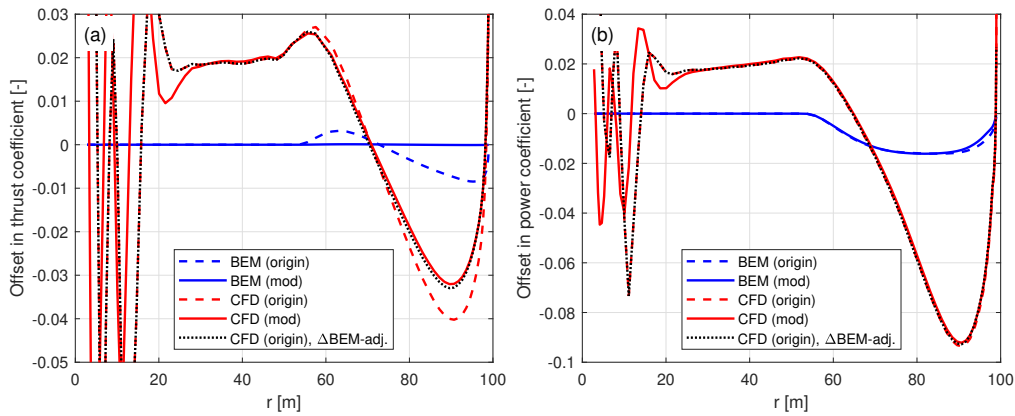


Figure 14. Offset in thrust coefficient ΔC_t (panel a) and simplified power coefficient $\Delta \tilde{C}_p$ (panel b) of the original downwind prebent blade W-5 and the modified downwind prebent blade mW-5, compared to the baseline straight blade, at a wind speed of 8 m s^{-1} .

865 same curved main axis shape. For the original downwind prebent blade W-5, the BEM method predicts a smaller decrease in the thrust coefficient, which is also due to the projection effects, with a maximum offset magnitude of approximately 0.01 at a radius of 95 m. These findings suggest that projection effects remain relatively small for the original prebent blades, indicating that they operate under conditions similar to the baseline straight blade. For the modified prebent blades mW-1 and mW-5, the thrust coefficient offsets predicted by the BEM method are approximately zero throughout the span, confirming that projection effects are effectively subtracted. This outcome validates the modifications to the chord and twist distributions derived in Sect. 2.8 as well as the approximations in Sect. 2.8.2. The BEM method predicts very similar results for the simplified power coefficient for both the original and modified prebent blades. A slight increase in power is predicted for the upwind prebent

870 blades (W-1 and mW-1) and a slight decrease for the downwind prebent blades (W-5 and mW-5). These differences arise because the main axis used in the comparison is the half-chord line rather than the 1/4 chord line, as discussed in Sect. 2.8.2.

The CFD results include the aerodynamic effects of changed wake geometries due to blade prebend, as indicated by the load offsets between the modified prebent blades and the baseline straight blade. The load offsets predicted by the CFD solver show a spanwise redistribution pattern, consistent with previous observations (Li et al., 2022b). For the modified upwind prebent blade mW-1, the loads are initially lower than those of the baseline straight blade in the inboard part of the blade, where the main axis is still straight (radius less than 50 m). When moving from the spanwise location where the blade starts to dihedral towards halfway to the blade tip (radius of 75 m), loads gradually increase but remain lower compared to the baseline. Moving further towards the tip, loads increase further and become higher compared to the baseline. For the modified downwind prebent blade mW-5, an opposite load redistribution pattern is observed.

880 For prebent blades, the projection effects arise only in the outboard region, which is consistent with the blade geometry setup where prebend begins around mid-span. Notably, load redistribution patterns differ ~~between prebent and from those seen in~~ swept blades. For prebent blades, the blade dihedral at the outboard part of the blade influences the entire blade span. In contrast, as shown in Sect. 4.6, blade sweep ~~primarily affects~~ effect is largely restricted to the swept portion of the blade with minimal impact on the inboard part of the blade that remains straight. This distinction implies that blade sweep and prebend 885 have different mechanisms affecting the wake geometries and consequently the loads. As a result, different engineering wake modeling techniques are necessary to correctly model these two effects.

The performance of using CFD results of the original prebent blades (W-1 and W-5) to investigate the impact of the wake geometry of the blade prebend, as has been done in the previous work (Li et al., 2022b), is also analyzed. As shown in Figs. 13 and 14, the power coefficient offsets are almost identical for the original and modified setups. However, the thrust coefficient 890 offsets of the original prebent blades are slightly decreased due to the projection effects. Since the differences between the CFD results of the original and modified prebent blades are minimal, the projection effect is thus of little significance compared to the wake-induced effect. As a result, it is still sufficient to correctly draw conclusions using the original prebent blades, despite small projection errors.

The adjusted CFD results of the original prebent blades, using BEM-based corrections according to Eqs. (98) and (99), 895 labeled as "CFD(origin), Δ BEM-adj." in the figure, show very good agreement with the CFD results of the modified prebent blades. This indicates that projection effects in the CFD and BEM results are similar for prebent blades and can be effectively subtracted using this adjustment. Moreover, as with swept blades in Sect. 4.6, this suggests that the cross-flow principle used in the BEM method performs well also for prebent blades.

4.7.2 Lower loading conditions

900 Comparisons are also performed for the upwind prebent blades ~~W-1-Uv and mW-1-Uv~~, at operational conditions corresponding to lower thrust coefficients listed in Table 1. The offsets in thrust and simplified power coefficients ~~are for the upwind prebent blades W-1-Uv and mW-1-Uv at a wind speed 20 m s⁻¹ (lowest loading condition) are presented in Fig. 15, while results at~~

intermediate conditions (12 and 15 m s⁻¹) are shown in Fig. D3 in Appendix D3¹². Similar conclusions apply to the downwind prebent blades W-5-Uv and mW-5-Uv, which are then not shown in this study.

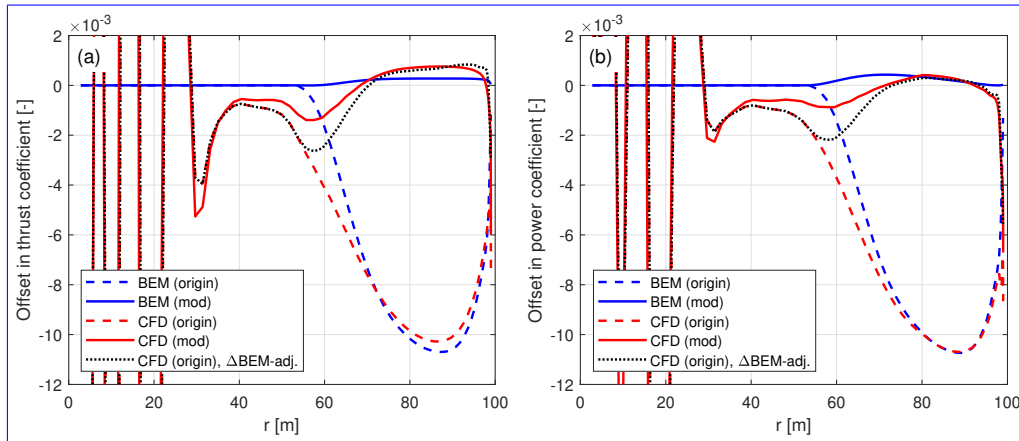


Figure 15. Offset in thrust coefficient ΔC_t (panel a) and simplified power coefficient $\Delta \tilde{C}_p$ (panel b) of the original and modified upwind prebent blades W-1-Uv, W-1-U20 and mW-1-Uv, mW-1-U20 compared to the baseline straight blade, for wind speeds at 12 m s⁻¹ (a), (b); 15 m s⁻¹ (c), (d); and wind speed of 20 m s⁻¹ (e), (f).

905 For the modified prebent blades at all tested lower loading conditions (12, 15 and 20 m s⁻¹), the thrust coefficient offsets predicted by the BEM method are approximately zero, indicating the projection effects are effectively removed. The power coefficient offsets have small values, primarily due to the torsion rate drag force, as discussed earlier. The CFD results of the modified prebent blades can directly show the impact of wake geometry due to blade prebend on the loads. Similar to the high-loading case, a spanwise load redistribution pattern can be observed for all ease tested lower loading conditions. This means the wake-induced effects due to blade prebend maintain similar patterns across both high and low loading conditions.

915 The projection effect can be characterized by the load difference between the original and modified prebent blades, for both BEM and CFD results. Comparing the CFD results of the original and modified prebent blades, it is visualized that as the wind speed increases (from 12 to 20 m s⁻¹), the load offset of the modified prebent blade becomes less significant compared to the original prebent blade. This trend indicates that as rotor loading decreases, the wake-induced effects diminish and the projection effects become dominant.

920 Due to the dominating projection effects at all tested lower loading conditions, the spanwise load redistribution pattern is not observed in the CFD results of the original prebent blades. Instead, both the BEM method and the CFD solver predict that the loads of the original prebent blades are consistently lower compared to the baseline throughout the span for all tested lower loading conditions. The projection effects in the original prebent blades are more pronounced compared to than those observed in the original swept blades discussed previously in Sect. 4.6.2. Nevertheless, the original prebent blades still operate under

¹²For completeness and ease of comparison, Fig. D3 also includes results at 20 m s⁻¹.

conditions close to those of the baseline straight blade, with maximum thrust coefficient differences due to projection effects being remaining relatively small (approximately 0.015).

The CFD results of the original prebent blade, after the adjustment of subtracting the projection effects based on the BEM results using Eqs. (98) and (99), show very good agreement with the CFD results of the modified prebent blades at all tested
 925 lower loading conditions. This demonstrates that the projection effects in the CFD results of the original prebent blades can be effectively subtracted using this BEM-based adjustment, even at these lower loading conditions.

4.7.3 Rotor-integrated effects

Similar to Sect. 4.6.3, this section uses CFD results to compare the individual contributions of projection and wake-induced effects to rotor-integrated loads. The contributions of projection and wake-induced effects on the rotor-integrated thrust and
 930 power coefficients for the upwind prebent blade W-1 across different operational conditions, as determined using the CFD results, are summarized in Table 5. Note that when performing the integration, load offsets relative to the baseline straight blade in the blade root region (radius less than 30 m) are excluded to avoid errors caused by noisy results in this region.

Table 5. Relative differences (in %) in rotor-integrated thrust and power coefficients due to projection, wake-induced and total effects for the upwind prebent blade W-1, as calculated from the CFD solver at different operational conditions.

<u>Wind speed [m/s]</u>	<u>$\epsilon C_T^{\text{wake}}$ [%]</u>	<u>$\epsilon C_T^{\text{proj}}$ [%]</u>	<u>$\epsilon C_T^{\text{tot}}$ [%]</u>	<u>$\epsilon C_P^{\text{wake}}$ [%]</u>	<u>$\epsilon C_P^{\text{proj}}$ [%]</u>	<u>$\epsilon C_P^{\text{tot}}$ [%]</u>
<u>8.0</u>	<u>0.13</u>	<u>-0.86</u>	<u>-0.72</u>	<u>3.94</u>	<u>0.25</u>	<u>4.18</u>
<u>12.0</u>	<u>-0.37</u>	<u>-1.94</u>	<u>-2.31</u>	<u>0.11</u>	<u>-1.87</u>	<u>-1.76</u>
<u>15.0</u>	<u>-0.21</u>	<u>-3.48</u>	<u>-3.68</u>	<u>-0.26</u>	<u>-3.87</u>	<u>-4.08</u>
<u>20.0</u>	<u>-0.05</u>	<u>-6.10</u>	<u>-6.15</u>	<u>-0.35</u>	<u>-7.55</u>	<u>-7.91</u>

At the optimal operating condition, the influence of blade prebend on the rotor-integrated power is dominated by the wake-induced effect, with a small positive contribution from projection. In contrast, for the rotor-integrated thrust, the projection
 935 effect is more than six times as large as the wake-induced effect. As described earlier for swept blades in Sect. 4.6.3, this is due to the spanwise load redistribution being partially canceled out when integrated along the blade span. As wind speed increases and rotor loading decreases, the projection effect rapidly becomes dominant over the wake-induced effect, for both rotor-integrated thrust and power. Compared to the swept blade case, the projection effect is more pronounced in the prebent case under the same operating conditions. For example, at a wind speed of 20 m s⁻¹, the projection effect on rotor thrust is
 940 approximately 10 times as large as the wake-induced effect and for rotor power, it is more than 20 times as large.

4.7.4 **Summary**

In summary, while the original prebent blade setup in the previous study (Li et al., 2022b) is sufficient to correctly show the wake-induced effects at the optimal operational condition, it becomes insufficient at lower loading conditions where projection effects dominate. In contrast, the modified prebent blades provide a consistent basis for comparison across all tested operational

945 conditions, enabling the wake-induced effects to be highlighted and directly visualized from the CFD results. Additionally, the projection effects in the CFD results of the original prebent blades can be effectively subtracted using BEM-based adjustments.

4.8 Blades with sweep and prebend combined

In this section, generalized curved blades with both sweep and prebend combined are investigated. The primary objective is to demonstrate that the modified curved blades are necessary to correctly show the wake-induced effects on loads and thus
 950 are necessary for a consistent aerodynamic comparison. The results in this section provide insights for future aerodynamic comparisons involving such generalized curved blade configurations.

4.8.1 Optimal operational condition

First, comparisons are performed at the optimal operational condition with a uniform inflow velocity of 8 m s^{-1} . The load offsets of both the original and modified curved blades, compared to the baseline straight blade, are calculated. For the original
 955 curved blades, the load offsets ΔC_t and $\Delta \hat{C}_p$ are computed using Eqs. (88) and (89) and plotted against the z^B -coordinates. For the modified curved blades, the load offsets ΔC_t and $\Delta \tilde{C}_p$ are calculated using Eqs. (94) and (95) and plotted against the radius. Results for the curved blades based on C-11 (backward sweep and upwind prebend) and C-55 (forward sweep and downwind prebend) are depicted in Figs. 16 and 17, respectively. Results for the curved blades based on C-15 (backward sweep and downwind prebend) and C-51 (forward sweep and upwind prebend) are shown in Figs. 18 and 19. In addition, the adjusted
 960 CFD results of the original curved blades, obtained by subtracting the projection effects predicted by the BEM method using Eqs. (98) and (99), are included for comparison.

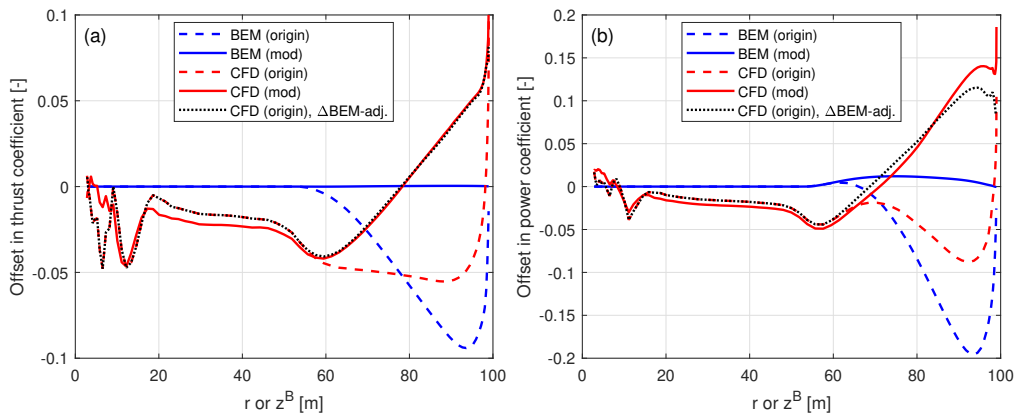


Figure 16. Offset in thrust coefficient ΔC_t (panel a) and simplified power coefficients $\Delta \tilde{C}_p$ and $\Delta \hat{C}_p$ (panel b) of the original and modified curved blades C-11 and mC-11, both with backward sweep and upwind prebend combined, compared to the baseline straight blade, at a wind speed of 8 m s^{-1} .

For the original curved blades, the load offsets predicted by the BEM method are primarily due to projection effects. The thrust coefficient offsets are significantly larger compared to those observed for blades with only sweep or only prebend.

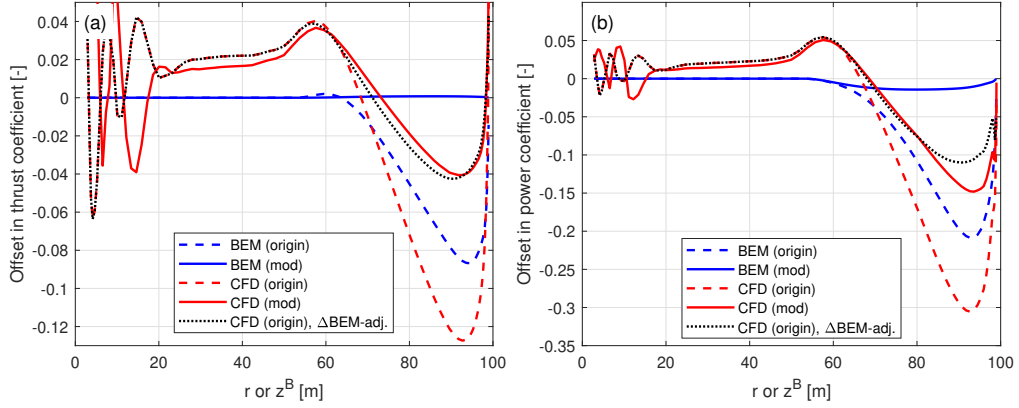


Figure 17. Offset in thrust coefficient ΔC_t (panel a) and simplified power coefficients $\Delta \tilde{C}_p$ and $\Delta \hat{C}_p$ (panel b) of the original and modified curved blades C-55 and mC-55, both with forward sweep and downwind prebend combined, compared to the baseline straight blade, at a wind speed of 8 m s^{-1} .

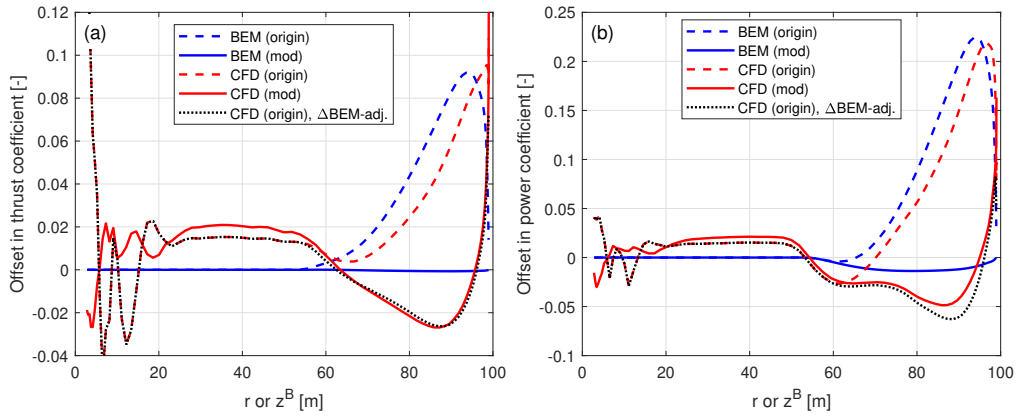


Figure 18. Offset in thrust coefficient ΔC_t (panel a) and simplified power coefficients $\Delta \tilde{C}_p$ and $\Delta \hat{C}_p$ (panel b) of the original and modified curved blades C-15 and mC-15, both with backward sweep and downwind prebend combined, compared to the baseline straight blade, at a wind speed of 8 m s^{-1} .

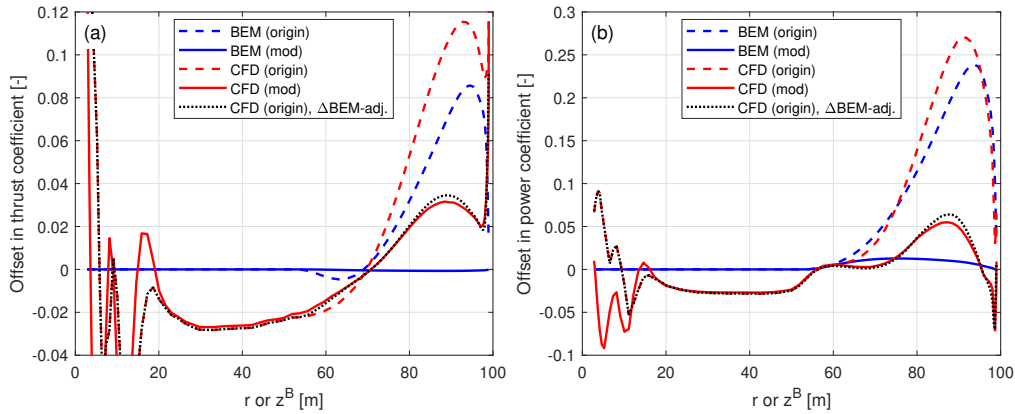


Figure 19. Offset in thrust coefficient ΔC_t^c (panel a) and simplified power coefficients $\Delta \tilde{C}_p$ and $\Delta \hat{C}_p$ (panel b) of the original and modified curved blades C-51 and mC-51, both with forward sweep and upwind prebend combined, compared to the baseline straight blade, at a wind speed of 8 m s^{-1} .

Specifically, for original curved blades C-11 and C-55, the maximum thrust coefficient decrease is around 0.09 at the z^B -
 965 coordinate of 94 m, while for C-15 and C-51, a maximum increase of approximately 0.09 is reached at the same spanwise
 location. Compared to the original swept blades B-1 and B-5, and the original prebend blades W-1 and W-5, the thrust coefficient
 offsets are approximately 5 to 10 times larger. Regarding the simplified power coefficient, the BEM method predicts even larger
 offsets for these original curved blades. For C-11 and C-55, a maximum decrease of approximately 0.2 is observed at the z^B -
 970 coordinate of 94 m, while for C-15 and C-51, a maximum increase of approximately 0.23 is reached at the same spanwise
 location. These considerable offsets indicate that the original curved blades with both sweep and prebend combined operate
 under different conditions compared to the baseline straight blade, primarily due to significant projection effects. This contrasts
 with the blades with only sweep or only prebend in Sects. 4.6 and 4.7, where projection effects were relatively small.

Conversely, for the modified curved blades, the thrust coefficient offsets predicted by the BEM method are approximately
 zero across the span, indicating that projection effects have been effectively subtracted. This validates the modifications to
 975 the chord and twist distributions derived in Sect. 2.8 as well as the approximations in Sect. 2.8.2. In terms of the simplified
 power coefficient, the BEM method predicts slight increases for the modified curved blades with upwind prebend components
 (mC-11 and mC-51) and slight decreases for those with downwind prebend components (mC-55 and mC-15). These variations
 are mostly due to the torsion rate drag in Eq. (78), originating from the main axis being the half-chord line instead of the 1/4
 chord line, as also observed for the blades with only prebend in Sect. 4.7.

980 The CFD solver accurately models captures the effect of changed wake geometries on the aerodynamics, which is quantified
 by the load offsets between the modified curved blades and the baseline straight blade. A spanwise load redistribution pattern is
also clearly observed from the CFD results of the modified curved blades with both sweep and prebend combined, similar to the
 cases of blades with only sweep in Sect. 4.6 and with only prebend in Sect. 4.7. This redistribution arises from the combination
 of sweep and prebend applied in the outboard portion of the blade. However, the superposed geometrical changes lead to more

985 complex aerodynamic behavior, with both sweep effects (local effects) and prebend effects (global effects) combined. For mC-11 and mC-51, the loads initially decrease and then increase compared to the baseline straight blade, when moving from the blade root towards the blade tip. For mC-55 and mC-15, the opposite pattern is observed, ~~where:~~ the loads initially increase and then decrease ~~compared to the baseline straight blade,~~ when moving from the blade root ~~to~~ toward the blade tip.

The performance of using the CFD results of the original curved blades (C-bw) to investigate the wake-induced effects for 990 blades with both sweep and prebend combined is also analyzed. Due to strong projection effects, the load offsets of C-11 and C-55 are substantially underestimated, while the load offsets of C-15 and C-51 are significantly overestimated. Consequently, the spanwise load redistribution effect is not evident from the CFD results of the original curved blades. For example, the loads of the original curved blade C-11 are consistently lower compared to the baseline straight blade, except at the very blade tip. For the original curved blade C-55, load redistribution patterns can still be visualized, but the load offsets at the z -coordinate 995 of 90 m are overestimated by a factor of two.

Moreover, the CFD results of the original curved blades adjusted using the BEM results according to Eqs. (98) and (99), labeled as "CFD(origin), Δ BEM-adj." in the figure, show satisfactory agreement with the CFD results of the modified curved blades. This indicates that the projection effects in the CFD and BEM results of the original curved blades are similar, which can be effectively subtracted using this BEM-based adjustment. This also suggests that the cross-flow principle used in the 1000 BEM method performs well for generalized curved blades. Additionally, this suggests that BEM and CFD can be integrated into a multi-fidelity optimization framework. In such a framework, BEM could be used for small variations of chord and twist while CFD would be needed for changes to the main axis geometry.

4.8.2 Lower loading conditions

Further comparisons are made for the original and modified curved blades ~~C-bw-Uv and mC-bw-Uv~~ combining sweep and 1005 prebend, at lower loading conditions, as listed in Table 1. Results for the blades C-11-Uv and mC-11-Uv, which are based on C-11 (with backward sweep and upwind prebend) operating at a wind speed of 20 m/s, are shown in Fig. ~~D4. Results for the other curved blades based on C-55~~ 20. Additional results for the curved blades C-bw-Uv and mC-bw-Uv (covering blade geometries C-11, C-15 and, C-51 and C-55) at lower loading conditions are provided in Appendix D4.

For the modified curved blades at all tested lower loading conditions, the BEM method predicts approximately zero thrust 1010 coefficient offsets throughout the span, confirming that the projection effect is sufficiently subtracted. For the power coefficient, the small non-zero offset is due to the torsion rate drag force, as previously discussed. The CFD results of the modified curved blades directly show the impact of wake geometry on loads. ~~For all~~ Across all tested lower loading conditions ~~, a~~ (12, 15 and 20 m s⁻¹), a consistent spanwise load redistribution pattern can be observed, similar to that at the optimal condition with high loadings. This indicates the wake-induced effects, which are due to blade curved geometry, have similar patterns across 1015 different loading conditions.

In contrast, the CFD results of the original curved blades do not show this pattern. Both BEM and CFD results show that the loads of the original curved blades C-11-Uv and C-55-Uv are lower compared to the baseline throughout the span, while the loads of C-15-Uv and C-51-Uv are higher. The load difference between the original and modified curved blades represents

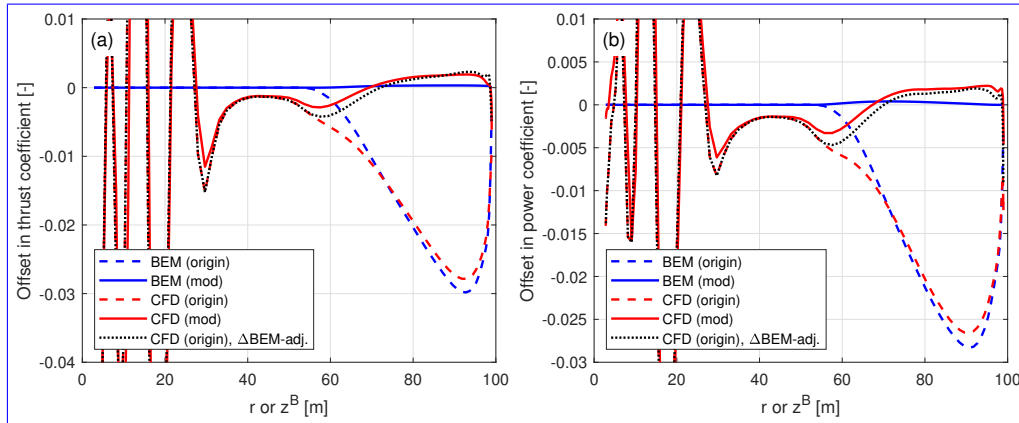


Figure 20. Offset in thrust coefficient ΔC_t (panel a) and simplified power coefficients $\Delta \tilde{C}_p$ and $\Delta \hat{C}_p$ (panel b) of the original and modified curved blades C-11-Uv C-11-U20 and mC-11-Uv mC-11-U20 with backward sweep and upwind prebend combined, compared to the baseline straight blade: ; at 12 m s^{-1} (a), (b); 15 m s^{-1} (c), (d); and wind speed of 20 m s^{-1} (e), (f).

the projection effects for both BEM and CFD results. Projection effects are already strong at 12 m s^{-1} , compared to the wake-induced effect. As wind speed increases and rotor loading decreases, the wake-induced effects diminish and the projection effects further dominate.

The CFD results of the original curved blades, after subtracting the BEM-predicted projection effects using Eqs. (98) and (99), show satisfactory agreement with the CFD results of the modified curved blades. This demonstrates that the projection effects in the original curved blades, despite their complex combined sweep and prebend geometries, can be effectively subtracted using this adjustment, even at at all tested lower loading conditions.

4.8.3 Rotor-integrated effects

Similar to Sects. 4.6.3 and 4.7.3, this section uses CFD results to compare the individual contributions of projection and wake-induced effects to rotor-integrated loads. The contributions of projection and wake-induced effects on the rotor-integrated thrust and power coefficients, for the curved blade C-11, which features both backward sweep and upwind prebend, across different operational conditions, are shown in Table 6.

At all operational conditions, the projection effect is clearly dominant over the wake-induced effect. Moreover, for the combined curved blade, the magnitude of the projection effect is substantially larger than in the cases with only sweep or only prebend. As wind speed increases and rotor loading decreases, the dominance of the projection effect becomes even more pronounced. This trend is consistent with the observations for blades with only sweep or prebend.

Table 6. Relative differences (in %) in rotor-integrated thrust and power coefficients due to projection, wake-induced and total effects for the curved blade C-11 (with backward sweep and upwind prebend combined), calculated from CFD at different operational conditions.

Wind speed [m/s]	$\epsilon C_T^{\text{wake}}$ [%]	$\epsilon C_T^{\text{proj}}$ [%]	$\epsilon C_T^{\text{tot}}$ [%]	$\epsilon C_P^{\text{wake}}$ [%]	$\epsilon C_P^{\text{proj}}$ [%]	$\epsilon C_P^{\text{tot}}$ [%]
8.0	-0.13	-3.90	-4.03	6.34	-14.68	-8.34
12.0	-0.68	-5.64	-6.32	0.47	-10.83	-10.37
15.0	-0.31	-8.62	-8.93	0.25	-12.22	-11.97
20.0	0.01	-13.42	-13.41	0.28	-16.45	-16.18

1035 4.8.4 Summary

In summary, for the tested curved blades combining both sweep and prebend, using the original setup with the same chord and twist distributions as the baseline straight blade is inadequate for investigating the wake-induced effects on loads. The projection effect is significant and dominates the wake-induced effect, leading to misinterpretations of the aerodynamic behavior. In contrast, the curved blades with modified chord and twist distributions enable consistent comparisons across all tested operational conditions. The impact of wake geometry on the load is isolated and can be directly visualized from the CFD results, showing a spanwise load redistribution pattern. Furthermore, it is demonstrated that for the CFD results of the original setup, the projection effects can be effectively subtracted using BEM-based adjustments.

4.9 Feasibility of superimposing separately modeled sweep and prebend

This section examines whether the wake-induced effects of curved blades with both sweep and prebend combined can be effectively taken into account by modeling the sweep and prebend effects separately and then superimposing them. This approach is tested by comparing the load offsets of a blade with combined sweep and prebend to the summed load offsets of two corresponding blades: one with only sweep and one with only prebend. The main axes of these two projected blades are derived directly from the geometry of the combined curved blade.

For a modified curved blade mC-bw, there are two corresponding projected blades mB-b and mW-w, with either only sweep or only prebend. The main axis geometry of the swept blade mB-b is obtained by removing the prebend component (y^B) from the main axis of mC-bw. Similarly, the main axis geometry of the prebent blade mW-w is obtained by removing the sweep component (x^B) from the main axis of mC-bw. The main axis of mW-w is further scaled so that each blade section has the same radius as in mC-bw. The chord and twist distributions of mB-b and mW-w are modified according to Sect. 2.8 to ensure that the BEM method predicts the same circulation distribution and inductions as the combined curved blade. For example, for the modified curved blade mC-15 with backward sweep and downwind prebend combined, the corresponding projected blades are the modified backward swept blade mB-1 and the modified downwind prebent blade mW-5.

4.9.1 Optimal operational condition

First, comparisons are performed at the optimal operational condition with a uniform inflow velocity of 8 m s^{-1} . For each modified curved blade mC-bw, load offsets are compared with those of the corresponding modified swept blade mB-b, the modified prebend blade mW-w and the superposition of both offsets (i.e., the sum of the load offsets from mB-b and mW-w). The results for the modified curved blades mC-11, mC-55, mC-15 and mC-51 are shown in Figs. 21 to 24.

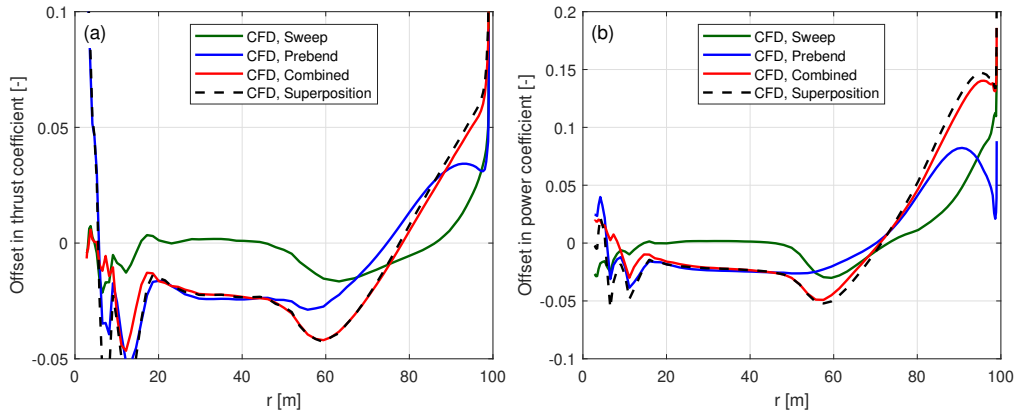


Figure 21. Offset in thrust coefficient ΔC_t (panel a) and simplified power coefficient $\Delta \tilde{C}_p$ (panel b) between the modified backward swept blade mB-1, the modified upwind prebend blade mW-1, the modified curved blade mC-11 with both backward sweep and upwind prebend combined and the superposition of the sweep and prebend offsets, compared to the baseline straight blade, at a wind speed of 8 m s^{-1} .

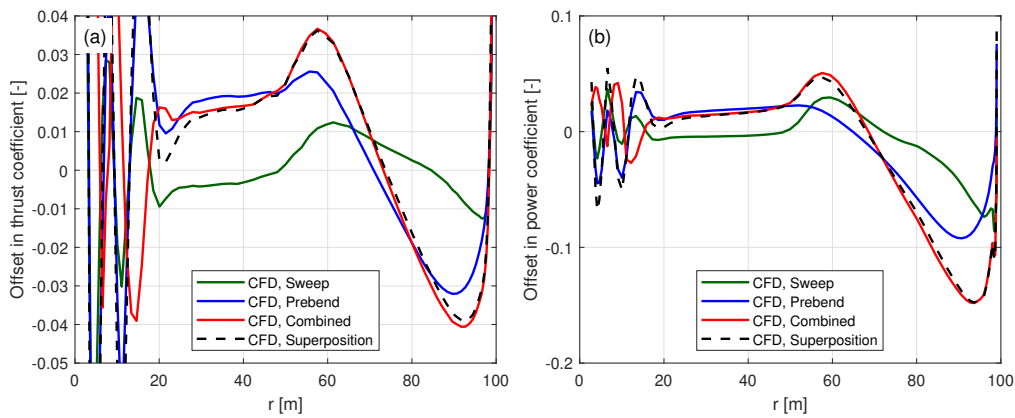


Figure 22. Offset in thrust coefficient ΔC_t (panel a) and simplified power coefficient $\Delta \tilde{C}_p$ (panel b) between the modified forward swept blade mB-5, the modified downwind prebend blade mW-5, the modified curved blade mC-55 with both forward sweep and downwind prebend combined and the superposition of the sweep and prebend offsets, compared to the baseline straight blade, at a wind speed of 8 m s^{-1} .

For all tested modified curved blades, the load offsets are well approximated using the superposition of the load offsets of the two corresponding modified swept and prebend blades. For mC-11 and mC-55, the spanwise load redistribution effects of

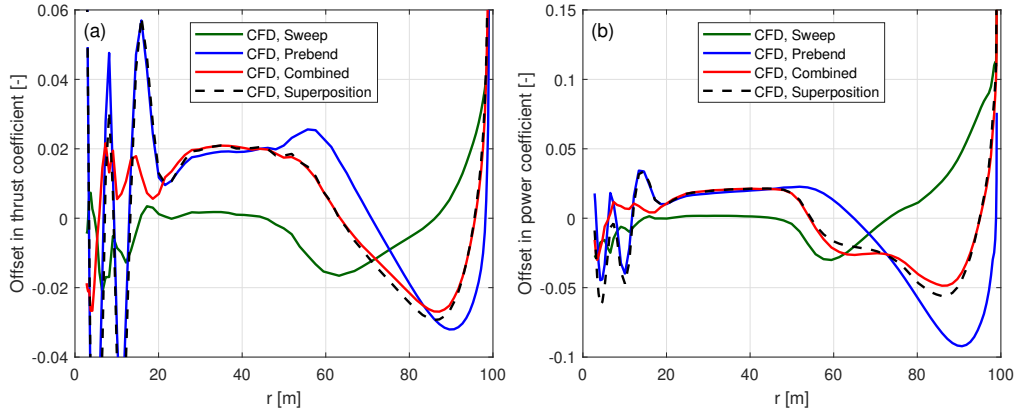


Figure 23. Offset in thrust coefficient ΔC_t (panel a) and simplified power coefficient $\Delta \tilde{C}_p$ (panel b) between the modified backward swept blade mB-1, the modified downwind prebend blade mW-5, the modified curved blade mC-15 with both backward sweep and downwind prebend combined and the superposition of the sweep and prebend offsets, compared to the baseline straight blade, at a wind speed of 8 m s^{-1} .

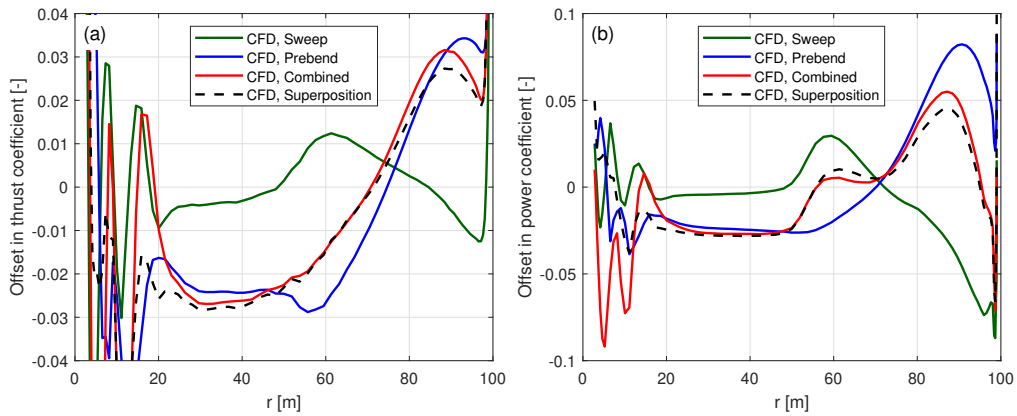


Figure 24. Offset in thrust coefficient ΔC_t (panel a) and simplified power coefficient $\Delta \tilde{C}_p$ (panel b) between the modified forward swept blade mB-5, the modified upwind prebend blade mW-1, the modified curved blade mC-51 with both forward sweep and upwind prebend combined and the superposition of the sweep and prebend offsets, compared to the baseline straight blade, at a wind speed of 8 m s^{-1} .

the corresponding swept and prebent blades are in the same direction. After the superposition, the load redistribution effect of the combined curved blade becomes more significant. For mC-15 and mC-51, the spanwise load redistribution effects of the corresponding swept and prebent blades are in opposite directions. After the superposition, the load redistribution effects partially cancel out, resulting in less significant effects.

4.9.2 Lower loading conditions

Further comparisons are performed for the modified curved blades mC-bw-Uv at lower loading conditions, as listed in Table 1. Results for mC-11-Uv are shown in Fig. 25. Results for the other curved blades based on mC-55, mC-15 and mC-51 are provided in Appendix D5.

For all four cases, the load offsets estimated using the superposition of the CFD results of the two corresponding projected blades show satisfactory agreement with the load offsets of the modified combined curved blades. As wind speed increases and rotor loading decreases, the agreement slightly worsens for the blade tip region (radius greater than 75 m), suggesting that the superposition assumption is less valid. However, since the wake-induced effect decreases as rotor loading decreases, the absolute error of the prediction using the superposition remains small. Overall, the general trends of the load offsets are well captured using this superposition approach.

4.9.3 Summary

In summary, the findings demonstrate that for general curved blades combining both sweep and prebend, the wake-induced effects can be effectively approximated by modeling the sweep and prebend effects separately and then linearly superimposing the results. This approach is confirmed using CFD results, showing promising agreement for different curved blade configurations across various operational conditions. These results provide valuable insights and guidelines for the future development of engineering aerodynamic models for generalized curved blades. For example, they suggest the possibility of directly superimposing the inductions from the coupled near and far wake model (Li et al., 2022d), which models only the blade sweep effect with those from the vortex cylinder model (Li et al., 2022b), which models only the blade prebend effect, to model a generalized curved blade.

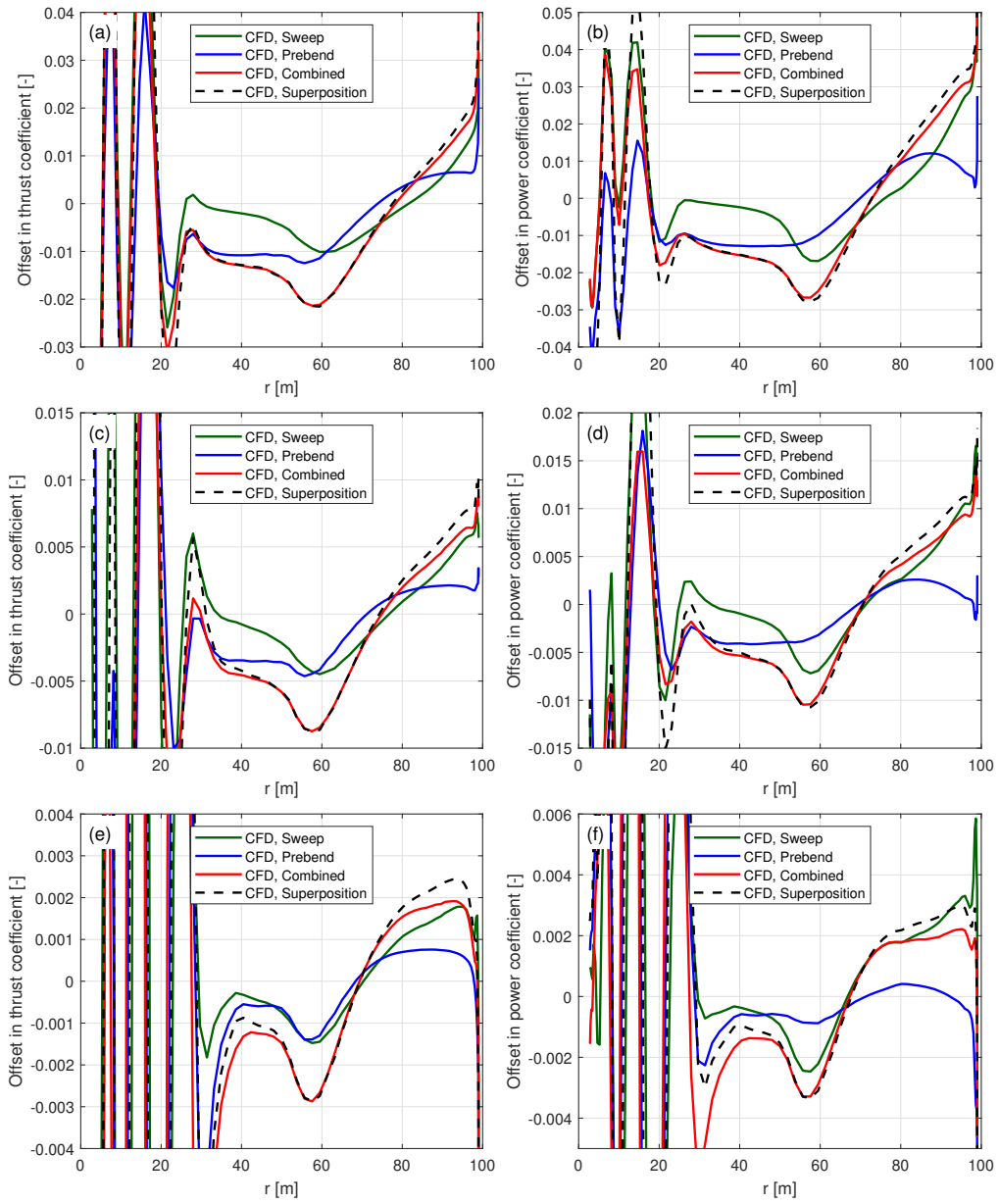


Figure 25. Offset in thrust coefficient ΔC_t and simplified power coefficient $\Delta \tilde{C}_p$ of the modified backward swept blades mB-1-Uv, the modified upwind prebend blades mW-1-Uv, the modified curved blade mC-11-Uv with both backward sweep and upwind prebend combined and the superposition of the sweep and prebend offsets, compared to the baseline straight blade: at 12 m s^{-1} (a), (b); 15 m s^{-1} (c), (d); and 20 m s^{-1} (e), (f).

5 Conclusions and future work

This study establishes a framework for consistent aerodynamic comparisons of blades with different curved geometries, effectively isolating wake-induced effects from projection effects arising from velocity and load projections. This framework
1090 employs modified curved blades, with chord and twist distributions adjusted based on the blade's curved geometry, ensuring they operate under the same angles of attack and local thrust coefficients as the baseline straight blade, as predicted by the blade element momentum (BEM) method. Revisiting previous comparisons for blades with either sweep or prebend shows that, under optimal operational conditions with high rotor loadings, the original setup with the same chord and twist distributions is sufficient to show the wake-induced effects. However, under lower loading conditions, projection effects becomes dominant over wake geometry effects, leading to inconsistent comparisons. For blades with both sweep and prebend combined,
1095 the original setup consistently exhibits significant projection effects across all operational conditions, making it insufficient for consistent comparisons. Using the modified curved blades, more consistent comparisons are achieved. Results from the Reynolds-averaged Navier–Stokes (RANS) CFD solver with the 3-D rotor geometry fully resolved show spanwise load redistribution patterns, similar to those observed in blades with only sweep or only prebend. Additionally, it is shown that projection
1100 effects in the CFD results can be effectively subtracted using BEM-based adjustments, confirming the validity of the modified blade setup for more consistent comparisons.

Another key finding of this study is that for blades combining both sweep and prebend, the wake-induced effects can be accurately approximated by linearly superimposing the wake-induced effects from the two corresponding blades, with only sweep and only prebend. This finding supports the approach of modeling sweep and prebend effects on inductions separately
1105 and then combining them, offering valuable guidance for the development of future mid-fidelity engineering aerodynamic models for general curved blade geometries.

While this work has focused on steady-state aerodynamic comparisons of rigid blades, the aeroelastic response of curved blades remains an important direction for future research. In particular, the dynamic aerodynamic response of curved blades may differ significantly from that of straight blades. Moreover, the observed load redistribution, through loading or deloading near the tip region, is expected to change both the steady and dynamic aeroelastic load alleviation associated with blade sweep.
1110

Appendix A: Nomenclature

Table A1. Variables Roman-letter variables used in the present work.

Symbol	Description
a, a_B	axial induction factor; axial induction factor at the blade
a'	tangential induction factor
\mathbf{a}	centrifugal acceleration vector
c	chord length
C_L, C_D, C_M	2-D lift, drag and sectional moment coefficients
C_t	local thrust coefficient
\tilde{C}_T	<u>rotor-integrated thrust coefficient</u>
\tilde{C}_p, \hat{C}_p	simplified local power coefficient from: the tangential force; the in-plane force
$\tilde{\tilde{C}}_p, \hat{\tilde{C}}_p$	<u>rotor-integrated simplified power coefficient from: the tangential force; the in-plane force</u>
F	Prandtl's tip-loss factor
k_s	normalized bound circulation of all blades
N_B	number of blades
r	radius of a blade section
\tilde{r}_c	<u>blade curve ratio</u>
R_{tot}	radius of the rotor
$\mathbf{R}_x, \mathbf{R}_y, \mathbf{R}_z$	rotation matrix around x -axis, y -axis and z -axis
s	curved blade length
\mathbf{t}, \mathbf{t}^*	tangent vector; modified tangent vector
\mathbf{T}	transformation matrix
T_0	time constant in unsteady 2-D aerodynamic model
U_0	free wind speed
V	3-D relative velocity magnitude
V_{rel}	2-D relative velocity magnitude

Table A2. Variables in Greek letters used in the present work.

Symbol	Description
α	angle of attack
β, β^*	twist angle, positive value with (positive for airfoil nose down); <u>in the sectional / modified sectional coordinate</u>
Γ	<u>bound vorticity of a blade section</u>
δ	position angle
$\Delta\alpha$	<u>difference in angle of attack: 3/4 chord point minus 1/4 chord point</u>
$\Delta\alpha_{1/4}$	<u>difference in angle of attack: calculation point minus 1/4 chord point</u>
$\Delta\alpha_{3/4}$	<u>difference in angle of attack: 3/4 chord point minus calculation point</u>
Δd	<u>blade curve magnitude</u>
$\Delta\theta_z$	rotational angle between the sectional and modified sectional coordinate systems
Γ bound vorticity of a blade section $\ddot{\epsilon}$	mid-chord heaving acceleration of the 2-D airfoil
ζ	<u>ratio of tangents: 2-D sectional flow angle ϕ to inflow angle φ</u>
θ_p	pitch angle; additional twist angle offset
$\dot{\theta}$	airfoil torsion rate
κ, κ^*	dihedral angle; effective dihedral angle
ψ, ψ^*	sweep angle; effective sweep angle
λ	tip-speed-ratio of the rotor
λ_r	local speed ratio at a blade section
Λ_{tip}	<u>tip curve angle</u>
μ	<u>ratio of sines: 2-D sectional flow angle ϕ to inflow angle φ</u>
ρ	density of air
ϕ	2-D sectional flow angle, in modified sectional coordinate system
φ	inflow angle
Ω	rotational speed

Table A3. Subscripts used in the present work.

Symbol	Description
1/4	at the 1/4 chord point
3/4	at the 3/4 chord point
x, y, z	in the x -, y - and z -directions
L, D, M	due to lift force; drag force; sectional moment
N	in normal direction
ma	main axis
x_c	at the x_{cp} -chord point
cp	at the calculation point
<u>tip</u>	<u>at the blade tip</u>
NC	non-circulatory term
BEM	from the BEM method
CFD	from the CFD solver
KJ	from the Kutta–Joukowski analysis

Table A4. Superscripts used in the present work.

Symbol	Description
B	in blade root coordinate system
BL	in blade local coordinate system
S	in sectional coordinate system
S*	in modified sectional coordinate system
str	straight blade
cur	curved blade
prebend	blade with only prebend and no sweep
sweep	blade with only sweep and no prebend
origin	original curved blade
mod	modified curved blade
acc	due to mid-chord heaving acceleration
tor	due to torsion rate
<u>proj</u>	<u>projection effect</u>
<u>wake</u>	<u>wake-induced effect</u>
<u>tot</u>	<u>total effects with wake-induced and projection effects combined</u>

Appendix B: BEM inductions for prescribed circulation

This section shows that, for a given spanwise circulation distribution, the blade element momentum (BEM) method converges to unique induction factors that are independent of the blade geometry (such as sweep or prebend).

1120 First, consider a prescribed spanwise circulation distribution Γ , which is then non-dimensionalized into k_s using Eq. (32). As shown in Eq. (38), the tangential induction factor a' is directly related to k_s . Substituting this expression into Eq. (34), the Kutta–Joukowski thrust coefficient $C_{t,KJ}$ (excluding radial induction) is obtained as:

$$C_{t,KJ} = k_s \left(1 + \frac{k_s}{4\lambda_r^2} \right). \quad (\text{B1})$$

This shows that $C_{t,KJ}$ is fully determined by k_s and the local speed ratio λ_r , with no direct dependence on blade geometry.

1125 Despite the circulation distribution being prescribed, the BEM method still requires iteration to reach a converged solution, due to the application of the tip-loss correction to the axial induction. According to Eq. (36), the blade axial induction factor a_B depends on the Kutta–Joukowski thrust coefficient $C_{t,KJ}$ and the inflow angle φ :

$$a_B = f_1(k_s, \varphi). \quad (\text{B2})$$

Here, we express a_B as a function of k_s and φ , noting that $C_{t,KJ}$ depends entirely on k_s .

1130 Next, consider the inflow angle φ . By substituting the expression for a' in Eq. (38) into the definition of the inflow angle φ in Eq. (15), we find that φ can be represented as a function of a_B and k_s :

$$\varphi = f_2(k_s, a_B). \quad (\text{B3})$$

Substituting φ from Eq. (B3) back into Eq. (B2), we arrive at:

$$a_B = f_1(k_s, f_2(k_s, a_B)). \quad (\text{B4})$$

1135 This results in an implicit equation for a_B , which can be solved iteratively where k_s is the only prescribed parameter. As a result, once k_s is fixed, the iterative procedure converges to a unique a_B that is independent of geometric modifications to the blade (e.g., sweep or prebend), providing these changes do not affect the blade radius.

In conclusion, given a prescribed circulation distribution, the BEM method will converge to the same inductions and also the same Kutta–Joukowski thrust and power coefficients, regardless of the blade geometry.

1140 Appendix C: Contribution of non-circulatory force and moment

In this section, we derive the total contribution of non-circulatory forces and moments to the local thrust and power coefficients under steady-state operational conditions. Although the 1/4 chord line is chosen as the main reference axis for simplicity, the conclusions presented here are general and can be extended to other main axis definitions as discussed in Sect. 2.8.2.

1145 Non-circulatory forces and moments arise when the airfoil experiences effective motions, specifically: a mid-chord heaving acceleration ($\ddot{\epsilon}$) perpendicular to the chord line and a torsion rate ($\dot{\theta}$). Under steady-state conditions, these effective motions

are only due to the projection of the rotor's angular velocity and centrifugal acceleration originating from rotor rotation. The mid-chord heaving acceleration $\ddot{\epsilon}$ is defined to be positive when directed from the pressure side to the suction side of the airfoil. The torsion rate $\dot{\theta}$ is defined to be positive in the nose-up direction. The expressions for $\ddot{\epsilon}$ and $\dot{\theta}$ are given in Eqs. (26) and (24), respectively.

1150 First, there are non-circulatory normal forces perpendicular to the airfoil arise due to mid-chord heaving acceleration and torsion rate. The corresponding force coefficients are given by:

$$C_{N,NC}^{\text{acc}} = -\frac{\pi c \ddot{\epsilon}}{2V_{\text{rel}}^2} = -\pi T_0 \frac{\ddot{\epsilon}}{V_{\text{rel}}}, \quad (\text{C1})$$

$$C_{N,NC}^{\text{tor}} = \frac{\pi c \dot{\theta}}{2V_{\text{rel}}} = \pi T_0 \dot{\theta}. \quad (\text{C2})$$

Here, the time constant T_0 is introduced, following literature (Hansen et al., 2004; Bergami and Gaunaa, 2012).

$$1155 \quad T_0 = \frac{c}{2V_{\text{rel}}} \quad (\text{C3})$$

Additionally, there are sectional moments due to mid-chord acceleration and torsion rate, with corresponding moment coefficients at the 1/4 chord point being:

$$C_{M,NC}^{\text{acc}} = \frac{\pi c \ddot{\epsilon}}{8V_{\text{rel}}^2} = \frac{1}{4} \pi T_0 \frac{\ddot{\epsilon}}{V_{\text{rel}}} = -\frac{1}{4} C_{N,NC}^{\text{acc}}, \quad (\text{C4})$$

$$C_{M,NC}^{\text{tor}} = -\frac{\pi c \dot{\theta}}{4V_{\text{rel}}} = -\frac{1}{2} \pi T_0 \dot{\theta} = -\frac{1}{2} C_{N,NC}^{\text{tor}}. \quad (\text{C5})$$

1160 Summing these components, the total non-circulatory normal force and moment coefficients are:

$$C_{N,NC} = C_{N,NC}^{\text{acc}} + C_{N,NC}^{\text{tor}} = \pi T_0 \left(\dot{\theta} - \frac{\ddot{\epsilon}}{V_{\text{rel}}} \right), \quad (\text{C6})$$

$$C_{M,NC} = C_{M,NC}^{\text{acc}} + C_{M,NC}^{\text{tor}} = -\frac{1}{4} C_{N,NC} - \frac{1}{4} \pi T_0 \dot{\theta}. \quad (\text{C7})$$

Additionally, a non-circulatory drag force due to the torsion rate (Li et al., 2022c) is accounted for:

$$C_{D,NC}^{\text{tor}} = -\frac{\pi c^2 \dot{\theta}^2}{8V_{\text{rel}}^2} = -\frac{1}{2} \pi T_0^2 \dot{\theta}^2. \quad (\text{C8})$$

1165 The non-circulatory lift and drag coefficients at the 1/4 chord point are:

$$C_{L,NC} = C_{N,NC} \cos \alpha_{1/4}, \quad (\text{C9})$$

$$C_{D,NC} = C_{N,NC} \sin \alpha_{1/4} + C_{D,NC}^{\text{tor}}. \quad (\text{C10})$$

These lift and drag increments, together with the moment term, are incorporated into the thrust and power coefficient formulations in Eqs. (64) to (66) to determine their net effects:

$$1170 \quad \Delta C_{t,L,NC} = C_{t,KJ} \frac{C_{L,NC}}{C_L}, \quad (C11)$$

$$\Delta C_{t,D,NC} = C_{t,KJ} \frac{C_{D,NC}}{C_L} \frac{1}{\|\mathbf{t}^*\|} \left(\frac{\tan \varphi}{\cos^2 \psi^*} + \tan \psi^* \tan \kappa^* \right), \quad (C12)$$

$$\Delta C_{p,L,NC} = \lambda_r C_{t,KJ} \frac{C_{L,NC}}{C_L} \tan \varphi, \quad (C13)$$

$$\Delta C_{p,D,NC} = -\lambda_r C_{t,KJ} \frac{C_{D,NC}}{C_L} \frac{1}{\|\mathbf{t}^*\|} \left(\frac{1}{\cos^2 \kappa^*} + \tan \varphi \tan \kappa^* \tan \psi^* \right), \quad (C14)$$

$$\Delta C_{p,M,NC} = -\lambda_r C_{t,KJ} \frac{C_{M,NC}}{C_L} \frac{e^{\text{str}} \tan \kappa^*}{r \cos \varphi}. \quad (C15)$$

1175 It can be further concluded that the non-circulatory lift and drag contribute to both thrust and power, while the non-circulatory moment only contributes to power. Further, the contribution of the non-circulatory torsion rate drag in Eq. (C8) to thrust is negligible since its magnitude is much smaller than the lift force. Nevertheless, its contribution to power is still considered in this study. In addition, approximations are applied, assuming small sweep, prebend and inflow angles. The total contribution of non-circulatory forces and moments to the local thrust and power coefficients is approximated as:

$$1180 \quad \Delta C_{t,NC} = \Delta C_{t,L,NC} + \Delta C_{t,D,NC} \\ \approx \frac{C_{t,KJ}}{C_L} C_{N,NC} \left[\cos \alpha_{1/4} + \frac{\sin \alpha_{1/4}}{\|\mathbf{t}^*\|} \left(\frac{\tan \varphi}{\cos^2 \psi^*} + \tan \psi^* \tan \kappa^* \right) \right], \quad (C16)$$

$$\Delta C_{p,NC} = \Delta C_{p,L,NC} + \Delta C_{p,D,NC} + \Delta C_{p,M,NC} \\ \approx \lambda_r \frac{C_{t,KJ}}{C_L} \left(C_{N,NC} \cos \alpha_{1/4} \tan \varphi - \frac{C_{N,NC} \sin \alpha_{1/4} + C_{D,NC}^{\text{tor}}}{\|\mathbf{t}^*\| \cos^2 \kappa^*} - \frac{C_{M,NC} e^{\text{str}} \tan \kappa^*}{r \cos \varphi} \right). \quad (C17)$$

C1 Straight blades forming a planar rotor

1185 For the special case where the blade is straight and forms a planar rotor, both the effective sweep angle ψ^* and the effective prebend angle κ^* are zero. Consequently, the projected effective mid-chord heaving acceleration $\ddot{\epsilon}$ and effective torsion rate $\dot{\theta}$ are also zero. As a result, the contributions of non-circulatory forces and moments to the local thrust and power coefficients are zero. This is also confirmed numerically in the following sections.

$$\Delta C_{t,NC}^{\text{str}} = 0 \quad (C18)$$

$$1190 \quad \Delta C_{p,NC}^{\text{str}} = 0 \quad (C19)$$

C2 Blades with only sweep

For the special condition where the blade has sweep but no prebend ($\kappa^* = 0$), the effective torsion rate and the mid-chord heaving acceleration, given in Eqs. (24) and (26), are simplified assuming both the effective sweep angle ψ^* and the twist

angle β are small:

$$1195 \quad \dot{\theta} = 0, \tag{C20}$$

$$\ddot{\varepsilon} = -\Omega^2 r \sin \psi^* \sin \beta \approx 0. \tag{C21}$$

Therefore, the total contributions of non-circulatory forces and moments to the thrust and power coefficients are approximately zero:

$$\Delta C_{t,NC}^{\text{sweep}} \approx 0, \tag{C22}$$

$$1200 \quad \Delta C_{p,NC}^{\text{sweep}} \approx 0. \tag{C23}$$

Numerical simulations were performed using the backward swept blades mB-1 to mB-4, whose parameters are listed in Table 3. Comparisons across different operational conditions, listed in Table 1, confirm these approximations. In addition, the baseline straight blade is included as a reference. The results for the non-circulatory force and moment contributions to the local thrust and power coefficients are shown in Fig. C1.

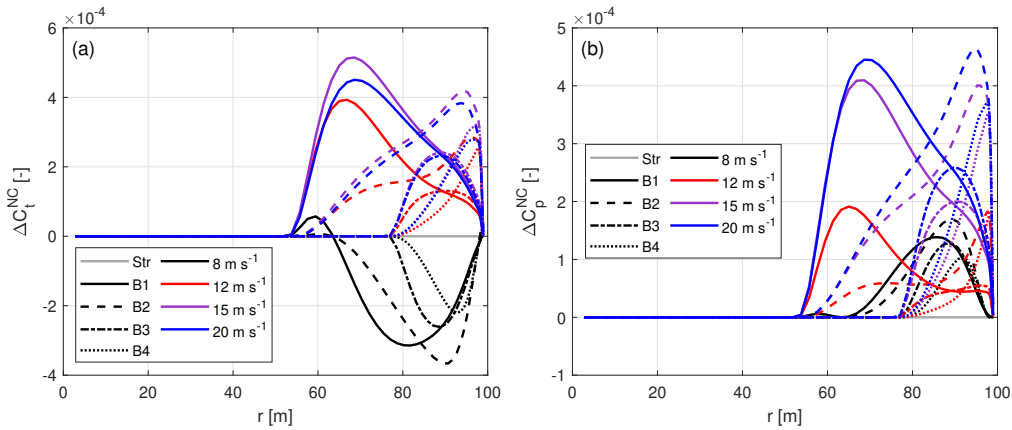


Figure C1. Contributions of the non-circulatory forces (a) and moments (b) to the local thrust and power coefficients of the baseline straight blade and the modified backward swept blades mB-1 to mB-4, at different wind speeds.

1205 For the baseline straight blade, the total contributions of non-circulatory forces and moments to thrust and power are zero. For the four backward swept blades, the maximum magnitude of the local thrust and power coefficients due to the non-circulatory forces and moments is only 5.1×10^{-4} and 4.6×10^{-4} , respectively, which are negligible.

C3 Blades with only prebend

For the special condition where the blade has prebend but no sweep ($\psi^* = 0$), the effective torsion rate and the mid-chord heaving acceleration are:

$$\dot{\theta} = -\Omega \sin \kappa, \quad (\text{C24})$$

$$\ddot{\epsilon} = -\Omega^2 r \sin \kappa \cos \beta. \quad (\text{C25})$$

Substituting these into Eq. (C6), the non-circulatory normal force coefficient becomes:

$$C_{N,NC} = -\pi T_0 \Omega \sin \kappa \left(1 - \frac{\Omega r \cos \beta}{V_{\text{rel}}} \right). \quad (\text{C26})$$

1215 Assuming that the tangential induction factor a' is much smaller than 1, the following approximation can be made:

$$\Omega r \approx \Omega r (1 + a') = V \cos \varphi. \quad (\text{C27})$$

Further, inserting Eq. (21) and assuming the inflow angle φ and the twist angle β are both small angles, the non-circulatory normal force is then approximately zero.

$$C_{N,NC} \approx -\pi T_0 \Omega \sin \kappa (1 - \cos \varphi \cos \beta) \approx 0 \quad (\text{C28})$$

1220 Inserting Eq. (C28) into Eqs. (C16) and (C17), the contributions to the thrust and power coefficients are approximately zero:

$$\Delta C_{t,NC}^{\text{prebend}} \approx 0, \quad (\text{C29})$$

$$\Delta C_{p,NC}^{\text{prebend}} \approx -\lambda_r \frac{C_{t,KJ}}{C_L} \left(\frac{C_{D,NC}^{\text{tor}}}{\cos \kappa} + \frac{C_{M,NC} c^{\text{str}} \tan \kappa}{r \cos \varphi} \right). \quad (\text{C30})$$

Inserting Eq. (C28) into Eq. (C7), the non-circulatory moment coefficient is approximated as:

$$C_{M,NC} \approx -\frac{1}{4} \pi T_0 \dot{\theta}. \quad (\text{C31})$$

1225 Further, inserting Eqs. (C8) and (C31) into Eq. (C30), the equation is further manipulated to be:

$$\Delta C_{p,NC}^{\text{prebend}} \approx \frac{1}{4} \pi T_0 \dot{\theta} \lambda_r \frac{C_{t,KJ}}{C_L} \tan \kappa \left(\frac{-\Omega c}{V_{\text{rel}}} + \frac{c^{\text{str}}}{r \cos \varphi} \right). \quad (\text{C32})$$

With further substitutions from Eqs. (62) and (C27) and assuming small inflow angle φ , the total contribution to the local power coefficient from non-circulatory forces and moments is approximately zero.

$$\Delta C_{p,NC}^{\text{prebend}} \approx -\frac{1}{4} \pi T_0 \dot{\theta} \lambda_r \frac{C_{t,KJ}}{C_L} \frac{\Omega c \tan \kappa}{V} \left(1 - \frac{1}{\cos^2 \varphi} \right) \approx 0 \quad (\text{C33})$$

1230 To confirm this numerically, the upwind prebent blades mW-1 to mW-4, with parameters listed in Table 3, at different operational conditions listed in Table 1 are used for comparison. The contribution of the non-circulatory force and moment to the local thrust and power coefficients is shown in Fig. C2.

For these four upwind prebent blades, the maximum contributions of non-circulatory forces and moments to the local thrust and power coefficients are only 1.5×10^{-4} , which are negligible.

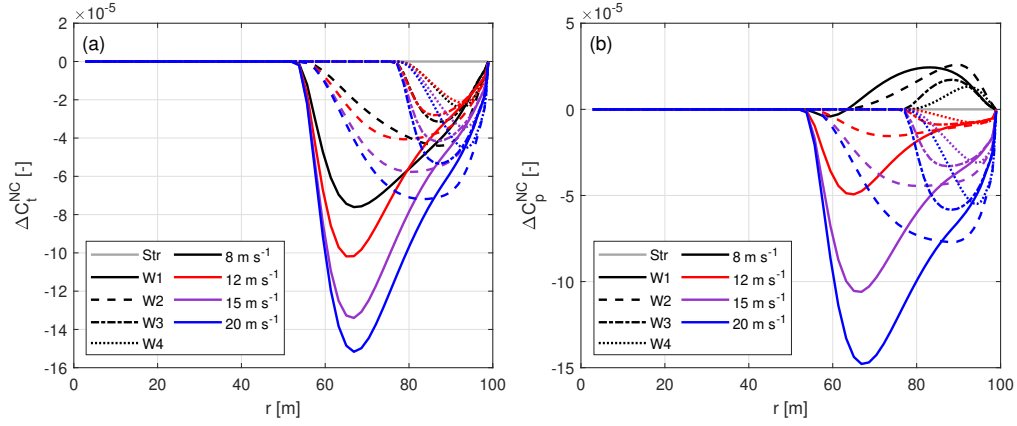


Figure C2. Contributions of the non-circulatory forces (a) and moments (b) to the local thrust and power coefficients of the baseline straight blade and the modified upwind prebent blades mW-1 to mW-4, at different wind speeds.

1235 C4 Blades with sweep and prebend combined

For the generalized case where the blade has both sweep and prebend combined, the expression for the mid-chord heaving acceleration becomes more complex. To simplify the derivation, approximations are firstly applied. Given that both the effective sweep angle ψ^* and the modified twist angle β^* are small, Eq. (26) can be approximated as:

$$\ddot{\varepsilon} \approx -\Omega^2 r \sin \kappa^* \cos \beta^*. \quad (\text{C34})$$

1240 Substituting Eqs. (24) and (C34) into Eq. (C6), the non-circulatory normal force coefficient becomes:

$$C_{N,NC} \approx -\pi T_0 \Omega \tan \kappa^* \left(\frac{1}{\|\mathbf{t}^*\|} - \frac{\Omega r \cos \beta^* \cos \kappa^*}{V_{rel}} \right). \quad (\text{C35})$$

By inserting Eq. (21) and applying the approximation in Eq. (C27), further simplifications are made. Further, assume ψ^* , κ^* , β^* and the inflow angle φ are all small angles for the region where the blade has sweep or prebend, the non-circulatory normal force is then approximately zero.

$$1245 \quad C_{N,NC} \approx -\pi T_0 \Omega \tan \kappa^* \left(\frac{1}{\|\mathbf{t}^*\|} - \mu \cos \varphi \cos \beta^* \right) \approx 0 \quad (\text{C36})$$

Substituting Eq. (C36) into Eqs. (C16) and (C17), the total contributions to the local thrust and power coefficients are:

$$\Delta C_{t,NC} \approx 0, \quad (\text{C37})$$

$$\Delta C_{p,NC} \approx -\lambda_r \frac{C_{t,KJ}}{C_L} \left(\frac{C_{D,NC}^{tor}}{\|\mathbf{t}^*\| \cos^2 \kappa^*} + \frac{C_{M,NC}^{str} \tan \kappa^*}{r \cos \varphi} \right). \quad (\text{C38})$$

1250 Inserting Eq. (C36) into Eq. (C7), the approximated non-circulatory moment coefficient takes the same form as for the special case with prebend only:

$$C_{M,NC} \approx -\frac{1}{4} \pi T_0 \dot{\theta}. \quad (\text{C39})$$

Next, substituting Eqs. (C8) and (C39) into Eq. (C38), we manipulate the expression further:

$$\Delta C_{p,NC} \approx -\frac{1}{4}\pi T_0 \dot{\theta} \lambda_r \frac{C_{t,KJ}}{C_L} \tan \kappa^* \left(\frac{\Omega c}{V_{rel} \|\mathbf{t}^*\|^2 \cos^2 \kappa^*} - \frac{c^{str}}{r \cos \varphi} \right). \quad (C40)$$

By assuming ψ^* is small and inserting Eq. (7), the norm can be approximated as:

$$1255 \quad \|\mathbf{t}^*\|^2 = 1 + \tan^2 \kappa^* + \tan^2 \psi^* \approx 1 + \tan^2 \kappa^* = \frac{1}{\cos^2 \kappa^*}. \quad (C41)$$

Inserting Eqs. (51), (52) and (C27) and assuming the 2-D flow angle ϕ is similar to the inflow angle φ , so $\mu \approx 1$. Furthermore, assuming κ^* and φ are small angles, the total contribution of the non-circulatory forces and moments to the local power coefficient becomes approximately zero.

$$\Delta C_{p,NC} \approx -\frac{1}{4}\pi T_0 \dot{\theta} \lambda_r \frac{C_{t,KJ}}{C_L} \frac{\Omega c^{str} \tan \kappa^*}{V} \left(\frac{\mu^2}{\cos^2 \kappa^*} - \frac{1}{\cos^2 \varphi} \right) \approx 0 \quad (C42)$$

1260 To validate these derivations, numerical comparisons were conducted using blades mC-11, mC-55, mC-15 and mC-51 with sweep and prebend $\dot{\theta}$ combined. Operational conditions are detailed in Table 1. The contributions of the non-circulatory forces and moments to the local thrust and power coefficients are shown in Fig. C3.

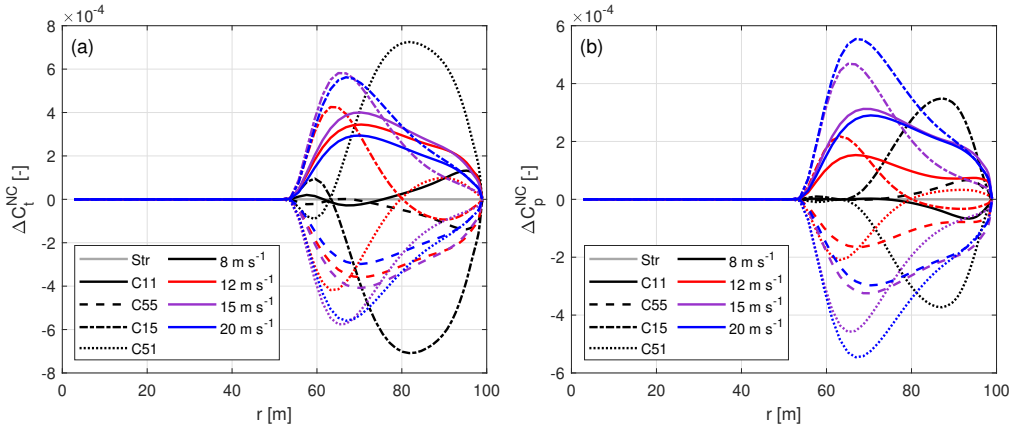


Figure C3. Contributions of non-circulatory forces (a) and moments (b) to the local thrust and power coefficients of the baseline straight blade and the modified curved blades mC-11, mC-55, mC-15, mC-51, at different wind speeds.

For these four combined curved blades, the maximum magnitude of contributions of non-circulatory forces and moments to the local thrust and power coefficients are 7.2×10^{-4} and 5.5×10^{-4} , respectively, which are negligible.

D1 Straight blades

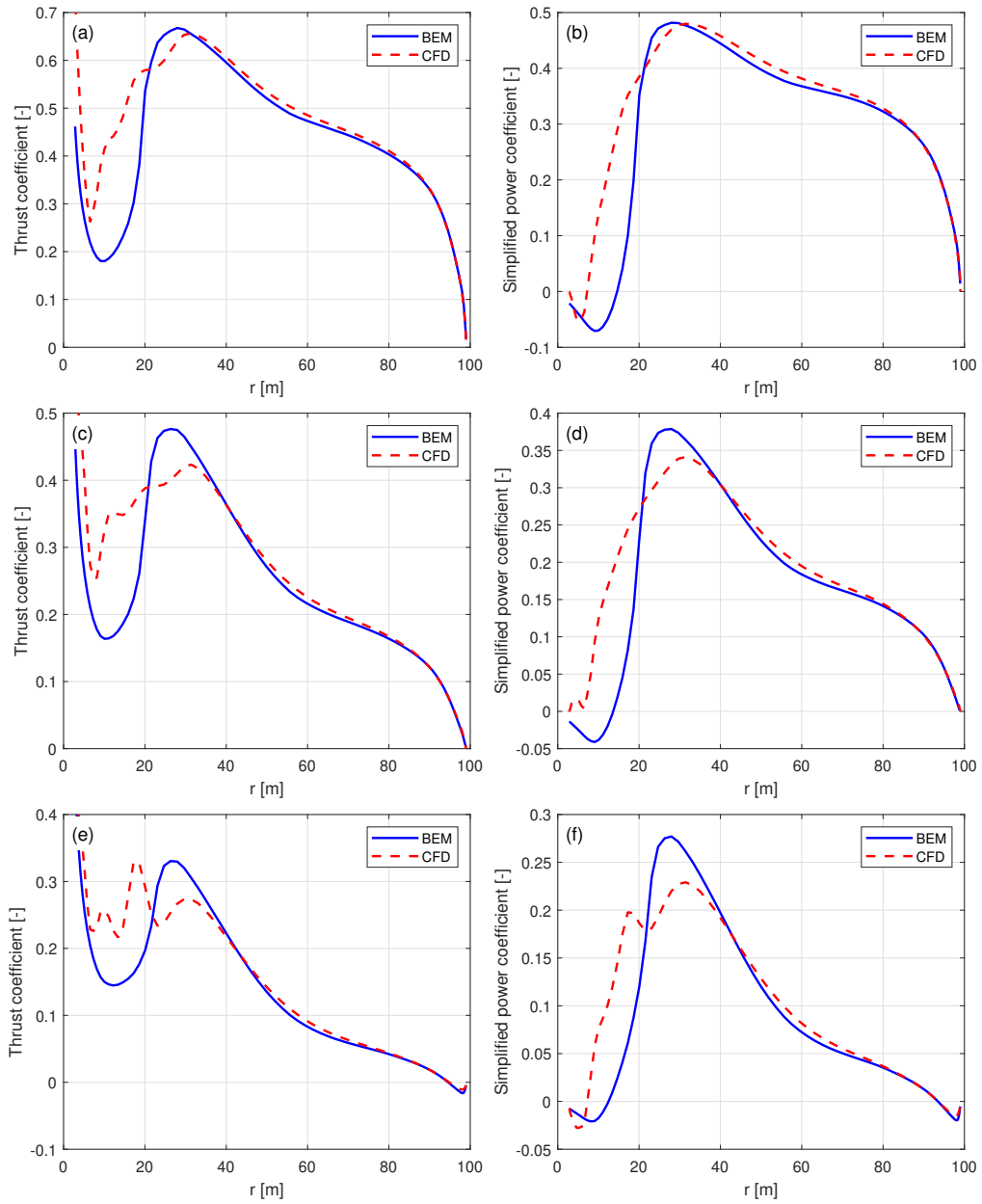


Figure D1. Thrust coefficient C_t and simplified power coefficient \tilde{C}_p of the baseline straight blade, for wind speeds at 12 m s^{-1} (a), (b); 15 m s^{-1} (c), (d); and 20 m s^{-1} (e), (f).

D2 Blades with only sweep

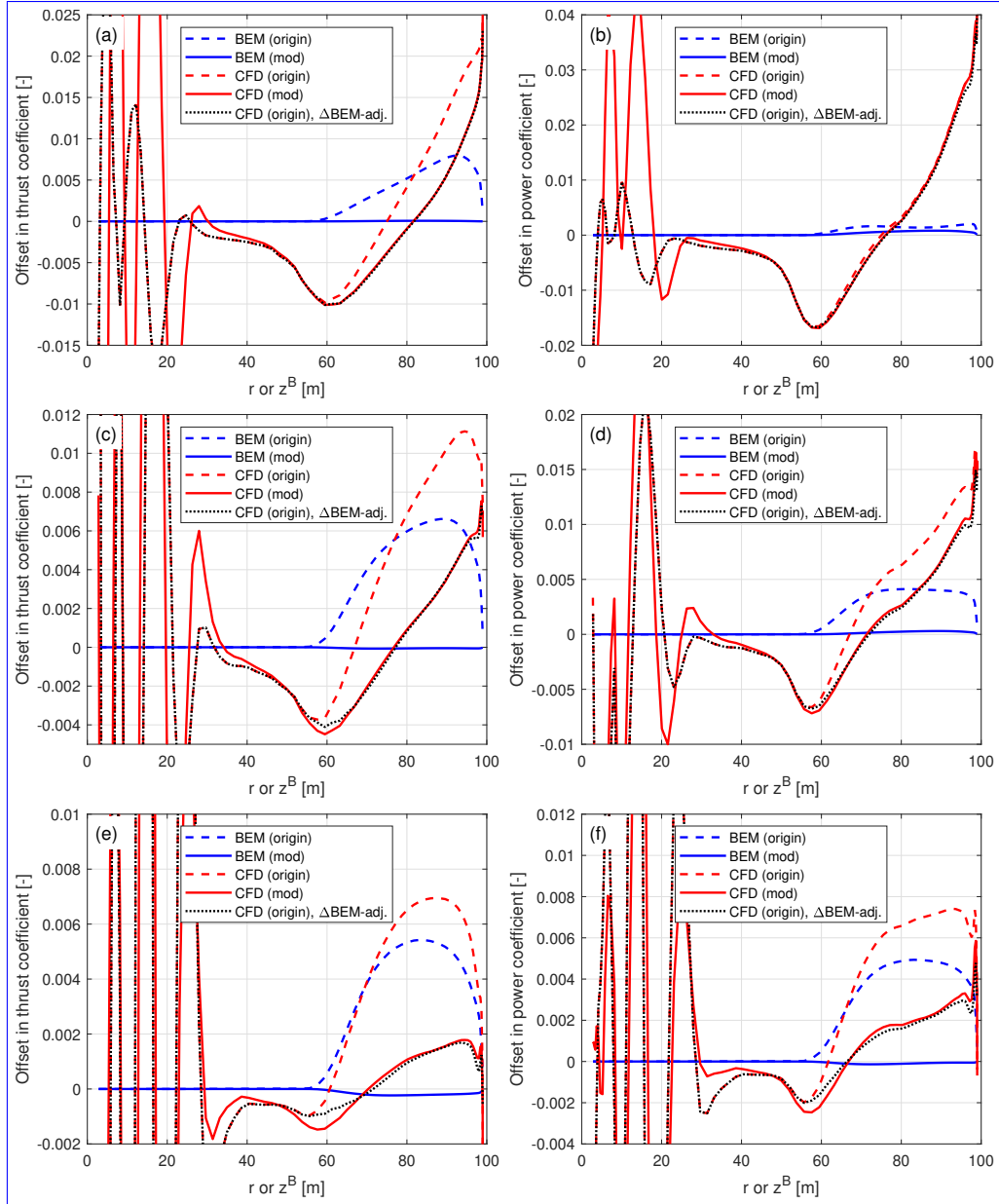


Figure D2. Offset in thrust coefficient ΔC_t and simplified power coefficients $\Delta \tilde{C}_p$ and $\Delta \hat{C}_p$ of the original and modified backward swept blades B-1-Uv and mB-1-Uv compared to the baseline straight blade, for wind speeds at 12 m s^{-1} (a), (b); 15 m s^{-1} (c), (d); and 20 m s^{-1} (e), (f).

D3 Blades with only prebend

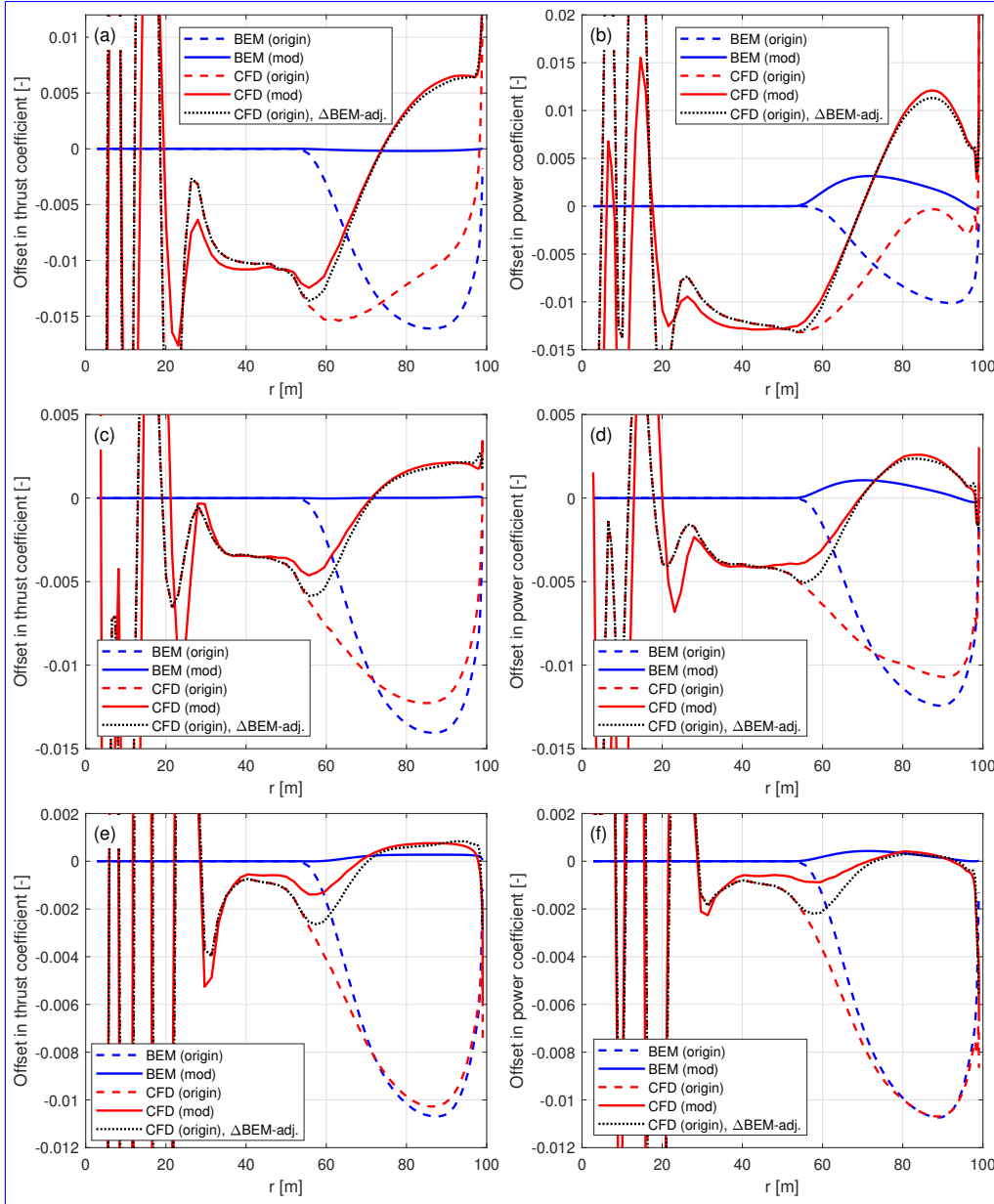


Figure D3. Offset in thrust coefficient ΔC_t and simplified power coefficient $\Delta \tilde{C}_p$ of the original and modified upwind prebent blades W-1-Uv and mW-1-Uv compared to the baseline straight blade, for wind speeds at 12 m s^{-1} (a), (b); 15 m s^{-1} (c), (d); and 20 m s^{-1} (e), (f).

D4 Blades combining sweep and prebend

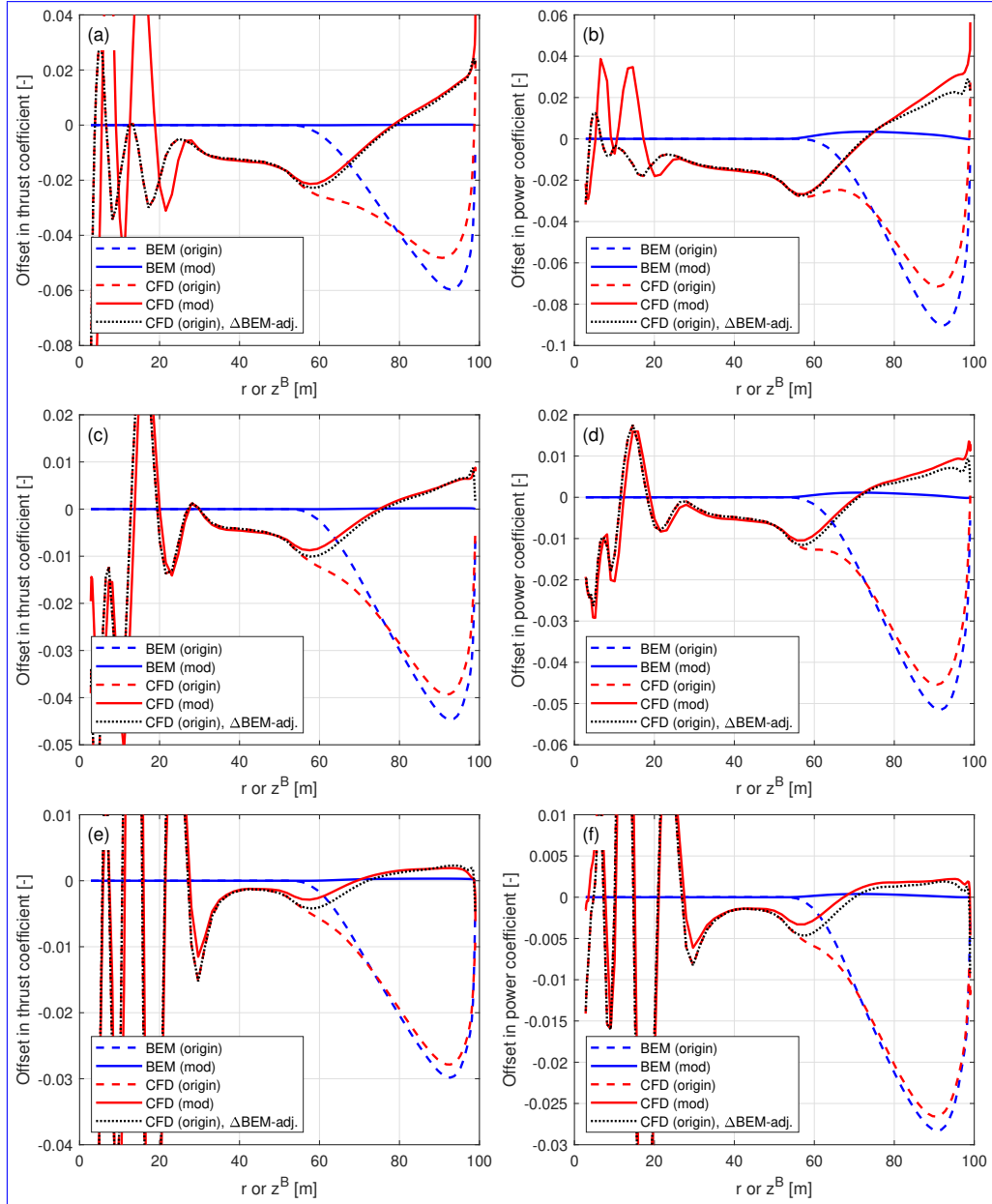


Figure D4. Offset in thrust coefficient ΔC_t and simplified power coefficients $\Delta \tilde{C}_p$ and $\Delta \hat{C}_p$ of the original and modified curved blades C-11-Uv and mC-11-Uv with backward sweep and upwind prebend combined, compared to the baseline straight blade: at 12 m s⁻¹ (a), (b); 15 m s⁻¹ (c), (d); and 20 m s⁻¹ (e), (f).

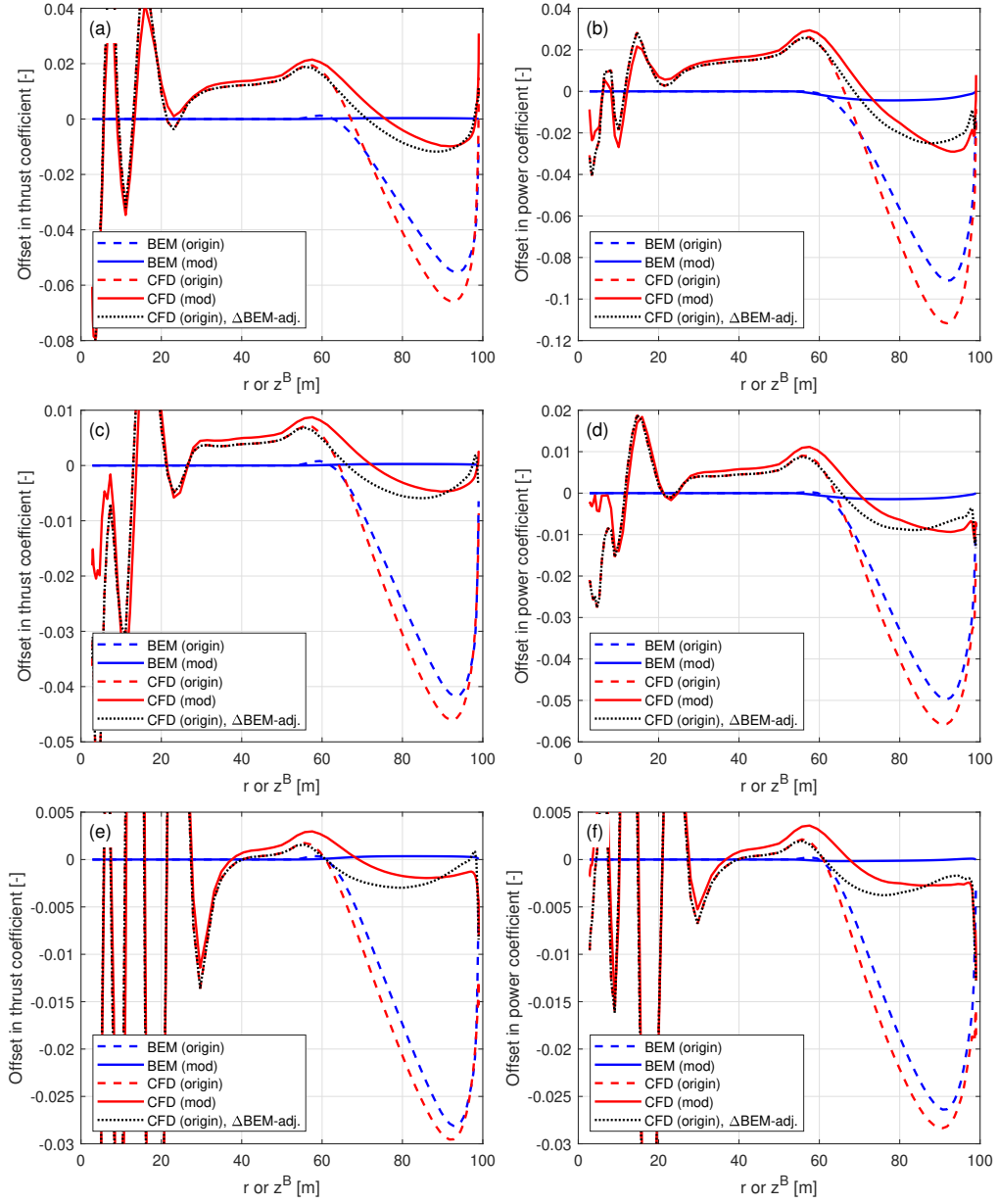


Figure D5. Offset in thrust coefficient ΔC_t and simplified power coefficients $\Delta \tilde{C}_p$ and $\Delta \hat{C}_p$ of the original and modified curved blades C-55-Uv and mC-55-Uv with forward sweep and downwind prebend combined, compared to the baseline straight blade: at 12 m s^{-1} (a), (b); 15 m s^{-1} (c), (d); and 20 m s^{-1} (e), (f).

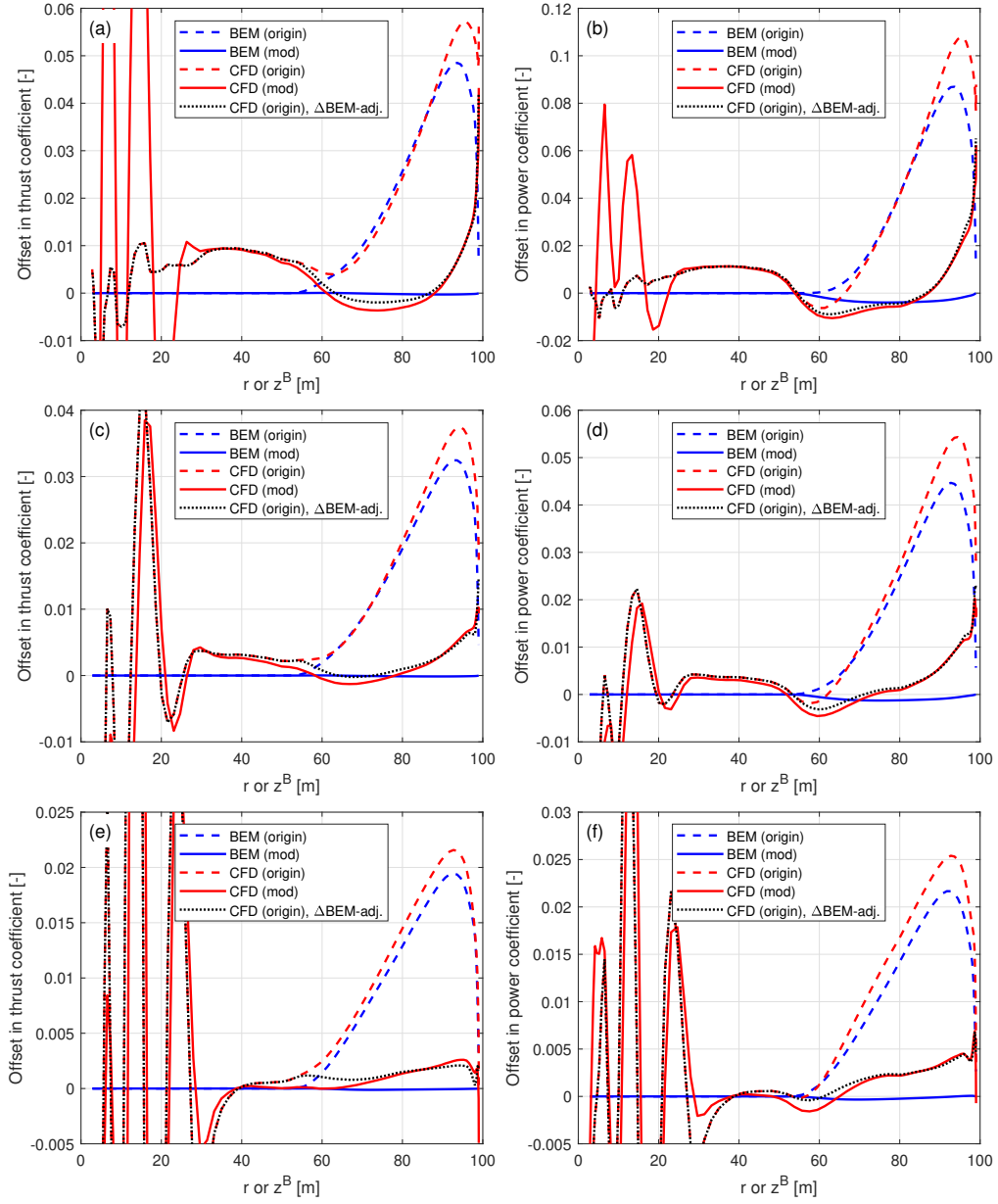


Figure D6. Offset in thrust coefficient ΔC_t and simplified power coefficients $\Delta \tilde{C}_p$ and $\Delta \hat{C}_p$ of the original and modified blades C-15-Uv and mC-15-Uv with backward sweep and downwind prebend combined, compared to the baseline straight blade: at 12 m s^{-1} (a), (b); 15 m s^{-1} (c), (d); and 20 m s^{-1} (e), (f).

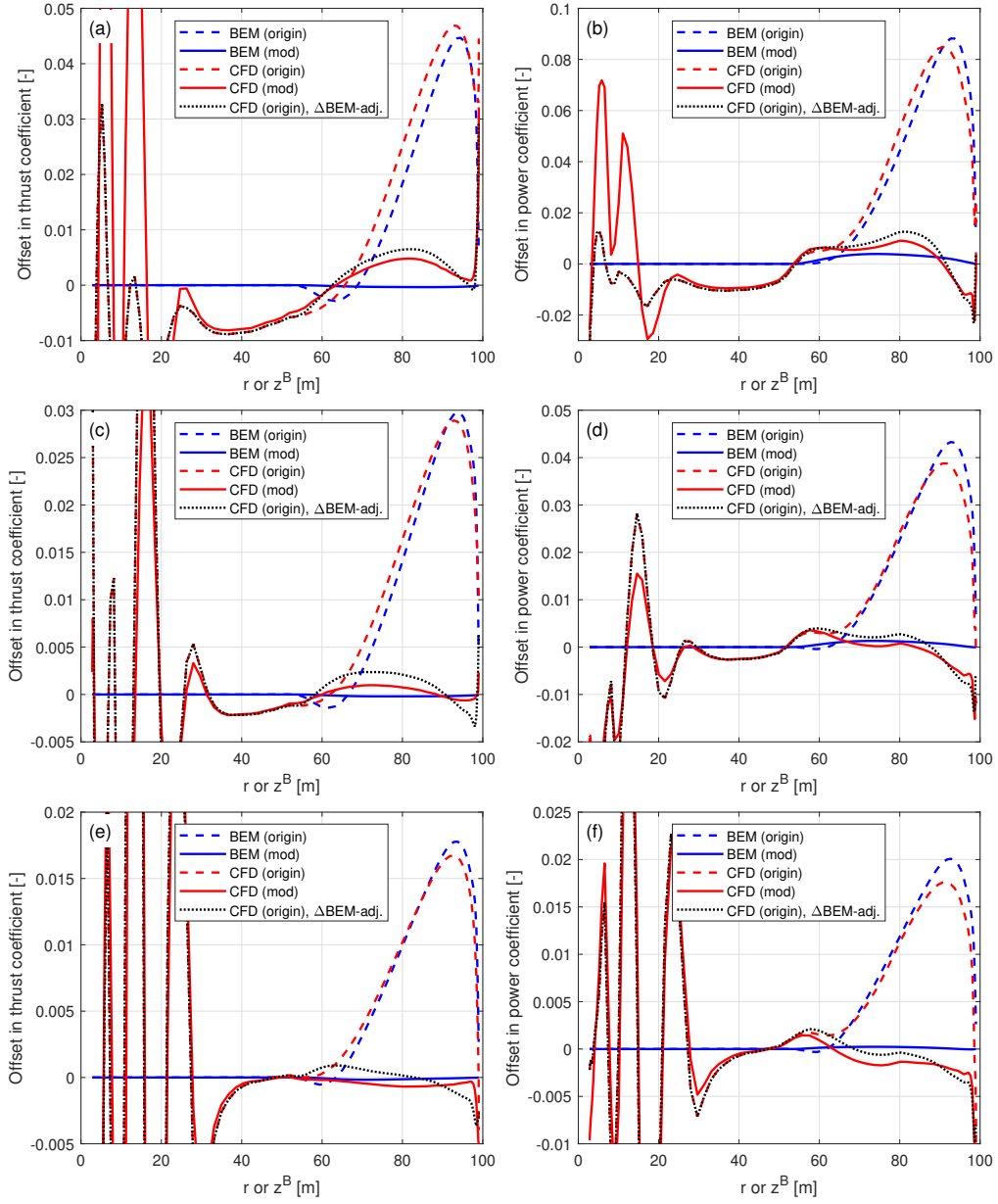


Figure D7. Offset in thrust coefficient ΔC_t and simplified power coefficients $\Delta \tilde{C}_p$ and $\Delta \hat{C}_p$ of the original and modified curved blades C-51-Uv and mC-51-Uv with forward sweep and upwind prebend combined, compared to the baseline straight blade: at 12 m s^{-1} (a), (b); 15 m s^{-1} (c), (d); and 20 m s^{-1} (e), (f).

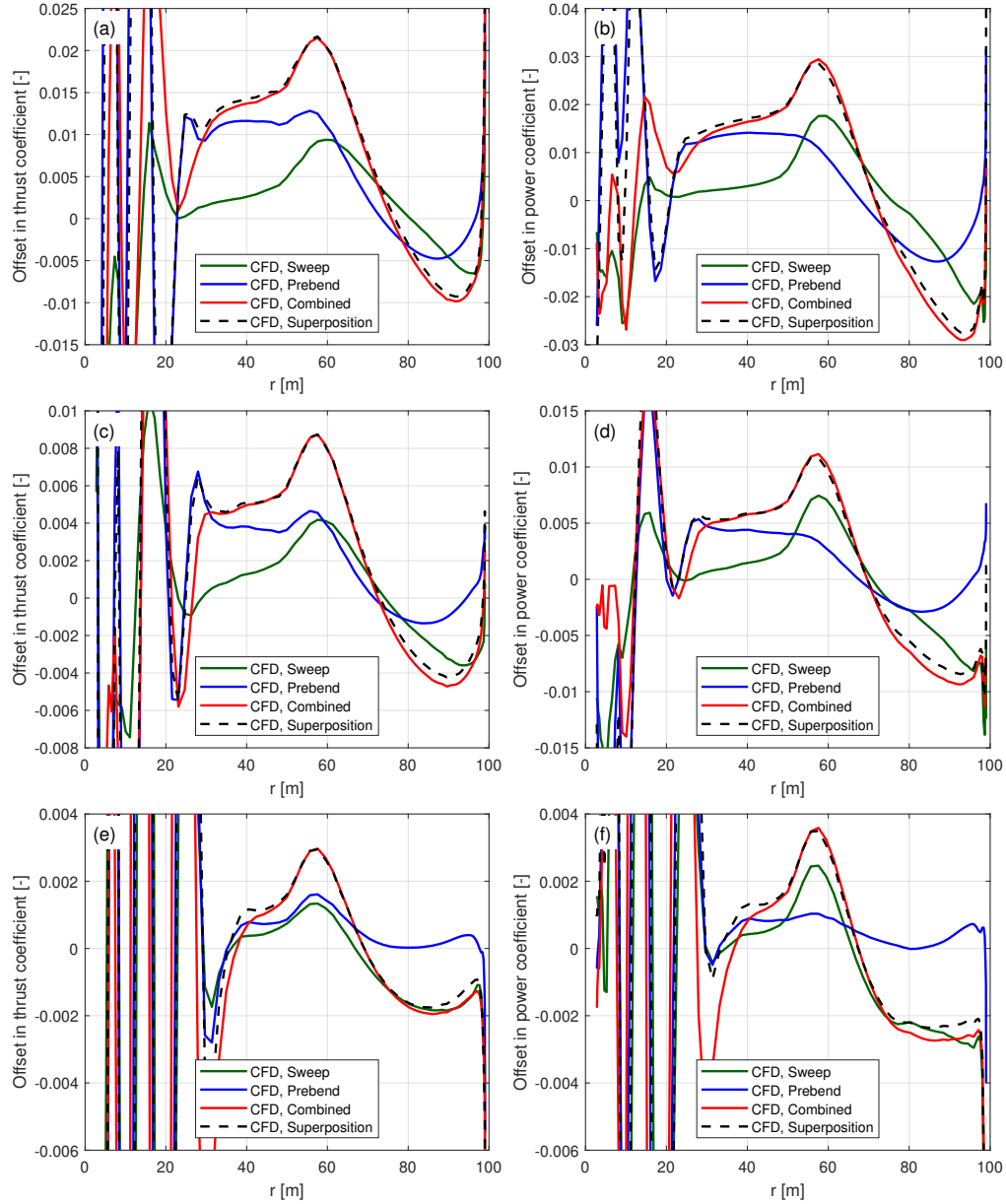


Figure D8. Offset in thrust coefficient ΔC_t and simplified power coefficient $\Delta \tilde{C}_p$ of the modified forward swept blades mB-5-Uv, the modified downwind prebent blades mW-5-Uv, the modified curved blade mC-55-Uv with both forward sweep and downwind prebend combined and the superposition of the sweep and prebend offsets, compared to the baseline straight blade: at 12 m s^{-1} (a), (b); 15 m s^{-1} (c), (d); and 20 m s^{-1} (e), (f).

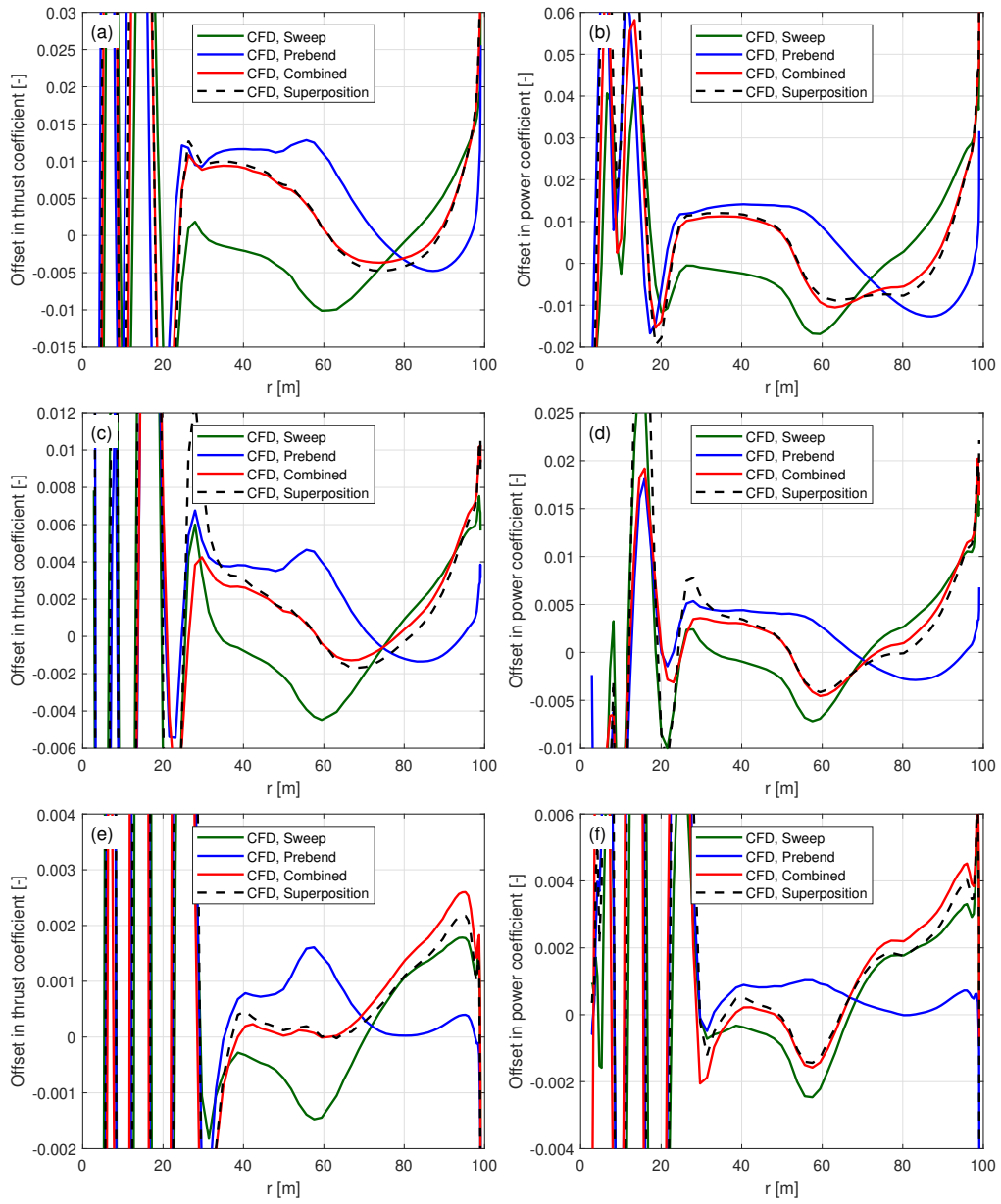


Figure D9. Offset in thrust coefficient ΔC_t and simplified power coefficient $\Delta \tilde{C}_p$ of the modified backward swept blades mB-1-Uv, the modified downwind prebend blades mW-5-Uv, the modified curved blade mC-15-Uv with both backward sweep and downwind prebend combined and the superposition of the sweep and prebend offsets, compared to the baseline straight blade: at 12 m s^{-1} (a), (b); 15 m s^{-1} (c), (d); and 20 m s^{-1} (e), (f).

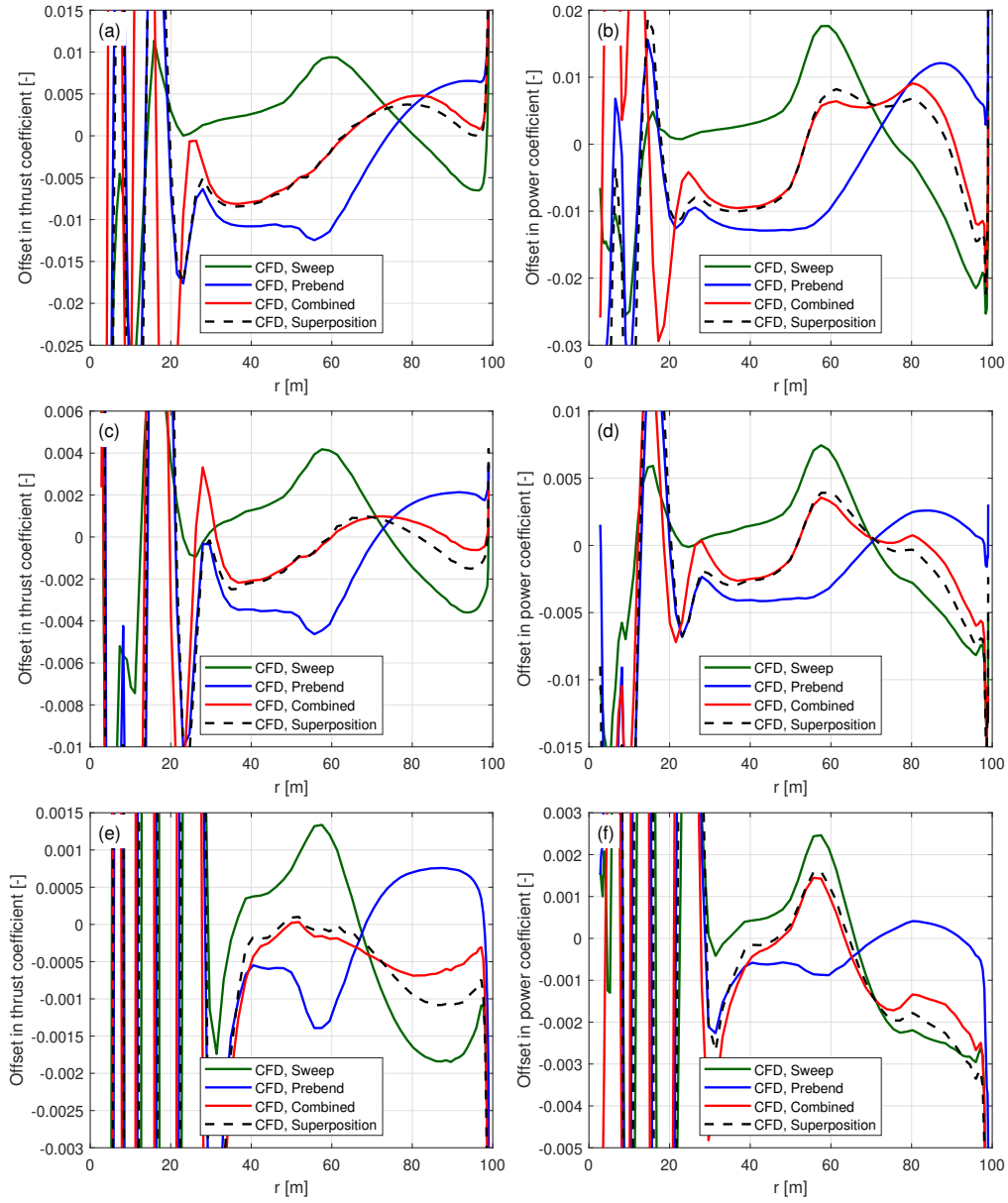


Figure D10. Offset in thrust coefficient ΔC_t and simplified power coefficient $\Delta \tilde{C}_p$ of the modified forward swept blades mB-5-Uv, the modified upwind prebend blades mW-1-Uv, the modified curved blade mC-51-Uv with both forward sweep and upwind prebend combined and the superposition of the sweep and prebend offsets, compared to the baseline straight blade: at 12 m s^{-1} (a), (b); 15 m s^{-1} (c), (d); and 20 m s^{-1} (e), (f).

Data availability. The 2-D airfoil data used in this article are generated with 2-D fully turbulent RANS computations (Bortolotti et al., 2019).

Author contributions. The concept of disentangling projection effects and wake geometry effects, as well as establishing a consistent framework for aerodynamic benchmarking originated from discussions among AL, MG, GRP and KL. In 2020, GRP conducted an initial study, demonstrating analytically and numerically that the BEM method is not able to predict an aerodynamic efficiency benefit for a swept blade compared to a straight blade. The application of the BEM method to general curved blades was described by AL, with contributions from MG, GRP and KL. The derivations of the modified chord and twist distributions were performed by AL. The derivations of the contribution of non-circulatory loads to a curved blade at steady-state conditions were also performed by AL. The results from the fully resolved CFD solver and the BEM method were computed and post-processed by AL, with co-authors contributing to analysis and interpretation. The overall analysis was conducted collaboratively by AL, MG, GRP and KL. All authors jointly formulated the study's conclusions and contributed to writing the manuscript.

Competing interests. DTU Wind and Energy Systems develops and distributes the Navier–Stokes solver EllipSys3D on commercial and academic terms. DTU Wind and Energy Systems also develops, supports and distributes HAWC2 on commercial terms, and HAWC2 is available free of charge for educational and academic research purposes.

Acknowledgements. The authors would like to thank their colleague Frederik Zahle at DTU Wind and Energy Systems for setting up the fully-scripted mesh generation and post-processing for the Reynolds-averaged Navier–Stokes (RANS) simulations in EllipSys3D. The authors would like to thank their colleague Antariksh Dicholkar at DTU Wind and Energy Systems for insightful discussions. Computational and storage resources were provided by the Sophia HPC Cluster at DTU (DOI: 10.57940/FAFC-6M81). This work was supported by the AMTip project, funded by the Energy Technology Development and Demonstration Program (EUDP) (Case no. 64021-2062). This paper was revised with the assistance of AI tools, including OpenAI's ChatGPT (GPT-3.5, GPT-4, GPT-4o, [GPT-4.1](#), [GPT-4.5](#), o1-preview and o1), which were used to generate suggestions to improve language and wording based on an existing draft. The manuscript underwent multiple rounds of revision by the authors, with AI-generated suggestions selectively incorporated and extensively modified.

References

- Barlas, T., Ramos-García, N., Pirrung, G. R., and González Horcas, S.: Surrogate-based aeroelastic design optimization of tip extensions on
1295 a modern 10 MW wind turbine, *Wind Energy Science*, 6, 491–504, <https://doi.org/10.5194/wes-6-491-2021>, 2021.
- Barlas, T., Pirrung, G. R., Ramos-García, N., González Horcas, S., Li, A., and Madsen, H. A.: Atmospheric rotating rig testing of a swept
blade tip and comparison with multi-fidelity aeroelastic simulations, *Wind Energy Science*, 7, 1957–1973, <https://doi.org/10.5194/wes-7-1957-2022>, 2022.
- Behrens de Luna, R., Marten, D., Barlas, T., Horcas, S. G., Ramos-García, N., Li, A., and Paschereit, C. O.: Comparison of different fidelity
1300 aerodynamic solvers on the IEA 10 MW turbine including novel tip extension geometries, *Journal of Physics. Conference Series*, 2265, 032 002, <https://doi.org/10.1088/1742-6596/2265/3/032002>, 2022.
- Bergami, L. and Gaunaa, M.: ATEFlap Aerodynamic Model, a dynamic stall model including the effects of trailing edge flap deflection, *Danmarks Tekniske Universitet, Risø Nationallaboratoriet for Bæredygtig Energi*, ISBN 9788755039346, 2012.
- Boorsma, K., Wenz, F., Lindenburg, K., Aman, M., and Kloosterman, M.: Validation and accommodation of vortex wake codes for wind
1305 turbine design load calculations, *Wind Energy Science*, 5, 699–719, <https://doi.org/10.5194/wes-5-699-2020>, 2020.
- Bortolotti, P., Tarrés, H. C., Dykes, K., Merz, K., Sethuraman, L., Verelst, D., and Zahle, F.: Systems Engineering in Wind En-
ergy - WP2.1 Reference Wind Turbines, Tech. rep., National Renewable Energy Laboratory (NREL), <https://www.osti.gov/biblio/1529216-iea-wind-tcp-task-systems-engineering-wind-energy-wp2-reference-wind-turbines>, (last access: 1 August 2024), 2019.
- Branlard, E.: Wind Turbine Aerodynamics and Vorticity-Based Methods: Fundamentals and Recent Applications, vol. 7 of *Research Topics
1310 in Wind Energy*, Springer, ISBN 978-3-319-55163-0, <https://doi.org/10.1007/978-3-319-55164-7>, 2017.
- Branlard, E. and Gaunaa, M.: Superposition of vortex cylinders for steady and unsteady simulation of rotors of finite tip-speed ratio, *Wind
Energy*, 19, 1307–1323, <https://doi.org/10.1002/we.1899>, 2015a.
- Branlard, E. and Gaunaa, M.: Cylindrical vortex wake model: right cylinder, *Wind Energy*, 18, 1973–1987, <https://doi.org/10.1002/we.1800>,
2015b.
- 1315 Branlard, E., Brownstein, I., Strom, B., Jonkman, J., Dana, S., and Baring-Gould, E. I.: A multipurpose lifting-line flow solver for arbitrary
wind energy concepts, *Wind Energy Science*, 7, 455–467, <https://doi.org/10.5194/wes-7-455-2022>, 2022.
- Dicholkar, A., Zahle, F., and Sørensen, N. N.: Convergence enhancement of SIMPLE-like steady-state RANS solvers applied to airfoil and
cylinder flows, *Journal of Wind Engineering and Industrial Aerodynamics*, 220, 104 863, 2022.
- Dicholkar, A., Lønbæk, K., Zahle, F., and Sørensen, N. N.: Stabilization of SIMPLE-like RANS solvers for computing accurate gra-
1320 dients using the complex-step derivative method, *Journal of Physics: Conference Series*, 2767, 052 022, <https://doi.org/10.1088/1742-6596/2767/5/052022>, 2024.
- Dicholkar, A., Lønbæk, K., Madsen, M. H. A., Zahle, F., and Sørensen, N. N.: From bluff bodies to optimal airfoils:
Numerically stabilized RANS solvers for reliable shape optimization, *Aerospace Science and Technology*, 161, 110 153,
<https://doi.org/10.1016/j.ast.2025.110153>, 2025.
- 1325 Fritz, E. K., Ferreira, C., and Boorsma, K.: An efficient blade sweep correction model for blade element momentum theory, *Wind Energy*,
25, 1977–1994, <https://doi.org/10.1002/we.2778>, 2022.
- Gaunaa, M.: Unsteady two-dimensional potential-flow model for thin variable geometry airfoils, *Wind Energy*, 13, 167–192,
<https://doi.org/10.1002/we.377>, 2010.
- Glauert, H.: Airplane Propellers, in: *Division L in Aerodynamic Theory*, vol. IV, Durand WF (ed.), pp. 169–360, Springer, 1935.

- 1330 Gözcü, O. and Verelst, D.: The effects of blade structural model fidelity on wind turbine load analysis and computation time, *Wind Energy Science*, 5, 503–517, <https://doi.org/10.5194/wes-5-503-2020>, 2020.
- Hansen, M. H., Gaunaa, M., and Madsen, H. A.: A Beddoes-Leishman type dynamic stall model in state-space and indicial formulations, Risø-R-1354, Roskilde, Denmark, 2004.
- Hoerner, S. F. and Borst, H. V.: Fluid-dynamic lift: practical information on aerodynamic and hydrodynamic lift, LA Hoerner, 1985.
- 1335 Horcas, S. G., Ramos-García, N., Li, A., Pirrung, G., and Barlas, T.: Comparison of aerodynamic models for horizontal axis wind turbine blades accounting for curved tip shapes, *Wind Energy*, 26, 5–22, <https://doi.org/10.1002/we.2780>, 2023.
- Larsen, T. and Hansen, A.: How 2 HAWC2, the user's manual, 1597(ver. 3-1)(EN), Risø National Laboratory, ISBN 9788755035836, 2007.
- Larwood, S. M. and Zutek, M.: Swept wind turbine blade aeroelastic modeling for loads and dynamic behavior, in: WINDPOWER 2006 Conference in Pittsburgh, USA, 2006.
- 1340 Li, A., Pirrung, G., Madsen, H. A., Gaunaa, M., and Zahle, F.: Fast trailed and bound vorticity modeling of swept wind turbine blades, *Journal of Physics: Conference Series*, 1037, 062 012, <https://doi.org/10.1088/1742-6596/1037/6/062012>, 2018.
- Li, A., Gaunaa, M., Pirrung, G. R., Ramos-García, N., and Horcas, S. G.: The influence of the bound vortex on the aerodynamics of curved wind turbine blades, *Journal of Physics: Conference Series*, 1618, 052 038, <https://doi.org/10.1088/1742-6596/1618/5/052038>, 2020.
- Li, A., Gaunaa, M., Lønbæk, K., Zahle, F., and Pirrung, G. R.: Comparison of aerodynamic planform optimization of non-planar rotors using blade element momentum method and a vortex cylinder model, *Journal of Physics: Conference Series*, 2265, 032 055, <https://doi.org/10.1088/1742-6596/2265/3/032055>, 2022a.
- 1345 Li, A., Gaunaa, M., Pirrung, G. R., and Horcas, S. G.: A computationally efficient engineering aerodynamic model for non-planar wind turbine rotors, *Wind Energy Science*, 7, 75–104, <https://doi.org/10.5194/wes-7-75-2022>, 2022b.
- Li, A., Gaunaa, M., Pirrung, G. R., Meyer Forsting, A., and Horcas, S. G.: How should the lift and drag forces be calculated from 2-D airfoil data for dihedral or coned wind turbine blades?, *Wind Energy Science*, 7, 1341–1365, <https://doi.org/10.5194/wes-7-1341-2022>, 2022c.
- 1350 Li, A., Pirrung, G. R., Gaunaa, M., Madsen, H. A., and Horcas, S. G.: A computationally efficient engineering aerodynamic model for swept wind turbine blades, *Wind Energy Science*, 7, 129–160, <https://doi.org/10.5194/wes-7-129-2022>, 2022d.
- Li, A., Gaunaa, M., Pirrung, G. R., and Lønbæk, K.: How does the blade element momentum method see swept or prebent blades?, *Journal of Physics: Conference Series*, 2767, 022 033, <https://doi.org/10.1088/1742-6596/2767/2/022033>, 2024.
- 1355 Li, A., Gaunaa, M., Pirrung, G. R., and Lønbæk, K.: Internet Appendix for: "Disentangling wake and projection effects in the aerodynamics of wind turbines with curved blades", <https://doi.org/10.5281/zenodo.13149533>, Internet Appendix, 2025.
- Liebst, B. S.: Wind turbine gust load alleviation utilizing curved blades, *Journal of Propulsion and Power*, 2, 371–377, 1986.
- Loth, E., Steele, A., Ichter, B., Selig, M., and Moriarty, P.: Segmented ultralight pre-aligned rotor for extreme-scale wind turbines, in: 50th AIAA Aerospace Sciences Meeting including the New Horizons Forum and Aerospace Exposition, p. 1290, 2012.
- 1360 Lønbæk, K., Bak, C., Madsen, J. I., and McWilliam, M.: A method for preliminary rotor design – Part 1: Radially Independent Actuator Disc model, *Wind Energy Science*, 6, 903–915, <https://doi.org/10.5194/wes-6-903-2021>, 2021.
- Madsen, H. A., Larsen, T. J., Pirrung, G. R., Li, A., and Zahle, F.: Implementation of the blade element momentum model on a polar grid and its aeroelastic load impact, *Wind Energy Science*, 5, 1–27, <https://doi.org/10.5194/wes-5-1-2020>, 2020a.
- Madsen, H. A., Zahle, F., Meng, F., Barlas, T., Rasmussen, F., and Rudolf, R. T.: Initial performance and load analysis of the LowWind turbine in comparison with a conventional turbine, *Journal of Physics: Conference Series*, 1618, 032 011, <https://doi.org/10.1088/1742-6596/1618/3/032011>, 2020b.

- Madsen, M. H. A., Zahle, F., Horcas, S. G., Barlas, T. K., and Sørensen, N. N.: CFD-based curved tip shape design for wind turbine blades, *Wind Energy Science*, 7, 1471–1501, <https://doi.org/10.5194/wes-7-1471-2022>, 2022.
- Manolas, D. I., Serafeim, G. P., Chaviaropoulos, P. K., Riziotis, V. A., and Voutsinas, S. G.: Assessment of load reduction capabilities using passive and active control methods on a 10MW-scale wind turbine, *Journal of Physics: Conference Series*, 1037, 032 042, <https://doi.org/10.1088/1742-6596/1037/3/032042>, 2018.
- Martínez-Tossas, L. A. and Meneveau, C.: Filtered lifting line theory and application to the actuator line model, *Journal of Fluid Mechanics*, 863, 269–292, 2019.
- Menter, F. R.: Two-equation eddy-viscosity turbulence models for engineering applications, *AIAA Journal*, 32, 1598–1605, 1994.
- Meyer Forsting, A. R., Pirrung, G. R., and Ramos-García, N.: A vortex-based tip/smearing correction for the actuator line, *Wind Energy Science*, 4, 369–383, <https://doi.org/10.5194/wes-4-369-2019>, 2019.
- Michelsen, J. A.: Basis3D - a Platform for Development of Multiblock PDE Solvers, Tech. Rep. AFM 92-05, Technical University of Denmark, 1992.
- Michelsen, J. A.: Block structured Multigrid solution of 2D and 3D elliptic PDE's, Tech. Rep. AFM 94-06, Technical University of Denmark, 1994.
- Phillips, W. F. and Snyder, D. O.: Modern adaptation of Prandtl's classic lifting-line theory, *Journal of Aircraft*, 37, 662–670, 2000.
- Pirrung, G. R. and Gaunaa, M.: Dynamic stall model modifications to improve the modeling of vertical axis wind turbines, DTU Wind Energy E-0171, Roskilde, Denmark, 2018.
- Ramos-García, N., Sørensen, J., and Shen, W.: Three-dimensional viscous-inviscid coupling method for wind turbine computations, *Wind Energy*, 19, 67–93, 2016.
- Sørensen, J. N.: *General Momentum Theory for Horizontal Axis Wind Turbines*, vol. 4, Springer, 2015.
- Sørensen, J. N. and Shen, W. Z.: Numerical Modeling of Wind Turbine Wakes, *Journal of Fluids Engineering*, 124, 393–399, <https://doi.org/10.1115/1.1471361>, 2002.
- Sørensen, N. N.: *General Purpose Flow Solver Applied to Flow over Hills*, Risø-R- 827-(EN), Risø National Laboratory, Roskilde, Denmark, 1995.
- Sørensen, N. N.: *HypGrid2D a 2-D Mesh Generator*, Risø-R- 1035-(EN), Risø National Laboratory, Roskilde, Denmark, 1998.
- Sun, Z., Zhu, W. J., Shen, W. Z., Zhong, W., Cao, J., and Tao, Q.: Aerodynamic Analysis of Coning Effects on the DTU 10 MW Wind Turbine Rotor, *Energies*, 13, 5753, <https://doi.org/10.3390/en13215753>, 2020.
- Sun, Z., Zhu, W., Shen, W., Tao, Q., Cao, J., and Li, X.: Numerical simulations of novel conning designs for future super-large wind turbines, *Applied Sciences*, 11, 1–17, <https://doi.org/10.3390/app11010147>, 2021.
- Theodorsen, T.: *General theory of aerodynamic instability and the mechanism of flutter*, Tech. Rep. NACA No. 496, National Advisory Committee for Aeronautics, (last access: 23 November 2021), 1935.
- Wilson, R. E. and Lissaman, P. B.: *Applied aerodynamics of wind power machines*, Tech. rep., Oregon State Univ., Corvallis (USA), <https://www.osti.gov/biblio/7359096>, 1974.
- Zahle, F.: *Parametric Geometry Library (PGL)*, Tech. rep., DTU Wind Energy, <https://gitlab.windenergy.dtu.dk/frza/PGL> (last access: 14 February 2025), 2019.
- Zahle, F., Li, A., Lønbæk, K., Sørensen, N. N., and Riva, R.: Multi-fidelity, steady-state aeroelastic modelling of a 22-megawatt wind turbine, *Journal of Physics: Conference Series*, 2767, 022 065, <https://doi.org/10.1088/1742-6596/2767/2/022065>, 2024.

- 1405 Zuteck, M.: Adaptive blade concept assessment: curved platform induced twist investigation, Tech. rep., Sandia National Labs., Albuquerque, NM (US); Sandia National Labs, 2002.
- Øye, S.: Instationære, Aerodynamiske Kræfter på Todimensionalt Vingeprofil, Tech. Rep. AFM 81-05 Notat VK-58-800122, Afdelingen for Fluid Mekanik, Den Polytekniske Lærestalt, in Danish, 1981.
- Øye, S.: A simple vortex model, in: Proceedings of the Third IEA Symposium on the Aerodynamics of Wind Turbines, pp. 4.1–4.15, ETSU, 16–17 November 1989, Harwell, UK, NTIS Issue number 199106, 1990.